8-26-2022

ADVANCED LITHIUM METAL BATTERIES: FUNCTIONAL ELECTROLYTE ADDITIVE AND LITHIUM METAL/SOLID-STATE ELECTROLYTE INTERFACE ENGINEERING

Abiral Baniya
Syracuse University, abaniya@syr.edu

Follow this and additional works at: https://surface.syr.edu/etd

Part of the Materials Science and Engineering Commons

Abstract

Majority of the energy in current world is produced and consumed by burning non-renewable

fossil fuel sources such as coal, oil, and natural gas, etc. It is taking a toll on our planet earth due

to high rates of carbon and greenhouse emissions. This calls for an urgent need of energy

transition from conventional fossil fuel to renewable and sustainable energy sources such as

solar, wind, geothermal, etc. However, harnessing energy from such renewables are constrained

by their intermittency and non-dispatchability, requiring some sort of efficient energy storage

systems that can provide continuous energy supply. Batteries in general are considered as a

reliable and conventional means of energy storage as they are used in all forms of portable

devices and smart electronics. However, batteries with higher energy densities that can safely

store energy for long duration and provide uninterrupted energy supply enabling high penetration

of renewables in energy usage are still being pursued. Currently commercialized lithium-ion

batteries (LIBs) which uses graphite anode intercalation chemistry with energy density of 220

Wh kg^{-1} are approaching their ceiling of energy density defined as 300 Wh kg^{-1}. So, it is

imperative to develop new battery chemistries that can provide even higher energy and power

densities to fulfill the ever-increasing energy demand. Lithium metal anodes (LMAs) shows

ultrahigh specific capacity of 3,860 mAh g^{-1}, low redox potential (-3.040 V v/s standard

hydrogen electrode) and are considered an ideal replacement to conventional graphitic anode for

realizing batteries with energy density ~500 Wh kg^{-1} and more. However, the violently reactive

nature of lithium (Li) which incurs severe side reactions when they are used as LMAs results in

electrolyte decomposition forming thick insulating solid electrolyte interphase (SEI) layer, and

growth of fibrous dendritic structure on its surface. Use of electrolyte additives is one of the

effective strategies to form *in-situ* protective SEI layer that can stabilize LMA against severe side

reaction and suppress dendrite growth on its surface. In our work, we reported that at very low concentration optimal amount (3 mM) of novel electrolyte additive, gadolinium nitrate $(Gd(NO_3)_3)$ in LiTFSI- $LiNO_3$ ether solvent based electrolyte promotes plating/stripping of Li in nodular morphology, significantly suppressing dendritic and dead Li growth and enhancing cycle life, and stability of Li metal batteries. The as formed SEI layer composed with additive compounds ensures fast Li ion diffusion and suppression of Li dendrite growth by tuning the SEI composition and facilitating plating/stripping of Li in nodular morphology. Similarly, Solid-state lithium batteries are another battery technology which are generally considered as the next-generation technology benefitting from inherent nonflammable solid electrolytes that promotes safe harnessing of high-capacity Li metal. Among various solid electrolyte ionic conductors, cubic garnet-type $Li_7La_3Zr_2O_{12}$ (LLZO) ceramics hold superiority due to their high room temperature ionic conductivity (10^{-3} to 10^{-4} S cm^{-1}) and good chemical stability against Li metal. However, commercialization of garnet electrolyte based solid-state batteries has been constrained by poor Li wetting behavior of the garnet surface resulting in interfacial mismatch, uneven current distribution, and high interfacial impedance. In our next work, we demonstrate a facile and effective process to significantly reduce the interfacial impedance by modifying the surface of Al-LLZO garnet-type solid electrolyte with a thin layer of silicon nitride (Si_3N_4). This interfacial layer provides an intimate chemical and physical contact with Li metal as it shows lithiophilic property and forms an intermediate Li metal alloy at the interface. The interface modified Li/garnet cells exhibited low overpotential and long-term stable plating/stripping cycles at room temperature compared to bare garnet. Thus, this dissertation work provides a significant advancement toward additive and surface engineering techniques for enhancing the overall performance of two different state of the art Li metal battery systems.

ADVANCED LITHIUM METAL BATTERIES: FUNCTIONAL ELECTROLYTE ADDITIVE

AND LITHIUM METAL/SOLID-STATE ELECTROLYTE INTERFACE ENGINEERING

by

Abiral Baniya

B.E., Kathmandu Engineering College, 2014

M.S., South Dakota State University, 2018

Dissertation

Submitted in partial fulfillment of the requirements for the degree of

Doctor of Philosophy in Mechanical & Aerospace Engineering

Syracuse University

August 2022

Ali Ali El-Magrous, and all others who have helped me generously throughout my Ph.D. journey. I am blessed to have earned the friendship of some wonderful people while living at Brookings, SD and Syracuse, NY. The summer football group, thank you for the time we spend together competing as a team, it strengthened the sense of team spirit and good sportsmanship in me. All the families and friends I met in Brookings and Syracuse will always be in my best memories, they made me feel at home although I was miles away.

Finally, my sincere gratitude to all my family members, who all are my support system, inspiring me to be the best version of me everyday. Similarly, there is no measure of blessings, unconditional love and support that I am continuously bestowed upon by my parents Mr. Mukunda Raj Baniya and Mrs. Rajkumari Chhetry. This would not have been near possible without their valuable life lessons and consistent advice. They are the one who make me believe in myself, giving me strength to chase my dreams.

-   *Abiral Baniya*

Table of Contents

Abbreviations

LIB   Lithium-ion batteries

Li   Lithium

LE   Liquid electrolyte

LMA   Lithium metal anode

SEI   Solid electrolyte interphase

LMB   Lithium metal battery

SSE   Solid-state electrolyte

CVD   Chemical vapor deposition

CuCF   Copper-clad carbon foam

ASEI   Artificial SEI

ALD   Atomic layer deposition

$Gd(NO_3)_3$ Gadolinium nitrate

SSB   Solid-state batteries

LISICON   Lithium superionic conductor

NASICON   Sodium superionic conductor

LGPS   Lithium germanium phosphorus sulfide

LiPON   Lithium phosphorus oxynitride

LATP	Lithium aluminum titanium phosphate
LLZO	$Li_7La_3Zr_2O_{12}$
MLD	Molecular layer deposition
LALZWO	$Li_{5.9}Al_{0.2}La_3Zr_{1.75}W_{0.25}O_{12}$
PECVD	Plasma enhanced chemical vapor deposition
LPCVD	Low pressure chemical vapor deposition
Ebeam	Electron beam
ALD	Atomic layer deposition
Al-LLZO	$Li_{6.25}Al_{0.25}La_3Zr_2O_{12}$
Si_3N_4	Silicon nitride
XRD	X-ray diffraction
XPS	X-ray photoelectron spectroscopy
AFM	Atomic force microscopy
SEM	Scanning electron microscopy
FESEM	Field emission SEM
EDS	Energy dispersive spectroscopy
EIS	Electrochemical impedance spectroscopy
LSV	Linear sweep voltammetry

CV   Cyclic voltammetry

BMS   Battery management system

$LiPF_6$ Lithium hexafluorophosphate

EC   Ethylene carbonate

DEC   Diethyl carbonate

EMF   Electromotive force

DOD   Depth of discharge

SOC   State of charge

SOH   State of health

CE   Coulombic efficiency

PC   Propylene carbonate

RT   Room temperature

R_{ct} Charge transfer resistance

TEM   Transmission electron microscopy

ECM   Equivalent circuit model

LCO   Lithium cobalt oxide

LFP   Lithium iron phosphate

NMC   Lithium nickel manganese cobalt oxide

List of Figures

List of Tables

Chapter 1: Introduction

1.1 Background

Energy is not only the backbone in developing various infrastructures but is also vital for carrying out daily life activities such as sustenance, transportation, production, and overall societal upbringing. In current global scenario majority of energy is produced and consumed by burning non-renewable energy sources such as coal, oil, and natural gas etc. The exploitation of these fossil fuels continues to account for the largest share of energy production and consumption in the world, by which we are endangering our planet due to carbon and greenhouse gas emissions [1]. The high emission rate of these greenhouse gases by burning fossil fuel is raising the earth's temperature, triggering the catastrophes such as climate change and natural disasters. Earth's temperature has risen by 0.14 °C per decade since 1880, and 2021 was the sixth-warmest year on record based on National Oceanic and Atmospheric Administration (NOAA) data [2]. As suggested by the International Energy Agency (IEA), the production of CO_2 majorly from transportation and power generation sectors needs to be reduced by 21% and 42%, respectively, by 2050 to ensure a possibility of sustainable future [3, 4]. Therefore, there is an urgent need of energy transition from conventional fossil fuel usage dominantly in transportation and power generation sectors to renewable and sustainable energy sources such as solar, wind, geothermal, etc. Figure 1.1 (a) shows the annual share of energy sources used for fuel production and consumption according to 2021 data from IEA [5]. Similarly, Figure 1.1 (b) shows the history and projection of global primary energy consumption by energy sources from 2010 to 2050, data from Environmental Impact Assessment (EIA), 2021 [6].
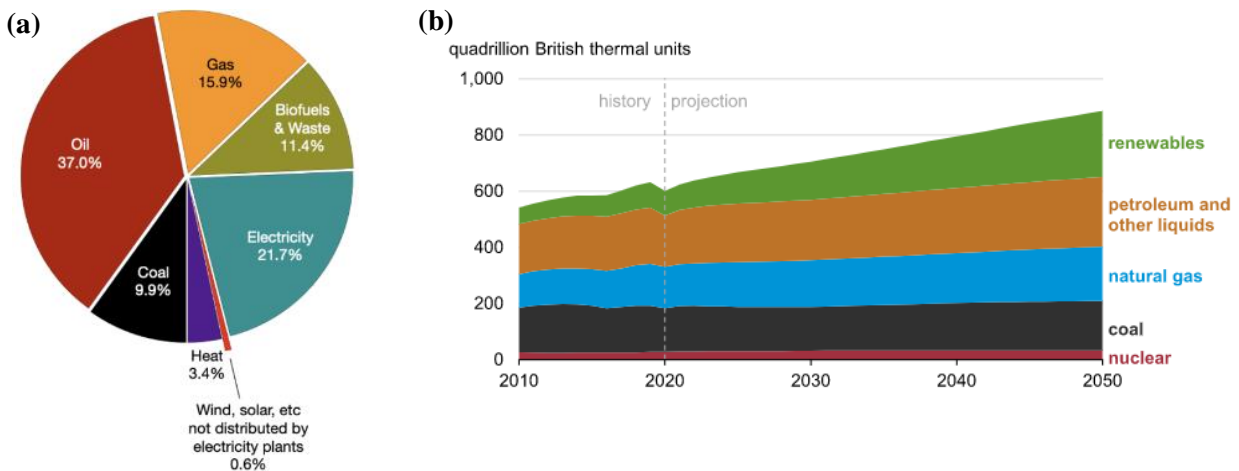
Figure 1. 1 (a) World final energy by annual share of fuel, Data: IEA (2021) [5] and (b) Global primary energy consumption by energy source (2010-2050), Data: EIA (2021) [6].

However, harnessing energy from the renewables such as solar and wind are constrained by their intermittency and non-dispatchability, requiring some sort of energy storage system to address this issue. Batteries in general have been a reliable and conventional means of energy storage from portable devices to smart electronics. Further, higher energy density batteries that can store energy for long duration are considered as solutions for issues associated with high penetration of renewables into the electric grid system [7]. The requirement of efficient energy storage systems is not only limited to electric grids. There is a continuous market demand of electric energy storage system in the fields of transportation (e.g. electric vehicles), residential buildings for power-backup, intrinsically integrated systems (e.g. solar charging batteries [8]), etc. Therefore, to efficiently store the intermittent renewables and to effectively power the next generation electric systems, the development of energy storge systems such as batteries with high energy density and long cycle life is of the essence [9-14]. Among numerous energy storage systems, lithium-ion batteries (LIBs) hold the potential to fulfill the energy demands for each of

the abovementioned applications due to their high specific energy density and high volumetric energy density providing lighter weight and smaller size, respectively.

1.2 Lithium-ion batteries and beyond

Conventional rechargeable type such as lead-acid, nickel-cadmium, and nickel-metal hydride battery systems were the first type of rechargeable battery systems that were very popular during 1980's. They were mainly used in starting automotive engines, small scale power storage systems, and grid-scale power systems [15]. However, the specific energy and energy density of these type of batteries were very less, about 35-40 Wh kg^{-1} and 80-90 Wh L^{-1}, respectively [16]. As the advancement in technologies picked up its pace the consumer market demand for rechargeable and portable electronics such as minicomputers and cameras went over the roof. These batteries were not capable to satiate the energy requirement, so there was a need of major technological breakthrough for alternative energy storage system with higher density, smaller size, and less weight. The first major breakthrough in battery science came from Whittingham et al. at Exxon Corporation, USA in 1979, in the form of rechargeable LIB which had lithium (Li) metal as anode and titanium disulfide (TiS_2) as cathode [17]. Although, the battery was functional, the voltage output from it was only 2 V. Then, in 1979 Goodenough et al. introduced the use of lithium cobalt oxide ($LiCoO_2$) as cathode material, with similar intercalation structure as TiS_2 (Figure 1.2) which increased the voltage output of LIBs to 4 V [18]. In both of the battery systems Li metal was introduced as potential anode, however, the violent reaction and unstable nature of Li toward organic liquid electrolytes (LEs) led to safety hazards. So, eventually LIBs with carbonaceous anode (e.g. graphitic anode) was designed by Yoshino et al. from Japan in 1986 [19]. This led to commercialization of rechargeable and safe LIBs by SONY in 1991 [20]. Recognizing the tireless efforts for research and development of LIBs and their

3

contribution to science, chemists Whittingham, Goodenough, and Yoshino were awarded the
Nobel Prize in Chemistry-2019 [21].
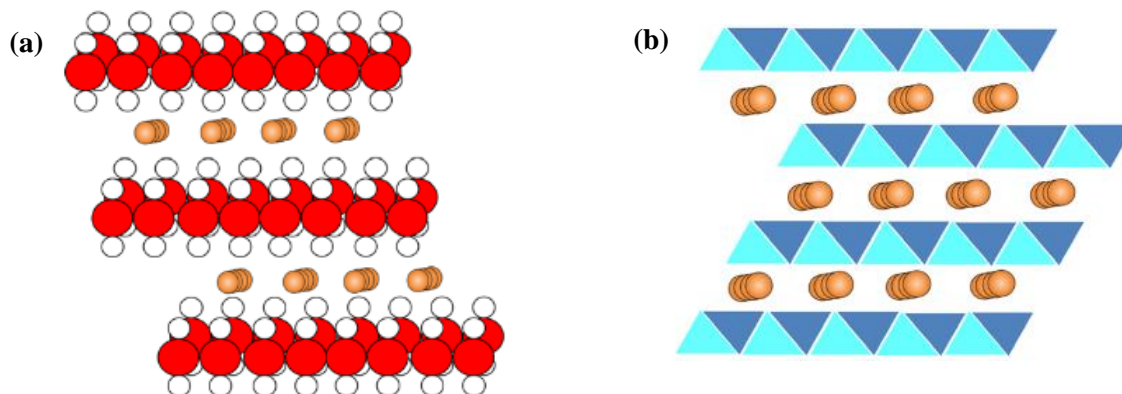
Figure 1.2 (a) Layered structure of TiS_2 with intercalated Li ions by Whittingham and (b)
Similar layered structure of CoO_2 with intercalated Li ions by Goodenough [22].

Current commercial LIB's which are extensively used worldwide for powering applications are
approaching the ceiling of energy density, 300 Wh kg^{-1} that is allowed by intercalation
chemistries of graphite anode. Thus, the major limiting factor for lower energy density of state-
of-the-art Li ion chemistry is the lower specific capacity of graphite anode which has a
theoretical specific capacity of 372 mAh g^{-1}. To overcome this limitation the studies on
investigating higher capacity anode materials are important. As graphite provides lithiation based
on intercalation mechanisms accommodating one Li ion per six carbon atoms, this has motivated
the studies of anode materials that exhibit alloy-based lithiation [23-25]. One of such promising
anode material is silicon with theoretical specific capacity of 4200 mAh g^{-1} [26]. However, the
main drawback of silicon based anodes is that it undergoes a drastic volume change
approximately 400 % during lithiation/delithiation cycles causing huge capacity fade and

mechanical breakage of silicon particles. Although various strategies such as use of silicon host nanostructures, protective layer coating, hollow cellular host, and porous silicon materials have been employed, it still faces limitation on scaling up to cost effective production volume [23, 27-31].

As it is imperative to develop novel battery chemistries that can ascertain high energy and power density to fulfill ever-growing energy demand, lithium metal anode (LMA) are considered a promising replacement to conventional graphitic anode to realize energy density ~500 Wh kg^{-1} and more [32]. Li metal as anode is an ideal candidate for replacing graphite, as it possess high specific capacity (3860 mAh g^{-1}), lowest reduction potential (-3.04 V vs standard hydrogen electrode (SHE)), and low gravimetric density (0.534 g cm^{-3}) among all elements in the Periodic Table [33]. Figure 1.3 (a) shows the Li ion battery research landscape and direction being taken by researchers, considering advancement in nanotechnology and innovations based on safe application for reviving LMA [34].

Further, the specific capacity of LIBs are not only constrained by anode but also by cathode that is paired with it. So, other major drawback associated with commercialized LIBs is coupling of their anode with low capacity cathodes. The existing lithium metal oxides based cathodes can offer specific capacities of only about 160 to 200 mAh g^{-1}. Thus, even if they are paired with high capacity LMA, the deliverable capacity from full cell (combination of cathode and anode) will always be low. So, much thought has also gone into developing high capacity cathodes e.g., sulfur and oxygen based, that can be paired with Li metal to formulate battery chemistries like Li-S and Li-O$_2$, respectively [35]. Figure 1.3 (b) shows the theoretical gravimetric energy densities at materials level for combinations of different anode and cathode and at different mass loadings of cathode active material. Similarly, the green band shows the target energy densities

(a)

Intercalation Graphite anode	Alloy anode	Lithium metal anode	Lithium metal anode
Separator	Separator	Separator	Solid separator
Cathode LCO, NMC, LFP	Cathode LCO, NMC, LFP	Cathode LCO, NMC, LFP	Cathode LCO, NMC, LFP
Li-ion Liquid electrolyte 200-250 Wh kg^{-1}	Li-ion Liquid electrolyte 250-300 Wh kg^{-1}	Li-metal Liquid electrolyte >400 Wh kg^{-1}	Li-metal Solid-state electrolyte >400 Wh kg^{-1}

(b)

Figure 1. 3 (a) Lithium battery research landscape, from intercalation and alloy anodes to high energy density LMA and (b) Theoretical gravimetric energy density for different anode/cathode combinations at different cathode mass loadings represented by different color and curves, respectively [36].

6

at cell level which at present context have risen to 500 Wh kg^{-1} [37]. Therefore, to envision a high energy density battery, along with the use of LMA the application of lean electrolyte, high mass loading and high capacity cathodes should also be equally considered.

Even though, LMA is considered as an ideal anode material for high energy density next-generation LIBs, there are many hurdles which limits its practical applications. As shown in Figure 1.4 (a), due to high reactivity of LMA, it reacts with electrolyte to form a solid electrolyte interphase (SEI) layer on top of Li metal. During further cycling operations severe side reactions can occur resulting in formation of thick accumulated insulating SEI which blocks the Li ion transport, resulting in severe capacity fade.

Along with highly reactive nature of Li metal another major issue associated with LMA is its infinite volume change during Li metal plating and dendritic growth during consecutive deposition [34]. Due to large variation in volume during cycling, cracks can develop within the SEI layer exposing fresh Li underneath [38]. The exposed layer of fresh Li will have low Li nucleation energy barrier for Li ion plating compared to layers covered with SEI, this results in non-uniform and preferential morphology of Li deposition which transforms into dendritic Li that shoots out through the cracks in further cycling. The dendrites with whiskers like morphology can penetrate through the separator and cause internal short circuit, thermal runaway and even cell explosion [39]. Further, these dendrites can break during stripping cycle which will produce isolated or dead Li on the surface of Li electrode. These dead Li are electrochemically inactive, causing inventory and capacity loss in the battery system. Continuous cycling will cause the above phenomena to occur repeatedly, which will eventually result in formation of accumulated dead Li, thick insulating SEI layer, porous and pulverized Li electrode.

7
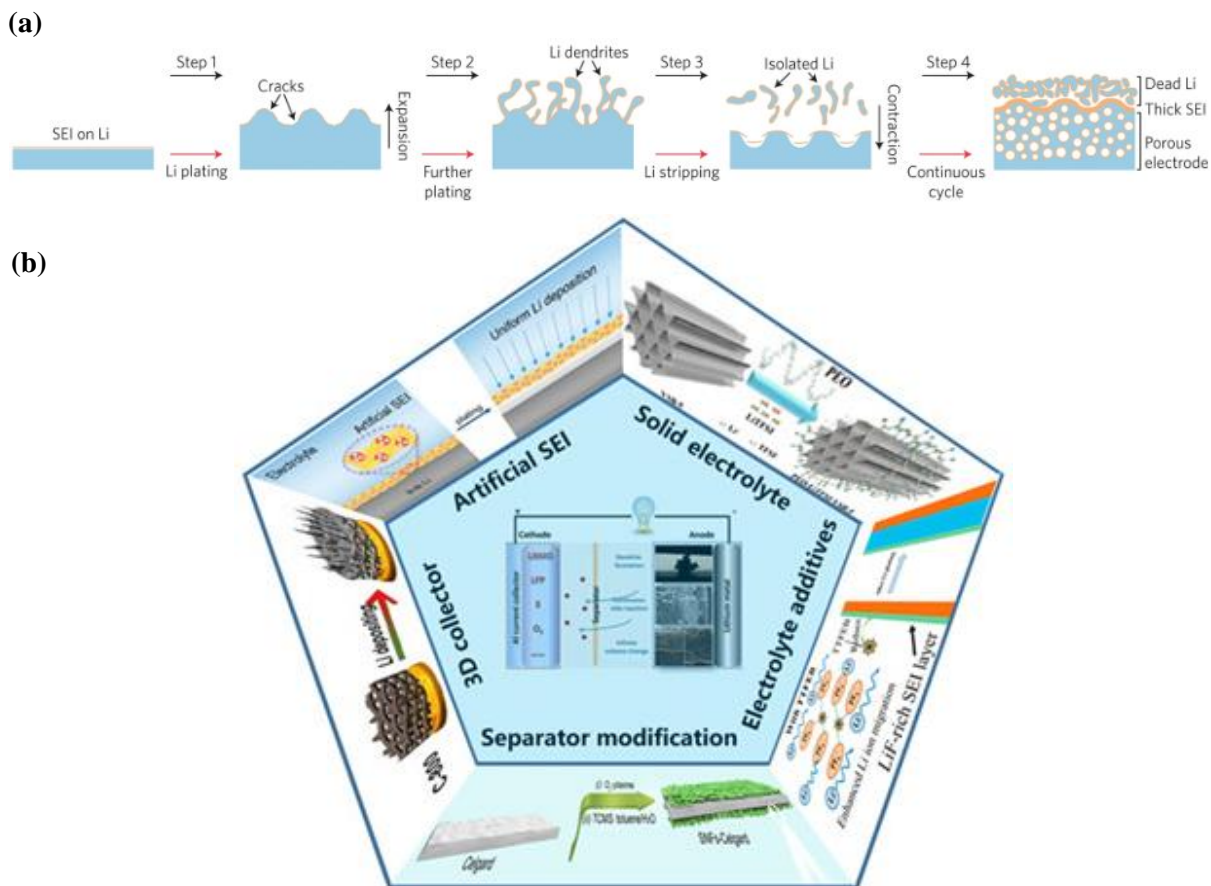
Figure 1. 4 (a) Schematic diagram showing the process of Li dendrite growth during Li plating/stripping process [34] and (b) Chart showing different strategies to protect LMA in lithium metal batteries [40].

Several diversified strategies have been introduced by number of researchers to restrain side reactions, suppress dendrite growth, and stabilize SEI layer related to LMA. As shown in Figure 1.4 (b), different approaches have been used, such as artificial protective SEI on top of Li metal, use of additives in electrolyte, 3D porous current collector, separator modifications, and use of solid state electrolyte [40-47]. Therefore, in order to address major issues associated with LMA and to achieve its effective application in lithium metal battery (LMB), the common strategies are: (1) designing lithiophilic, microporous, and stable 3D framework to homogenize the Li ion flux and minimize the volume change during plating/stripping cycles; (2) stabilizing Li anode by

engineering artificial *ex-situ/in-situ* protective SEI layer at the interface; (3) designing solid-state electrolyte (SSE) and its interface with Li metal for preventing dendrite propagation; and (4) modifying separator films to enhance the interfacial interactions with Li electrode.

1.3 Literature review

1.3.1 Advances in Li metal protection

As discussed in previous sections, the coupling of LMA with high capacity cathodes is essential to realize high energy density LMBs. However, using Li metal as anode is besieged with multiple interrelated challenges such as safety hazards, rapid capacity fade, violent chemical reactivity, infinite volume change, unstable SEI formation, and dendritic growth. Therefore, to circumvent these issues various strategies have been investigated by the researchers such as minimizing volume change by using stable 3D Li host, developing varieties of artificial SEI layer, and designing interface stable SSE for Li dendrite suppression.

1.3.1.1 3D nano/microstructured current collectors

The morphologies of electroplated Li metal largely depends on the mass transfer kinetics of its cations in a electrolyte solution [48]. The major types of mass transfer affects experienced by Li cations in an electrolyte solution are: (1) diffusion, (2) convection, and (3) migration. As shown in Figure 1.5 (a) due to natural convection some cations will move faster and other will move slower. This discrepancy will create varied concentration gradient at the electrode interface. Slow movement of Li metal cations towards the electrode surface will create even steeper concentration gradient. As the concentration gradient increases, the cations are not completely plated swiftly, this will cause the metal dendritic structure to grow and propagate into the liquid bulk electrolyte (Figure 1.5 (b)). These metal protrusions will develop a strong electric field experiencing higher local current densities which will cause the dendrite growth to further

accelerate [49, 50]. This condition exacerbates at higher current densities during which the consumption rate of cations is high in the vicinity of negative electrode. As the diffusion rate of Li ions is slower compared to their consumption, large concentration gradient will be established causing inhomogeneous deposition of metal cations.
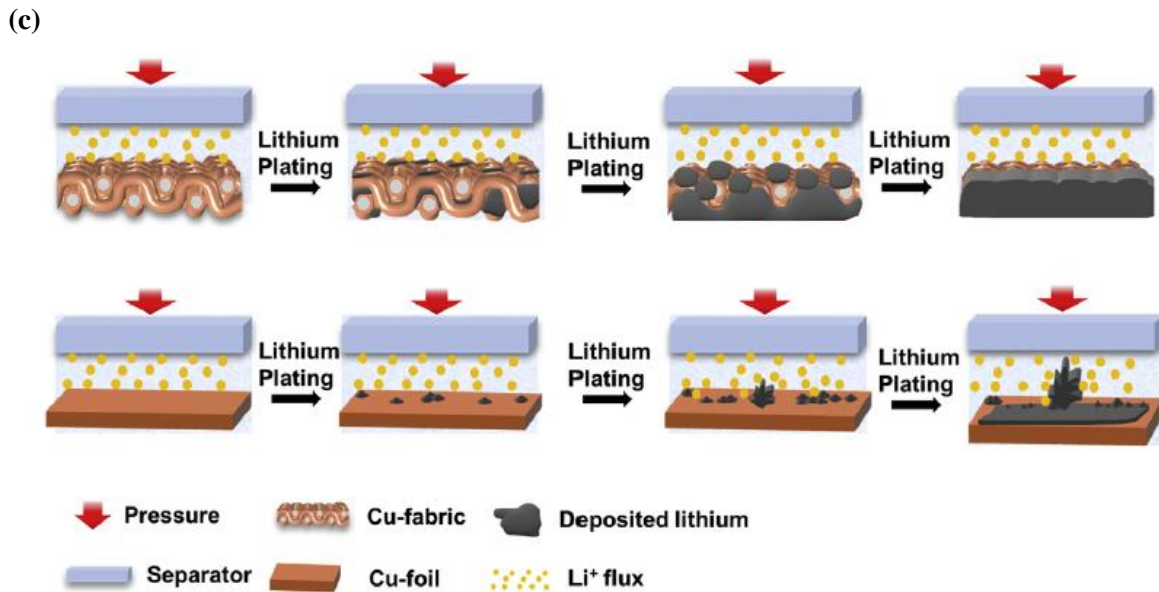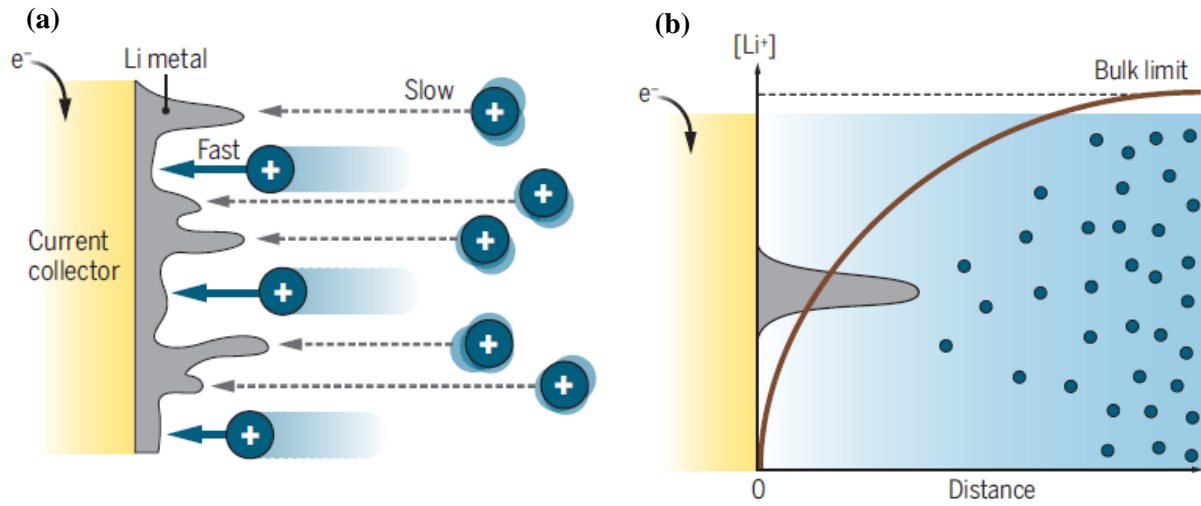
Figure 1. 5 (a) Uneven plating of Li metal ions due to different mass transfer kinetics, (b) large concentration gradient and subsequent protruded morphology of metal cation at the electrode surface [48], and (c) Li ion deposition process in Cu-fabric and Cu-foil [51].

In order to obtain uniform and dendrite free lithium deposition, use of 3D nano/microstructured frameworks as Li hosting anode materials has been a very popular and successful technique [52-54]. The reduction in local current density is achieved when 3D current collector with higher surface area is used instead of planar 2D current collector [55]. This will provide a homogeneous charge distribution within the submicron 3D structure leading to even Li deposition and dendrite suppression. As shown in Figure 1.5 (c), Ye et al. applied copper (Cu) coating into different insulating cloth fabrics to create a 3D soft conductive fabric that provided more uniform lithium deposition and dendritic suppression during the battery cycling. Using this 3D Cu coated soft fabric as anode for LMBs showed prolonged cycling performance for more than 1000 hours compared to using 2D bare Cu [51]. Similarly, along with reduced local current density, the 3D structure used as Li host can compensate the volume change of electrode during cycling [34].

Current collectors play an active role of gripping the electrode materials and providing pathway for electron conduction that cycles through the external circuit. Thus, the major properties in a current collector are they should have high electronic conductivity and electrochemical stability. In addition, a free-standing, mechanically strong and low-cost current collectors are desired for LIBs with superior performance [56]. The main advantages of using 3D current collectors over 2D planar materials (e.g. Al, Cu, and Ni sheets) are that they provide short diffusion length for Li ions, have high electronic conductivity, suppress dendrite growth by facilitating uniform Li deposition, and accommodate volume change during cycling due to large surface area which

further also helps to increase active mass of electrode [57, 58]. The 3D foam type current collectors follow different preparation routes which affects the resulting architecture and performance of thus obtained current collectors. Figure 1.6 shows different methods such as chemical vapor deposition (CVD), pyrolysis, etc. to prepare the 3D foam-type current collectors.
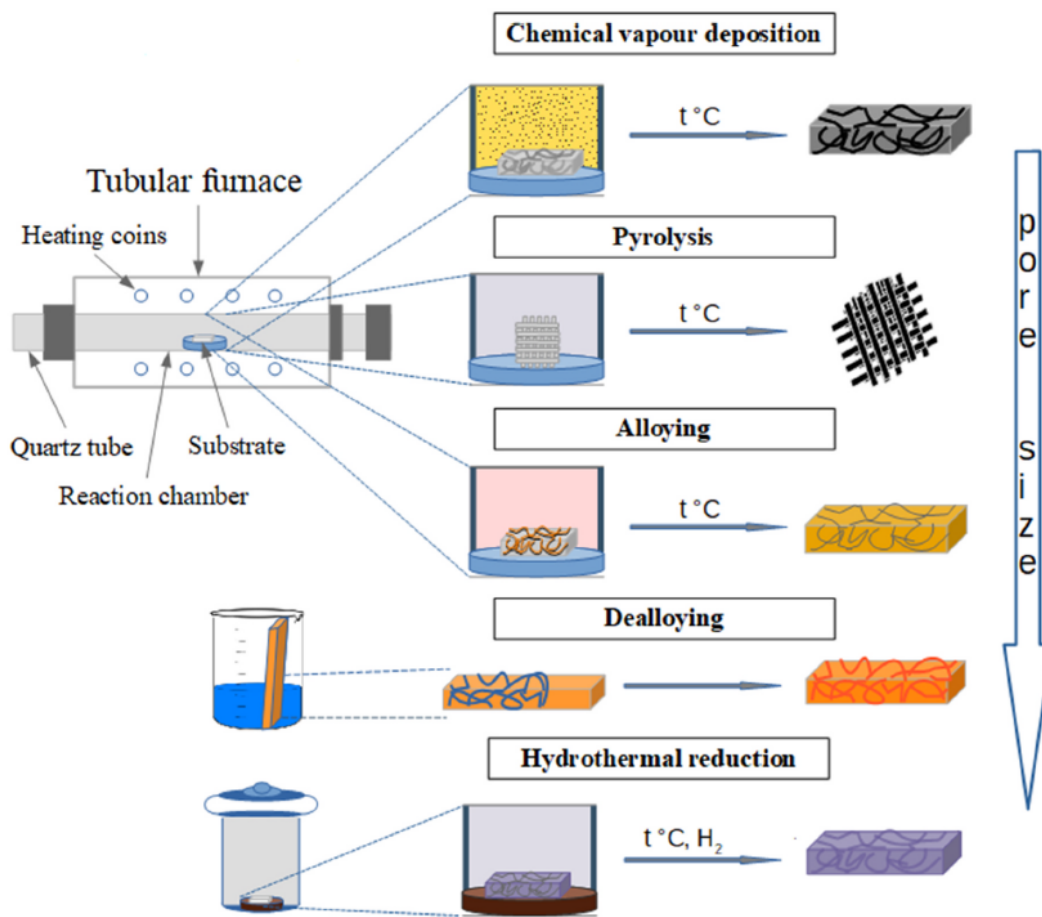
Figure 1. 6 Schematics of different synthesis routes for the preparation of 3D current collectors [54].

The 3D current collector properties such as pore size and conductivity depend on the materials used and synthesis route followed.

After multiple reviews and experiments it was determined that only porous framework with 3D

structure, but poor Li wettability was still unable to uniformly deposit Li and avoid high

nucleation overpotential. Therefore, various approaches have been reported to apply lithiophilic

coatings or decorations on thus prepared porous frameworks. As shown in Figure 1.7 (a), Zhang

et al performed CVD to coat lithiophilic N-doped graphene on the 3D Cu current collector

surface [59]. Figure 1.7 (a) also shows the differences in nature of Li deposition and SEI layer

formation in non-coated and coated 3D Cu framework. Attributed to irregular lithiophobic

surface of non-coated 3D Cu, there was a tendency of non-uniform Li deposition, dendritic

growth and formation of fragile SEI. The deposition of lithiophilic N-doped graphene facilitated

in uniform Li deposition and stable SEI formation.
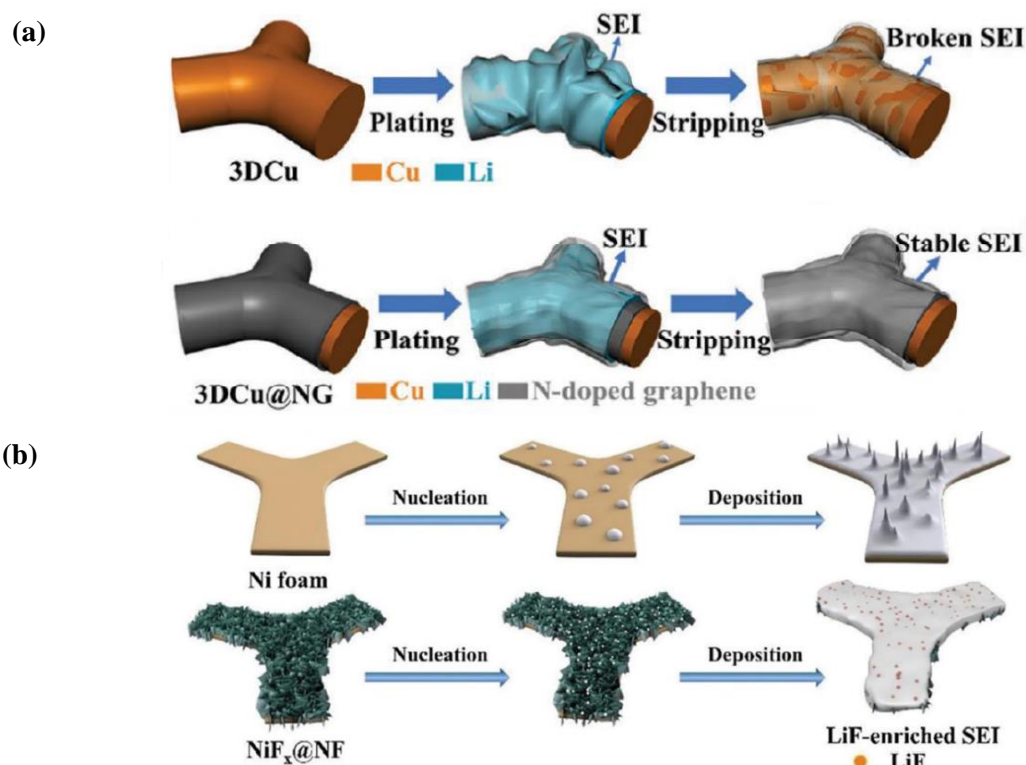
Figure 1. 7 (a) 3D porous Cu framework and effect of N-doped graphene coating on it [59], and (b) Li deposition behavior on bare NF and NiF$_x$ coated NF 3D current collector [60].

Similarly, on other work Huang and team conformed the lithiophilic coating of nickel fluoride (NiF$_x$) nanosheets on nickel foam (NF) reacted with deposited Li to form LiF-rich SEI layer on the top of 3D Ni foam current collector [60]. As shown in Figure 1.7 (b), the formation of this LiF-rich stable SEI layer suppressed dendrite growth and superior lithiophilicity of NiF$_x$ nanosheets decreased the Li nucleation barrier facilitating uniform homogeneous Li deposition. The interconnected 3D morphology of thus obtained current collector effectively reduced the local current density thus avoiding dendrite formation. Some of the other lithiophilic coatings that have been studied in similar way are gold (Au) [61], silver (Ag) [62], antimony (Sb) [63], and zinc oxide (ZnO) [64].

In our previous work, we reported the use of novel 3D light-weight, lithiophilic and flexible copper-clad carbon foam (CuCF) as LMA current collector [46]. This copper coated carbon foam framework was fabricated by pyrolysis of melamine-formaldehyde foam (MF) to obtain carbon foam (CF) followed by electroplating of Cu on thus formed CF to obtain CuCF. The total thickness of Cu deposited on CF was dependent on the applied electrodeposition time. As shown in Table 1.1, the maximum cycling number and coulombic efficiency (CE) of cells with CuCF current collector was optimized varying Cu loading density and effective electrodeposition time.

Table 1. 1 Performance summary of CuCF fabricated at different Cu electrodeposition time [46].

Sample name	Total time (second) *	Effective electrodeposition time (second)	Average weight (mg)	Cu loading density (mg/cm^{-2})	Cycling number at CE > 90%
CF	-	-	0.50	-	123
CuCF-2	200	120	0.92	0.24	161
CuCF-4	400	240	1.47	0.55	174
CuCF-6	600	360	2.10	0.91	>200
CuCF-8	800	480	2.71	1.25	>200

* Pulse current was applied with 15s of electrodeposition and 10s of rest for each cycle.

Similarly, Figure 1.8 (a-c) shows the voltage profile of Li plating on planar Cu, CF and CuCF , respectively at 0.5 mA cm^{-2} with capacity reaching 4 mAh cm^{-2}. It can be observed that the Li nucleation overpotential for plating is least for the CuCF compared to planar copper current collector. This was attributed to improved lithiophilicity, enhanced surface conductivity, high porosity, and numerous nucleation sides on the CuCF surface after Cu electrodeposition [65]. Further, the Li deposition morphology on each of these current collectors were observed by using SEM images as shown in Figure 1.8 (d-f). The CuCF current collector showed smooth coverage and uniform Li deposition in nodular morphology with no dendrite formation whatsoever. However, growth of fibrous and dendritic lithium was observed on surface of planar copper and partial coverage of Li deposition was obtained on CF current collector surface.
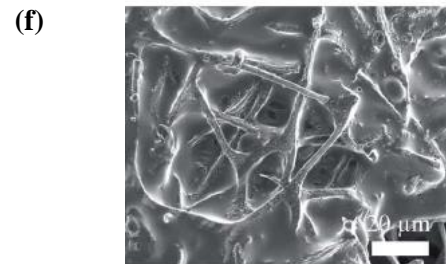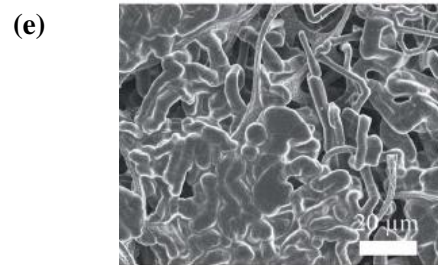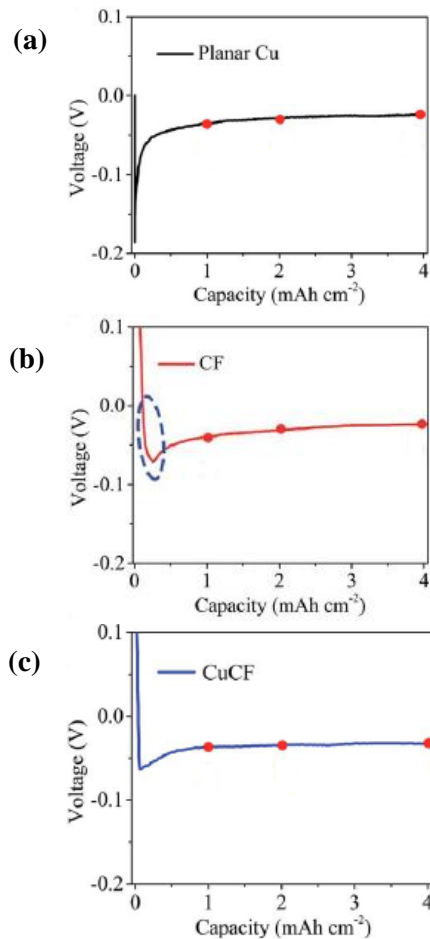
Figure 1. 8 (a-c) Voltage profile for Li plating showing nucleation overpotential for cells cycled at 0.5 mA cm^{-2} with capacity reaching upto 4 mAh cm^{-2} for planar Cu, CF, and CuCF, respectively and (d-f) respective SEM images showing Li deposition morphologies after plating at 4 mAh cm^{-2} capacity [46].

1.3.1.2 *Ex-situ* and *in-situ* artificial SEI design

The SEI layer is one of the critical components of battery research, which forms during initial battery cycling. The pioneering studies on SEI layer were performed by Emanuel Peled [66, 67] and Doron Aurbach [68, 69]. In these studies, they have mentioned that as the electrodes work in conditions extreme to the thermodynamic stability region of electrolyte, any electrolyte can get reduced at the interface and a layer form at the electrode surface. Similarly, as LMAs are highly electronegative, electrolytes used in LMBs get reduced to form a layer on the Li surface [70]. This layer known as SEI is critical to passivate the Li surface, halting the reduction reaction and making it possible to further operate the cell under extreme environment with voltage window reaching above 4 V during cycling. Initial studies of SEI on electrode surfaces was thoroughly performed on carbonaceous anodes [71]. However, compared to Li-ion chemistry LMA incurs more restrictions and requirements on the SEI layer. Some of the properties that should be considered for a superior SEI layer are: (1) high ionic conductivity, (2) good electron-blocking ability, (3) homogenous morphology and composition, (4) good flexibility, and (5) high Young's modulus [33, 38, 72].

As shown in Figure 1.9 (a), the SEI layer is composed of both organic and inorganic phase elements, with organic layer accommodating some part of the electrolyte which enhances the Li ion conduction [73]. The outer layer of SEI are mainly composed of Li alkyl carbonates
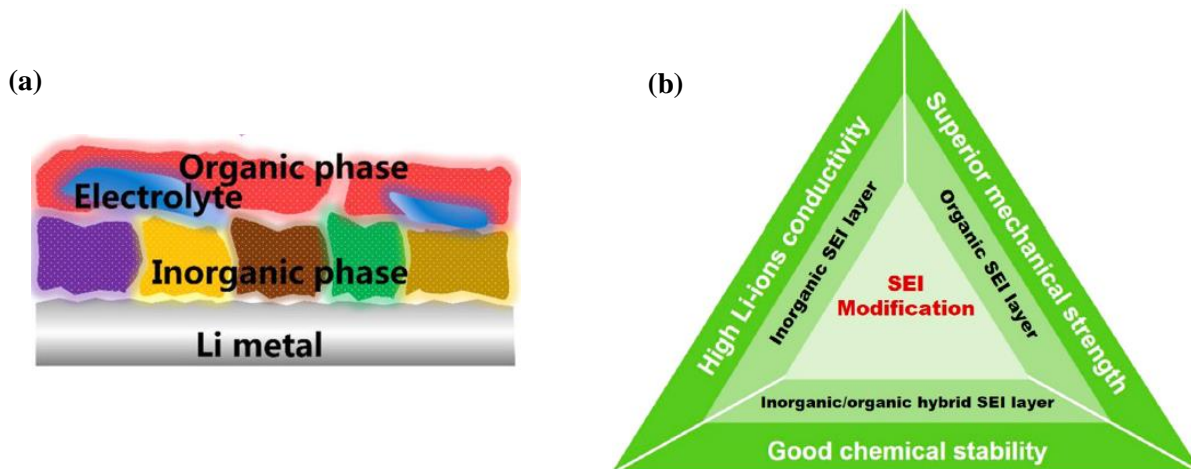
Figure 1. 9 (a) Schematic representation of SEI layer composition at the surface of LMA [73] and (b) Chart showing different SEI modification strategies [74].

(ROCOOLi and ROLi), which further gets converted to Li_2CO_3 when there is trace amount of water present. Similarly, depending upon the Li salts in the electrolyte solvent, components such as Li_2O, Li_2CO_3, and Li halides are mainly found on the inner layer of SEI. However, the naturally occurring SEI are not electrochemically stable, has low Li ion conduction and are mechanically fragile. The fragile SEI film can break during cycling or electrode volume change, exposing fresh electrode surface for reduction and initiating hotspots for dendrite growth. Therefore, the artificial SEI (ASEI) layers are coated or developed on the surface of Li metal electrode that functions as an ideal SEI in the electrochemical system. The main advantage for scientist while developing these ASEI films is that they can tune their chemical composition as desired for e.g., the coating layer can not only be Li ion conductive and chemically stable but also mechanically strong to suppress dendritic growth. These ASEI are generally formed in two ways: (1) *ex-situ* formation where ASEI are coated before battery cycling, and (2) *in-situ*

formation where ASEI are developed during the battery cycling operations. Figure 1.9 (b) shows different strategies employed for modification of SEI layer [74].

The *ex-situ* ASEI layers are coated onto the LMA before battery cycling mainly through physical or chemical deposition routes. The as deposited ASEI layers should conform to have mechanical stability, smooth morphology, passivating the LMA surface and facilitating uniform Li-ion distribution during cycling (Figure 1.10). The fabrication of *ex-situ* ASEI layers are mainly performed using thin-film deposition techniques such as physical vapor deposition (PVD), chemical vapor deposition (CVD), doctor-blading, spin-coating, and drop-casting. The ASEI layers may or may not react with LMA depending upon the nature of deposited material. If the deposited ASEI material does not react with LMA and maintains its pristine form after coating, they are known as physically deposited ASEI layers. Whereas, if the deposited ASEI material undergoes a chemical reaction with LMA and forms a new product with different properties compared to its pristine nature then they are classified as chemically deposited ASEI layers.
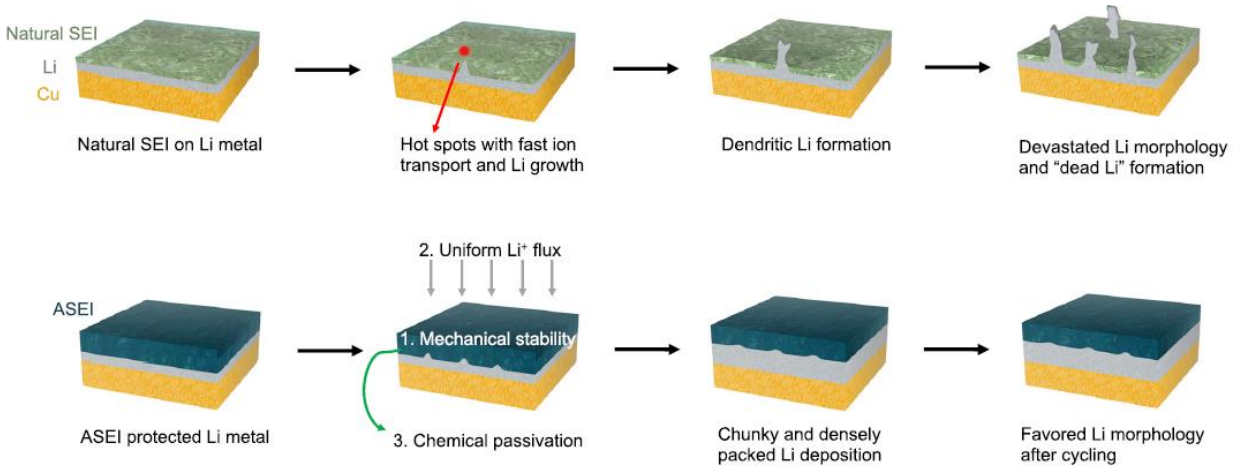
Figure 1. 10 Schematics showing evolution of Li deposition for natural and artificial SEI [75].

Carbon based and polymeric materials are two types of materials that are widely used as coatings for ASEI on LMA. As shown in Figure 1.11 (a), Zhang et al. simply drop casted different concentrations of zinc oxide (ZnO) and carbon nanotubes (CNT) suspensions stirred in 1,3-dioxolane (DOL) solvent onto the Li foil to fabricate ASEI interfacial layer coated LMA [76]. Thus, developed interfacial layer showed lithiophilic-lithiophobic gradient (GZCNT) properties facilitating formation of stable SEI layer and lithium dendrite suppression, respectively (Figure 1.11 (b)). The Li symmetrical cells with GZCNT ASEI were able to be cycled at high current density of 10 mA cm^{-2}, whereas the bare Li and CNT coated Li failed in short period showing high overpotential and unstable plating/stripping.
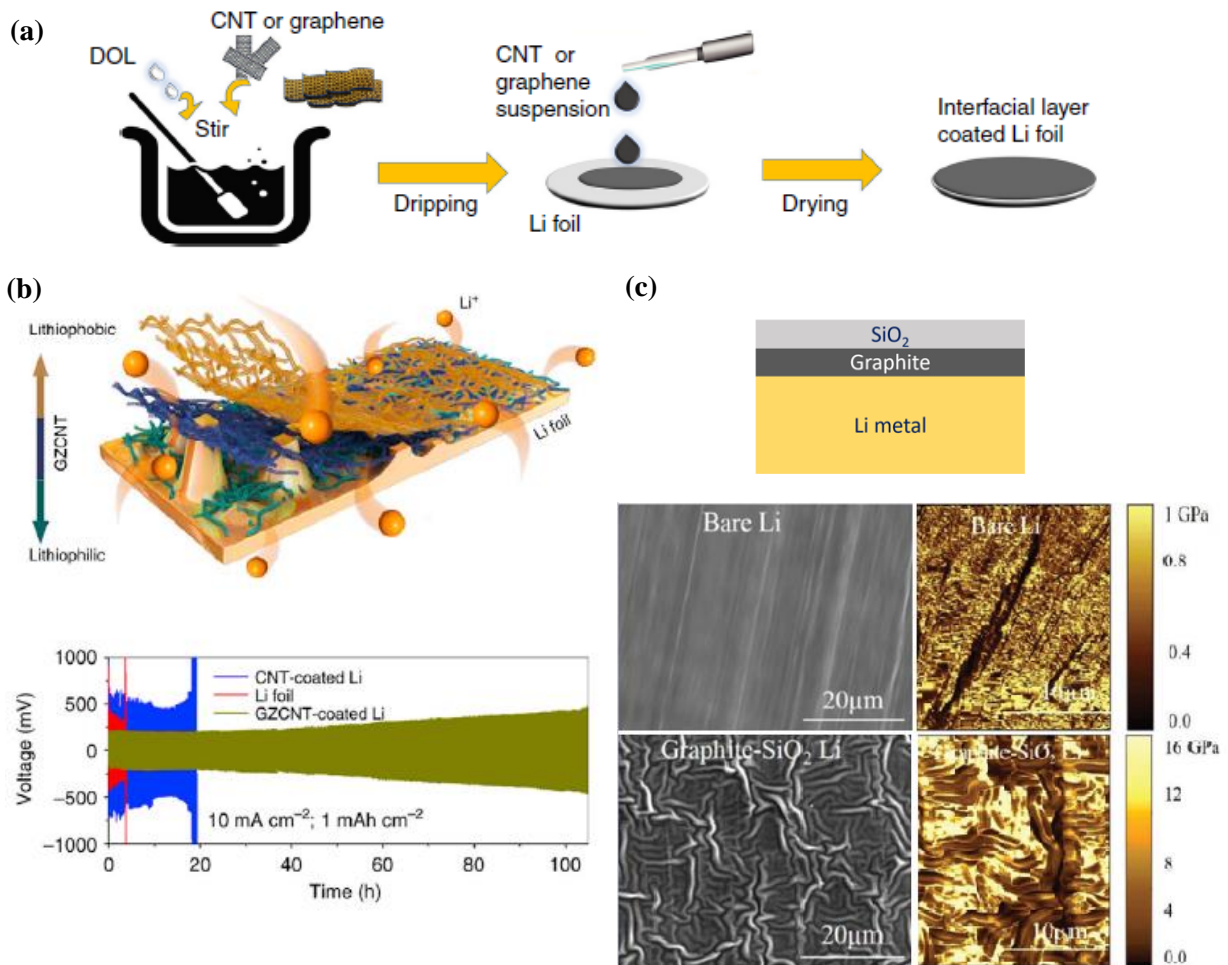
Figure 1. 11 (a) Schematics showing fabrication of ZnO/CNT interfacial layer onto the Li foil. (b) Development of lithiophilic-lithiophobic gradient interfacial layer as ASEI and corresponding Li symmetrical cell cycling [76]. and (c) Sputtered deposited ultrathin graphite/SiO_2 bilayer showing SEM surface morphology and AFM showing Young's modulus values of 1 GPa for bare Li whereas 16 GPa for bilayer deposited Li chips [77].

Similarly, Pathak et al. proposed an ultrathin bilayer of graphite and silicon dioxide (SiO_2) as an ASEI layer, where 20 nm graphite (bottom layer) and 20 nm SiO_2 (top layer) were sputter deposited onto the Li metal chips [77]. In this multifunctional bilayer ASEI design the graphite acted as an electrical bridge between plated Li and Li electrode by providing lower plating impedance and compensating volume expansion during plating/stripping cycles. On the other hand, the SiO_2 layer improved the electron affinity and showed higher Young's modulus to suppress the Li dendrite growth (Figure 1.11 (c)). Further, alumina (Al_2O_3) thin layer was coated onto the Li metal using atomic layer deposition (ALD) [78, 79] and sputtering method [80] which functioned as ASEI layer. In this process, the alumina reacted with Li to form chemically deposited $LiAlO_x$ intermediate ASEI product that enhanced the Li-ion conductivity at the interface and suppressed the dendrite growth due to improved mechanical strength.

Incorporating the fluorination of SEI where lithium fluoride (LiF) acts as a key SEI component has also been widely investigated. It is believed that presence of LiF in SEI improves the cycling performance of LMA as it is an excellent electronic insulator with its wide bandgap preventing the electron tunneling effect [81]. Additionally, LiF possess high ionic conductivity, and low diffusion barrier thus allowing Li ion conduction in parallel manner [82, 83]. Apart from LiF, Li-based alloy phases have also been effectively implemented as interphase component to suppress

20

Li dendrite growth and reduce Li ion diffusion energy. Some of such alloying approaches includes the development of chemically deposited ASEI with formation of Sn-Li, Li_{13}-In_3, Li-Zn, Li_3Bi, Li_3-As, Au-Li, and Si-Li alloy phases [84-87].
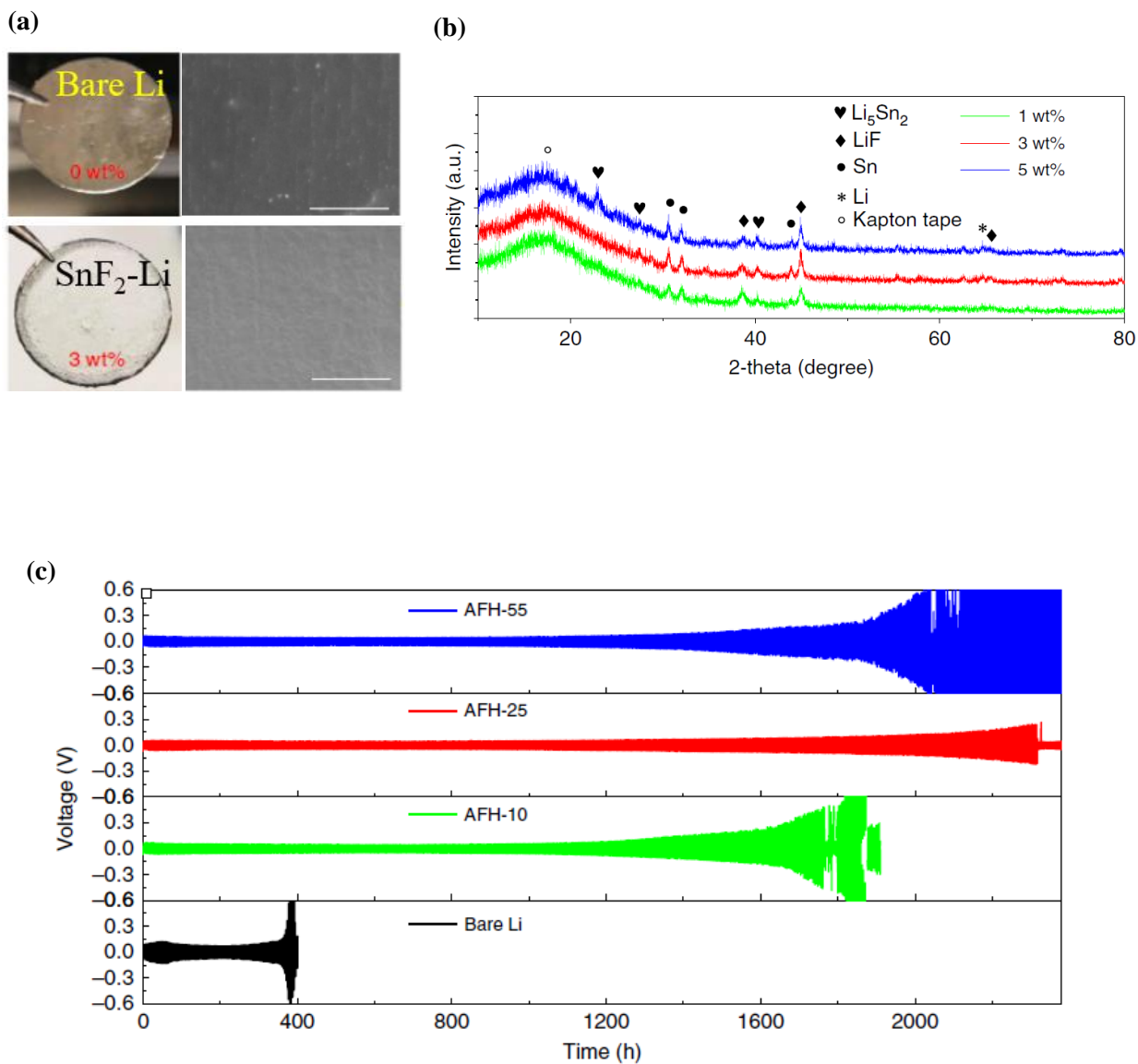
Figure 1. 12 (a) Digital photographs with corresponding SEM images of bare Li and Li treated with SnF_2 solution. The scale bars for SEM are 20 µm, (b) XRD spectrum showing formation of LiF, Sn, and Li-Sn alloy on the surface of Li treated with different weight percentage of

SnF$_2$, and (c) The voltage profile of Li symmetrical cells with bare Li and different thickness

ASEI at current density of 0.5 mA cm^{-2} and capacity of 1 mAh cm^{-2} [88].

In our previous work, we reported a chemically deposited ASEI by pretreating Li anode with Tin

fluoride (SnF$_2$) containing electrolyte (Figure 1.12 (a)) [88]. As the dispersion of SnF$_2$ in LE

mixture was drop casted onto the surface of Li metal, it reacted to form an ASEI layer composed

of LiF, tin (Sn), and Li-Sn alloy (Figure 1.12 (b)). This fluorinated ASEI ensured fast Li ion

diffusion, suppression of Li dendrite growth and stored Li by reversible Li-Sn alloying.

Similarly, superior plating/stripping cycles were achieved for Li symmetrical cells with such

ASEI compared to cells with bare Li (Figure 1.12 (c)).

Polymeric materials are also widely used as ASEI, as these organic materials are elastic in

nature, not only they can provide good contact at the interface and allow dendrite suppression,

but they can also compensate the huge volume change during prolonged cycling [89-91]. Li et al.

used Li polyacrylic acid (LiPAA) to prepare a flexible SEI layer which self-adapted for interface

regulation [92]. Owing to the properties of high binding ability and excellent stability, the

LiPAA polymer based SEI significantly reduced the parasitic reactions and suppressed dendrites

showing stable cycling performance of 700 h for Li symmetrical cells. Similarly, Chen et al.

prepared a 10 nm thick covalent organic framework (COF) films on the Li metal surface which

improved Li ion transfer kinetics [93]. The framework design enabled unique microcellular

structures (Figure (1.13 (a))) which redistributed the Li ion flux leading to uniform

plating/stripping process. Further, the ASEI layer showed high Young's modulus of 6.8 GPa

which was mechanically strong enough to suppress dendrite growth. Thus, the ASEI modified

LMA exhibited stable cycling for 400 h at high current density of 1 mA cm^{-2} (Figure 1.13 (b))).
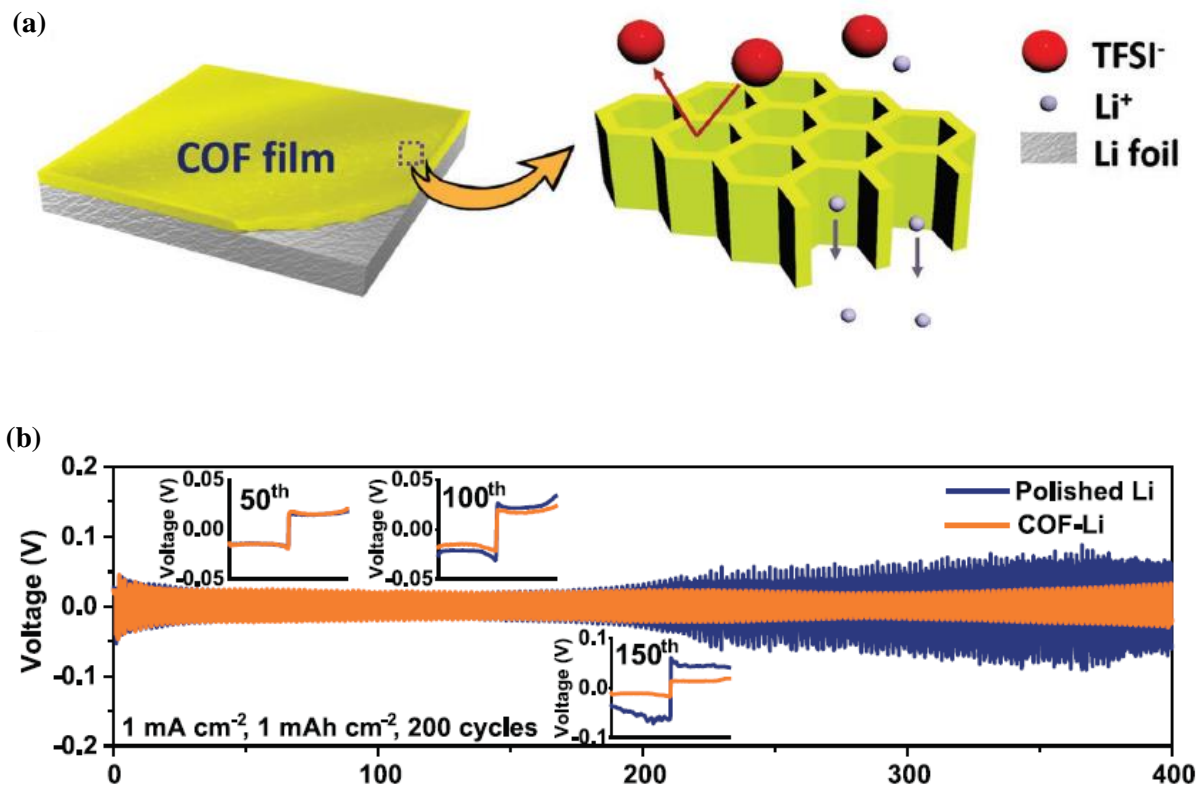
Figure 1. 13 (a) Schematic diagram of COF film showing its microporous structure and effect on Li plating/stripping, and (b) Voltage profile of Li symmetrical cells for polished Li and COF modified Li at current density of 1 mA cm^{-2} reaching to the capacity of 1 mAh cm^{-2} [93]

In contrast to *ex-situ* formation of ASEI, the *in-situ* ASEI are developed during battery cycling operations. Although, the approaches for *ex-situ* ASEI design have achieved remarkable breakthroughs in Li dendrite suppression, the economic feasibility due to complicated synthesis and processing routes proves to be a major drawback [34, 41-44]. On the other hand, employing advanced formulations in LEs to develop *insitu* ASEI such as introduction of additives [94-98], increasing electrolyte salt concentration [99-101], using dual-salt electrolyte [102, 103], and incorporating novel salt-solvents [104-107] have shown to be more cost-effective methodologies

that are grabbing high attention of researchers working in development of advanced LMBs with suppressed parasitic reactions and dendrite growth. Also, it is believed that the electrolyte additives provides missing component while forming interphases enabling advanced ASEI layer tailored by additives for enhanced LMB chemistries [108, 109].

Current commercial electrolytes such as carbonate-based ones generally show low electrochemical stability, with stable voltage window of only < 4.3 V (v/s Li/Li$^+$). This limit its applications in high voltage LMBs [104, 110, 111]. Similarly, the ester based electrolytes form unstable SEI film at LMA surface leading to continuous electrolyte decomposition and Li inventory loss [41, 44, 112-121]. Compared to these electrolytes the ether based electrolytes shows enhanced Li metal modification by forming stable SEI layer and effective dendrite inhibition [122-125]. Although ether based electrolytes hold promising prospects in realizing LMBs with stable SEI and dendrite suppression, they still show poor oxidation stability of only 3.7 V when paired with high voltage cathodes [121, 126-131]. Therefore, it is important to understand the match of electrolytes/electrodes and use of electrolyte additives for realizing high voltage > 4.3 V LMBs.

Nitrate based electrolyte additives such as RNO$_3$ (R = Li, Na, K, La, and Cs) [101, 132-136] along with other additives such as phosphorous pentasulfide (P$_2$S$_5$) [137], and lithium iodide (LiI) [138], have shown to mitigate the polysulfide shuttle effect in lithium-sulfur (Li-S) batteries by passivating LMA surface via enhanced SEI layer. Similarly, materials such as NaNO$_3$ [98], and LiNO$_3$ [139, 140] were used as additives in ether-based and carbonate-based electrolytes for long-term cycling performance of LIB and LMBs, respectively. Although it is known that SEI layer plays a vital role in enhancing battery performance, the exact knowledge of part played by electrolyte additives to tune the composition of this layer is still insufficient.

In our recent study, inclining to superior nitrate anion chemistry against Li metal, gadolinium

nitrate $(Gd(NO_3)_3)$ as an electrolyte additive in ether based LEs is introduced. Gadolinium (Gd)

has been used as protective coating layer in various metal and metal alloys [141]. The additive

reaction of these metals with (Gd) contributes to form a coating layer that improves the tensile

strength, enables high temperature operation, and provides corrosion resistance to these metal

and metal alloys products. Along with it Gd are also used as electrolyte in solid oxide fuel cells,

which shows high ionic conductivity at low operating temperatures. These properties of Gd are

observed to be propitious to form an enhanced ASEI layer with low resistance, high Young's

modulus, and ionic conduction. Figure 1.14 shows the schematics of $Gd(NO_3)_3$ as electrolyte

additive alters the morphology of Li deposition and suppresses growth of dendritic and dead Li

on the surface of LMA for prolonged cycling. The results and analysis on this work will be

extensively discussed in future chapters.
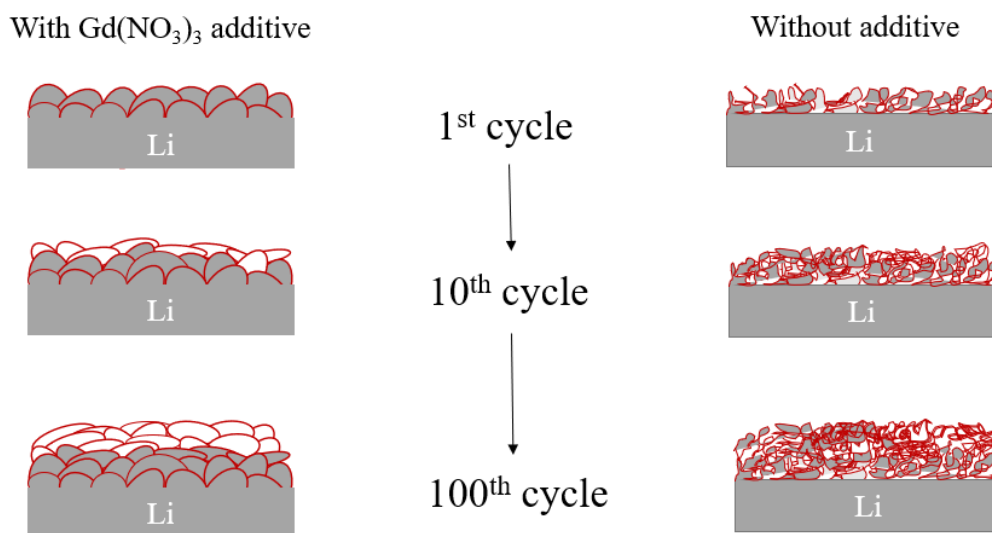
Figure 1. 14 Schematic showing nodular morphology of Li plating/stripping enabled by use of

$Gd(NO_3)_3$ as electrolyte additive in ether based LE.

1.3.1.3 SSE design for dendrite suppression

As discussed earlier, fragile SEI with low Young's modulus will crack under continuous cycling and this will get even worse at high current densities. Fresh Li will be exposed to the electrolyte from these cracks resulting in high electronegative hotspots regions. In these regions the Li will nucleate and morph into dendritic structure. Therefore, designing SSE with high Young's modulus values is essential to suppress dendrite growth and prevent Li side reactions. Moreover, the threshold value of 6 GPa is required to effectively suppress the Li dendrite growth [142]. In order for practical application, the SSE design not only should meet the criteria of high Young's modulus but also should possess properties such as sufficient Li ion conductivity, wide electrochemical stability window, and low interfacial impedance at the electrode/electrolyte interface. The Young's modulus of most inorganic ceramics based electrolytes ranges from tens to hundreds of GPa, which is much higher than the threshold value of 6 GPa and is sufficient for dendrite suppression. Table 1.2 summarizes ionic conductivity, Young's modulus, and electrochemical stability values for different SSE.

However, highly rigid materials cannot form good adhesion at the interface so they suffer from high interfacial resistance due to interfacial mismatch [143]. On the other hand, solid polymer based electrolytes shows lower ionic conductivity and moderate Young's modulus. As a result they cannot effectively suppress the growth of Li dendrites [144]. However, their adhesion with electrodes are much better compared to ceramics. Therefore, continuous research efforts are being made to improve the ionic conductivity of polymer solid electrolytes. One of the popular strategies is to construct polymer-inorganic composites that inherits advantages of both inorganic ceramics and polymer solid electrolytes. However, the ratio of this mixture is extremely important to obtain the maximum benefits from both types of SSE. For instance, it has

been shown that ceramic loading of < 10 vol. % can increase the ionic conductivity but at level

over 30 vol. % the conductivity will start to decrease, as compared to original polymer SSE

[145]. In recent developments, higher ceramic loadings of > 50 wt. % was shown to improve the

overall performance of solid-state batteries (SSB) [146, 147]. Similarly, inorganic compounds

such as Al_2O_3, SiO_2, Fe_2O_3, etc. have also been blended with polymer matrix to reduce its

crystallinity and enhance the ionic conductivity by providing additional pathways for Li ion

transport.

Table 1. 2 Summary of ionic conductivity, modulus and electrochemical stability window of

different SSE [34].

SSE materials	Ionic conductivity at 25 °C (mS cm^{-1})	Young's modulus (GPa)	Electrochemical stability window (V)	References
Li_2S-P_2S_5	~ 0.3-3	~18-25	1.71-2.31	[148-151]
$Li_{10}GeP_2S_{12}$	~12	~20	1.71-2.14	[151-153]
$Li_{3x}La_{2/3-x}TiO_3$	~1	~190-260	1.75-3.71	[153-155]
$Li_7La_3Zr_2O_{12}$	~0.8	~150	0.05-2.91	[156-158]
Li_3N	~1	~150	0-0.44	[159, 160]
LIPON	~0.001	~77	0.68-2.63	[161, 162]
PEO/Li salt	0.001-0.1	<0.1	~5 (Li compatible)	[163-165]

1.3.2 LMA and SSE interfacial engineering

As the ceiling of energy density allowed by commercialized graphite chemistry is almost met,

any effort to push it higher will face the safety risks imposed by highly flammable organic

electrolyte solvent. Use of LMA provides the solution as it has potential to achieve very high

energy density batteries. However, very low electronegativity also makes Li metal violently

reactive when in contact with almost any known LE. Therefore, to realize a high-energy density

battery with safe operations it is necessary to replace LEs with incombustible fast ion

conductors. SSBs that consists of SSEs have such potential as long as they are chemically stable

with Li metal and high capacity cathodes, and expertly conducts Li ions [166, 167]. Further, the

use of SSE can enable stackable battery design with increased volumetric energy density [168].

Different types of solid ion conductors have been investigated, ranging from sulfides to oxides

and oxynitrides such as perovskite [169], antiperovskite [170], LISICON [171], thio-LISICON

[172], NASICON [173], garnet [156], sulfide glass ceramic [152, 174, 175], etc. Solid sulfide

electrolytes are known for their high ionic conductivity e.g., LGPS sulfide SSE with room

temperature (RT) conductivity above 1 mS cm^{-1}. However, most sulfide electrolytes are unstable

in moisture generating highly toxic H_2S gas. Also, they are thermodynamically unstable against

LMA and high voltage cathodes [151, 176-178]. Similarly, phosphate based solids such as

LiPON [161, 179] and LATP [180, 181] are unstable against LMA forming redox reaction

products at the interface (e.g., Ti^{4+}/Ti^{3+} redox reaction). Among these garnet SSE, such as

$Li_7La_3Zr_2O_{12}$ (LLZO), shows high ionic conductivity around 1 mS cm^{-1}, has wide

electrochemical window, and are stable chemically against LMA [182, 183]. The comparison

between different SSEs are shown in radar plots of Figure 1.15 (a-f) [184].
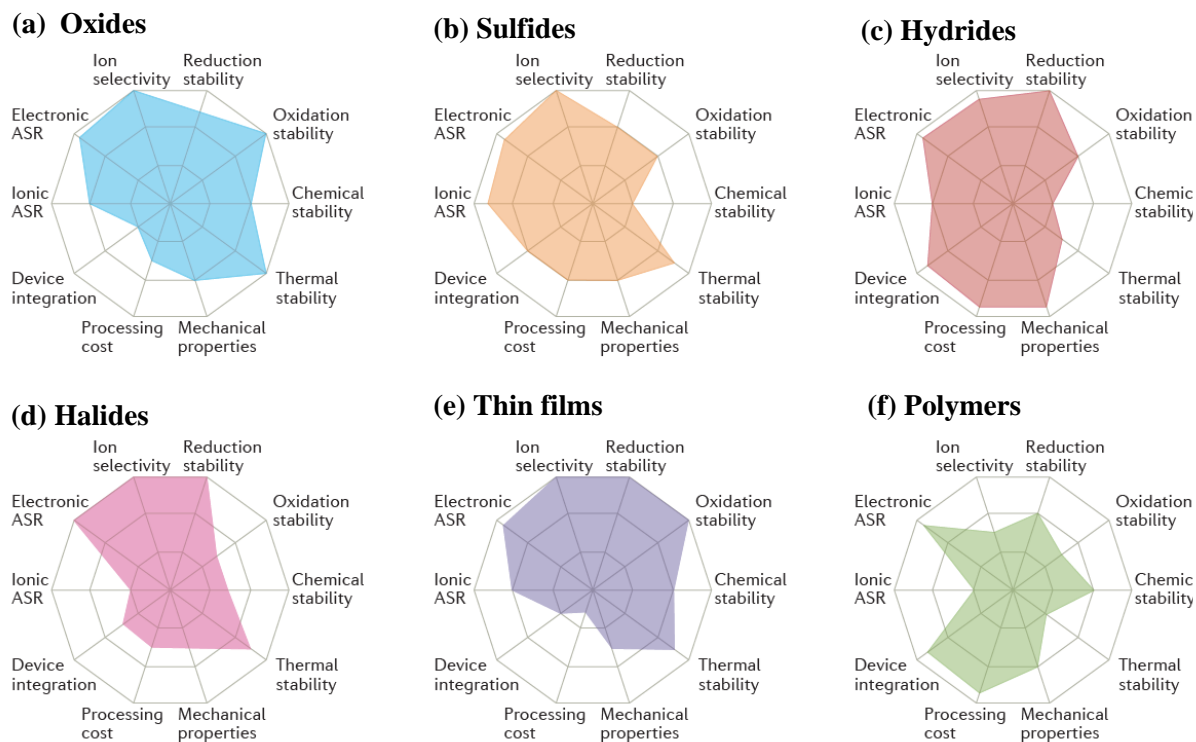
Figure 1. 15 (a-f) Radar plots showing performance characteristics of different SSEs [184].

However, garnet type LLZO SSEs are not lithiophilic as Li metal do not wet their surface very well [185-187]. The poor physical contact arising from microscopic voids and gaps that are common at solid-solid interfaces leads to high interfacial resistance ($\sim 10^3$ Ω) and nonuniform current distribution at the interface. These conditions will result in dendritic infiltration of Li in the SSE and poor cycling performance. The poor interfacial contacts are also partly due to the presence of insulating contaminants such as lithium carbonate (Li_2CO_3) and lithium hydroxide (LiOH) on the garnet surface [188-191]. Therefore, to obtain stable cycling in LLZO based SSBs their wetting behavior with LMA should me improved, and the resistance at the interface must be decreased. Various strategies such as using electrolyte additives , thermal pressing, modifying

electrolyte surface and interfaces are popular to reduce interfacial resistance at LMA/LLZO interface. Among them introducing interfacial buffer layers are proven effective. Buffer layers such as metals (e.g. Au [192], Al [187], Si [193], Ge [194], Mg [195]), metal oxides (e.g. Al_2O_3 [196], ZnO [197]), carbon materials (e.g. graphite [198]), and metal nitrides (e.g. Li_3N [199], Si_3N_4 [200]) have shown to significantly reduce resistance and ensure intimate contact at the interface. Some of the popular and effective strategies to address interface incompatibilities at LMA/inorganic interfaces SSE are described below.

1.3.2.1 LMA/Sulfide SSE interface

Although sulfide based inorganic SSEs possess high ionic conductivity, they are chemically unstable against Li metal. This instability leads to formation of insulating decomposition products with high electronic conductivity at the interface promoting dendritic growth and Li infiltration in the SSE bulk. One of the pioneering works done to reduce the electrochemical reduction of sulfide SSE at the LMA interface was to introduce a lithium alloy coating with higher reduction potential. However, some of this coating layer has shown to significantly reduce the deliverable maximum cell energy density. Several other approaches have been investigated which are discussed further.

Coating of protective layers at the LMA/sulfide SSE interface has been a very popular method to stabilize the sulfides and prevent migration of electronic reactants into the SSE bulk. As shown in Figure 1.16 (a), Xu et al. introduced bilayer of LiF or LiI as the interface layer and used methoxyperfluorobutane (HFE) solution to penetrate into the SSE [201]. The bilayer stabilized the highly unstable sulfides and the infiltration of HFE prevented growth of Li dendrites (Figure 1.16 (b)). As a result, the interface modified Li symmetrical cells showed very low interfacial

resistance and LCO cathode assemble full LMB exhibited reversible capacity of 118.9 mAh g^{-1} with retention of 96.8 mAh g^{-1} after 100 cycles (Figure 1.16 (c,d))
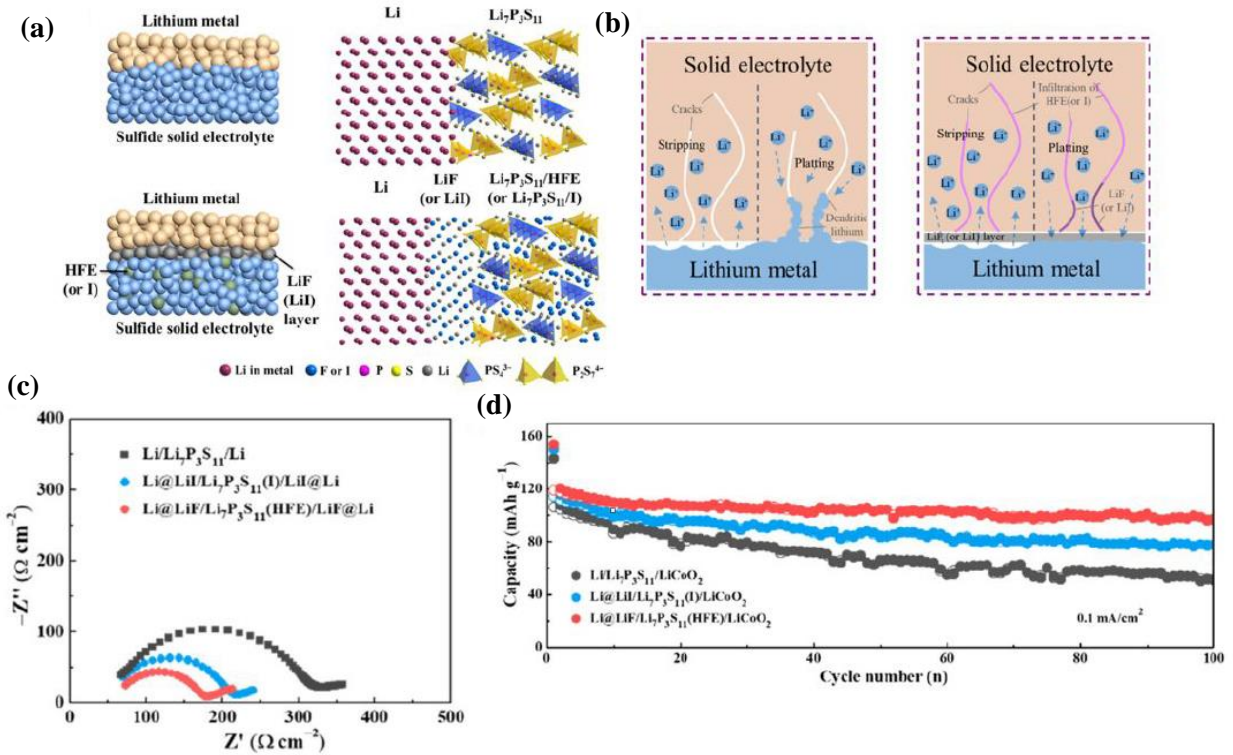
Figure 1. 16 (a) Schematic showing the interface engineering using LiF (or LiI) layer and HFE solution infiltration, (b) Schematic showing Li plating/stripping behavior of interface modified Li metal compared to bare Li metal, (c) Nyquist plots showing resistance values of different Li symmetrical cells, and (d) Full cell cycling performance of LCO based SSB at current density of 0.1 mA cm^{-2} and temperature 25 °C. [202]

Similarly, some other interfacial layers deposited at the LMA/sulfide SSE interface and the process used for such deposition to achieve interface stability and enhanced Li plating/stripping as well as improved full cell cycling are listed in Table 1.3.

Table 1. 3 List of different coating layer at LMA/sulfide SSE interface.

S.N.	Interfacial Layer	Coating Process	References
1	Gold (Au) thin films	Thermal evaporation	[203]
2	Indium (In) thin films	Vacuum evaporation	[204]
3	$3LiBH_4.LiI$ in THF	Chemical deposition	[205]
4	LiH_2PO_4	Spin coating	[206]
5	Alucone	Molecular layer deposition (MLD)	[207]
6	$(LiO-(CH_2O)n-Li)$ & $(LiF, -NSO_2-Li, Li_2O)$ nanocomposite	*In-situ* electrochemical reduction	[208]
7	Lithium bis(trifluoromethane sulfonyl) imide	Drop casting	[209]

Furthermore, some other methods used to stabilize the LMA/sulfide SSE are: (1) elemental substitution/doping of sulfide particles, (2) Solution processing of sulfide electrolytes, and (3) Hybrid of polymer and sulfide electrolytes.

1.3.2.2 LMA/Oxide SSE interface

As discussed earlier, the garnet-type oxide SSE have lowest reduction potential compared to Li metal and also they possess the most thermodynamically stable interface with Li [187]. However, the rigid ceramic nature of garnet makes it difficult to wet Li on its surface leading to large interfacial resistance. A simple method of using ~ 2 µl of LE (1M $LiPF_6$ in ethylene

carbonate (EC)/diethyl carbonate (DMC)/diethyl carbonate (DEC) at volume ratio of 1:1:1) at the interface between $Li_{1.4}Al_{0.4}Ti_{1.6}(PO_4)_3$ (LATP) SSE pellet and Li metal have shown to reduce the interfacial resistance from 1000 Ω to 275 Ω [210]. However, the hybrid nature by adding LE would compromise the advantages of a solid-state interface.

Another popular practice is applying pressure and heat to attach Li foil onto the garnet pellet. Wang and Sakamoto from University of Michigan analyzed the relationship between interfacial resistance and adhesive pressure applied by testing Li| LLZO| Li symmetrical cells [211]. In this study, the lowest interfacial resistance of 7 Ω cm^2 was observed for adhesion pressure of 8 MPa. Similarly, approach of heat infusion or melting of Li metal on top of garnets have also been performed in order to obtain good contact at the interface. Nonetheless, this process always leaves small, microscopic interfacial gaps and voids. Thus, to achieve an optimal method to reduce the interfacial resistance, several methods have been investigated.

Coating the surface of LLZO to convert it from lithiophobicity to lithiophilicity has been widely explored to establish intimate surface contact at the Li metal/ LLZO interface. As shown in Figure 1.17 (a), a very minimalist and simple method of pencil drawing the graphite layer on the top of tungsten (W)-doped garnet $Li_{5.9}Al_{0.2}La_3Zr_{1.75}W_{0.25}O_{12}$ (LALZWO) pellet was demonstrated by Shao et al. [198]. The melt infusion of Li metal onto the interface modified LALZWO pellet led to formation of lithiated graphite (LiC_6) which improved the wettability of Li metal on the garnet surface (Figure 1.17 (b)). This interaction led to decrease in interfacial resistance from 1250 to 105 Ω cm^2 (Figure 1.17 (c)). Similarly, the interface modified Li symmetrical cells and full cells with NCM523 cathode showed better cyclability and excellent stability (Figure 1.17 (d-f)). Further, some other interfacial coating layers deposited at the

LMA/garnet SSE interface and the process used for such deposition to achieve interface stability

and enhanced Li plating/stripping as well as improved full cell cycling are listed in Table 1.4.
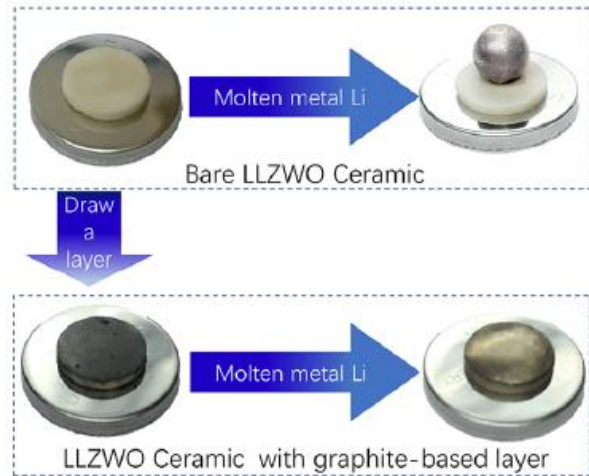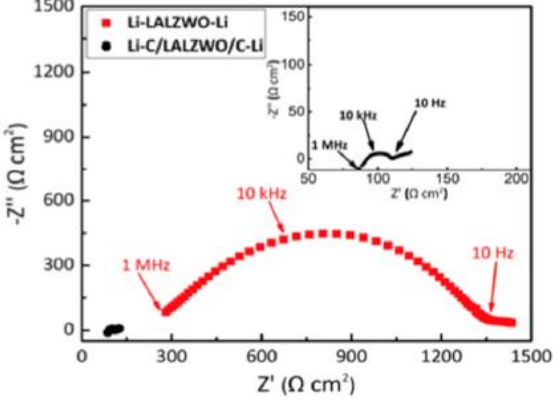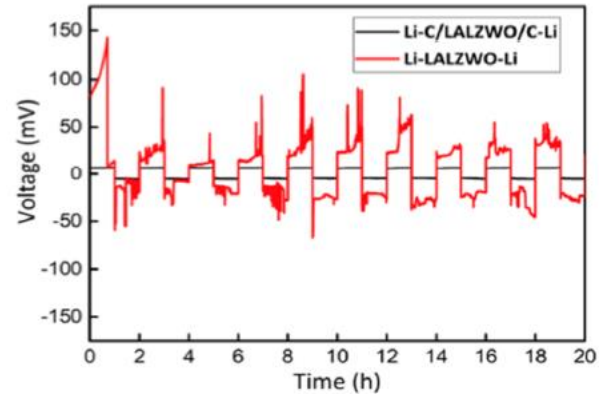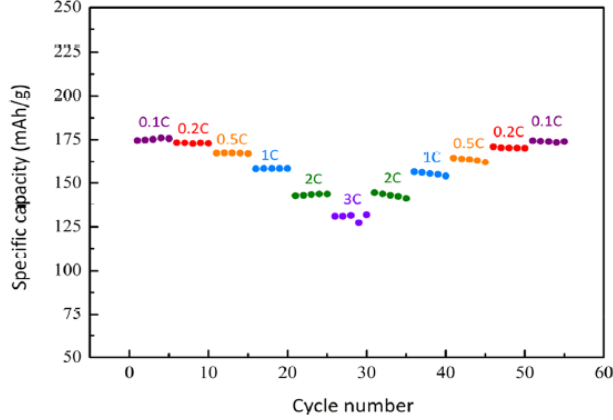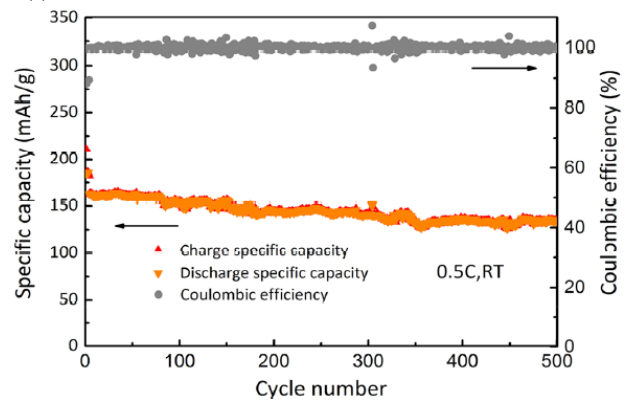
Figure 1. 17 (a) Digital photo showing pencil drawing of interlayer on garnet surface, (b) Wettability test of melt infused Li on the top of LALZWO surface with and without graphite layer, (c) Nyquist plot showing difference in interfacial resistance, (d) voltage profile of Li symmetrical cell tests for with and without graphite interface layer, (e) rate capability test of NCM523/ LMA full cells at various C-rates, and (f) Cycling performance of NCM523/ LMA full cells at 0.5 C in RT [198].

Table 1. 4 List of different coating layer at LMA/garnet SSE interface.

S.N.	Interfacial Layer	Coating Process	References
1	Li-Al alloy	Dip coating	[212]
2	Amorphous Silicon (Si)	Plasma enhanced chemical vapor deposition (PECVD)	[193]
3	Germanium (Ge)	Electron beam (Ebeam) evaporation	[194]
4	Alumina (Al_2O_3)	Atomic layer deposition (ALD)	[196]
5	Thin Al layer	Ebeam evaporation	[187]
6	Magnesium (Mg)	Sputtering	[195]
7	Zinc Oxide (ZnO)	ALD	[197]
8	Lithium Nitride (Li_3N)	PECVD	[199]
9	PEO-PAS gel-solution	Drop casting	[213]
10	Soaking LE in PVDF-HFP polymer matrix	Stacking freestanding gel-polymer electrolyte	[214]

Additionally, some other methods used to stabilize the LMA/garnet SSE are: (1) surface polishing to remove air-exposed oxides such as Li_2CO_3 and $LiOH$, (2) controlling the microstructures of grains and grain boundary, (3) introducing electrolyte additives, and (4) designing 3D conductive framework.

1.4 Motivation

To fulfill the requirement of high energy density LMBs ~ 500 Wh kg ^{1}, there is an urgent need to stabilize the Li metal for its safe use. However, unrestrainable growth of Li dendrites and formation of unstable SEI undermines the potential and impedes the commercialization of LMBs. On the other hand, use of LE is imposing the safety hazards while attempting to push the energy density (Wh kg^{-1}) and volumetric density (Wh l^{-1}) of LMBs higher. Therefore, a facile and all-around strategy to implement dendrite free LMA, and superior cycling stability of SSBs are of the essence.

1.5 Objective

The objective of this dissertation is to accomplish a dendrite-free Li metal deposition and stabilized LMA/SSE interface which will ensure outstanding performance and safe use of LMBs. Two approaches will be studied along the dissertation about research on: (1) using novel nitrate salt based functional electrolyte additive in ether solvent based electrolyte that promotes plating/stripping of Li metal in nodular morphology, thus, significantly suppressing the growth of dendritic and dead Li on LMA surface promoting the formation of stable SEI, enhancing the cycle life, and overall stability of LMBs. (2) a facile and effective strategy to significantly reduce the interfacial resistance at LMA/garnet SSE interface by depositing metal nitride interfacial layer on garnet SSE, enhancing the plating/stripping cycles of solid-state Li symmetrical cells and augmenting the rate capability and electrochemical stability of a hybrid SSB.

For achieving abovementioned objectives, following tasks were performed:

1. Use of novel electrolyte additive, gadolinium nitrate ($Gd(NO_3)_3$) in $LiTFSI-LiNO_3$ ether solvent based electrolyte.

   a. Preparing the baseline $LiTFSI-LiNO_3$ ether solvent based electrolyte without use of new additive.

   b. Optimizing the molar amount of electrolyte additive in the ether based electrolyte.

   c. Coating cathodes and preparing Li anodes for fabricating electrochemical cells.

2. A new method to coat $Li_{6.25}Al_{0.25}La_3Zr_2O_{12}$ (Al-LLZO) garnet SSE with a highly ion-conductive and lithiophilic silicon nitride (Si_3N_4) and use it as an interfacial layer between LMA and garnet SSE.

   a. Preparing Al-LLZO garnet solid electrolyte pellets with high ionic conductivity (powder metallurgy method).

   b. RF sputtering an ultrathin film layer of Si_3N_4 on Al-LLZO garnet pellet (physical vapor deposition method).

   c. Optimize the Si_3N_4 layer thickness for achieving superior plating/stripping cycle performance.

   d. Melt infuse Li metal onto the interfacial layer deposited pellet samples to fabricate Li symmetrical cells and use cathode coated on current collector to assemble full cells.

3. Optimize the experimental conditions for sample preparation and lab equipment operation.

4. Conduct morphological, structural, and imaging characterizations using X-ray diffraction (XRD), Raman spectroscopy, X-ray photoelectron spectroscopy (XPS), atomic force microscopy (AFM), and field emission scanning electron microscopy/energy dispersive spectroscopy (FESEM/EDS).

5. Perform electrochemical characterization using electrochemical impedance spectroscopy (EIS), linear sweep voltammetry (LSV), cyclic voltammetry (CV), Li symmetrical cell and full cell test.

1.6 Organization of the Dissertation

Chapter 1 provides the introduction on the subject and background on energy sources, consumption and crisis. It further describes the importance of renewable energy resources and energy storage systems, providing information on how energy storage system is vital to realize high penetration of renewables in global energy consumptions. A comprehensive review, describing numerous literatures on LIB history, its importance and current research direction is provided. In addition, a detailed literature review on significance of LMBs, problems associated with LMAs, strategies for Li metal protection and some of our previous studies on ASEI development and 3D current collector design for Li dendrite suppression are explained. The next part of this chapter describes the LMA and SSE interfacial engineering. It starts by explaining different types of solid-state ionic conductors, their properties and key challenges associated with each of them. The characteristics of LMA/SSE interface, their key challenges and solution method are provided. As last part of this chapter the motivation and objectives for this dissertation work are listed.

Chapter 2 discusses the theory behind working principle of LIBs, providing an understanding of different battery components and specifications. Theories on Li dendrite growth and methods to

38

stabilize LMA are provided. Also, the mechanism of ion transport in SSE, and processes occurring in their electrode/electrolyte interfaces are explained. Further, different material and electrochemical characterization techniques are described.

Chapter 3 provides details on experimental procedures of materials and sample preparations for nitrate salt electrolyte additive and metal nitride SSE interlayer works. Further, it describes sample preparation and processing for various materials and electrochemical characterization techniques that were carried out to study the properties of electrolyte additive enhanced *in-situ* SEI, metal nitride deposited interlayer and their effects on battery stability and cycling performance.

Chapter 4 gives details about all the results and discussions obtained from morphological and electrochemical characterization of electrolyte additive engineered LMAs, and metal nitride interfacial layer engineered LMA/SSE interfaces. The materials characterizations and optimization procedures of experimental conditions are described. Further, the results obtained from these characterizations are thoroughly analyzed.

Chapter 5 is the summary of all of the dissertation work on additive and interface engineering and provides its significance. It also gives the specific conclusions obtained from different analytical works performed throughout this dissertation. Further, some future works mainly focused on market adoption and commercialization are provided.

Chapter 2: Theory

2.1 How does LIBs work?

2.1.1 Battery components

As shown in Figure 2.1 (a), a LIB consists of anode, cathode, separator, electrolyte and current

collectors (positive and negative). Anodes and cathodes are at two ends of a battery and their

purpose is to store Li ions. In LIBs, anodes are generally made up of carbon and cathodes are

made from Li metal oxide chemical compound. The electrolyte consists of Li salts dissolved in

organic solvents. During battery operation the electrolyte carries positively charged Li ions from

cathode to anode and vice-versa (charging/discharging) through a polymeric separator. The

separators are made of porous polymer materials which only allows the flow of positive ions

blocking electrons in order to prevent short circuiting. The movement of Li ions through the

electrolyte creates free electrons, which during discharge (Figure 2.1 (b)) flows from negative

current collector through a device being powered (e.g., cell phone, tablet, etc.). During charging

(Figure 2.1 (c)), the exact opposite process occurs. A power source is attached, and the Li ions

moves back from cathode to anode creating electric field which allows electrons to move from

anode to cathode.

(a)
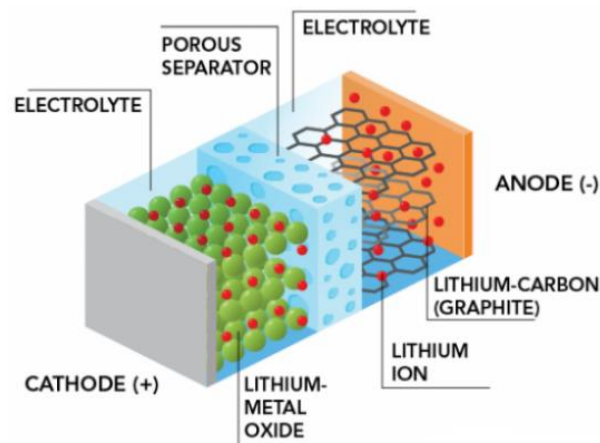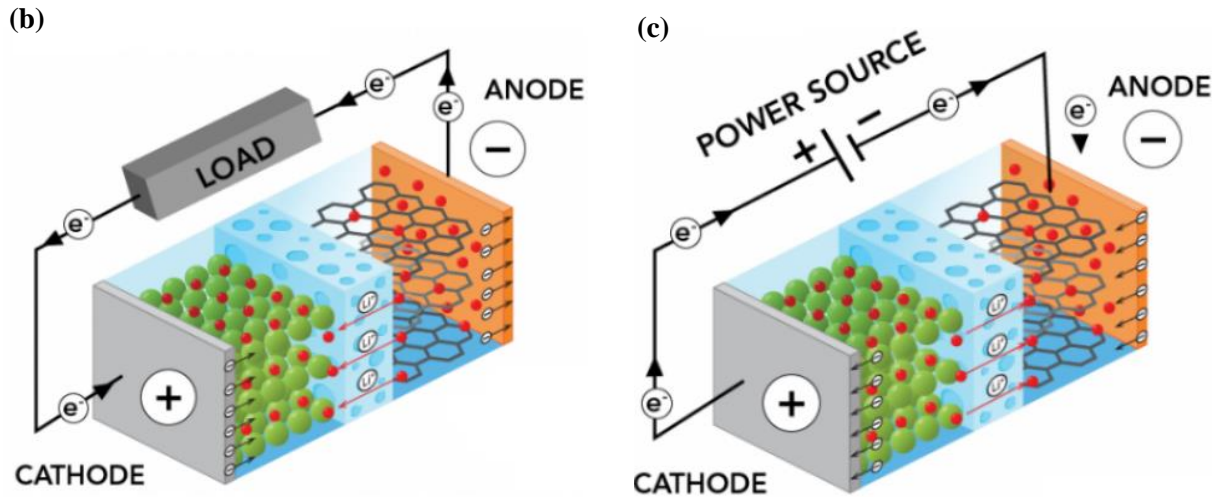
Figure 2. 1 (a) Components of a LIB, (b) LIB discharging , and (c) charging [215].

Similarly, several other components make up a battery pack, which comprises of more than one Li ion cells. Some of them are: (1) temperature sensor to monitor the battery temperature during operation, (2) voltage regulators to keep voltage and currents at safe limits, (3) battery management system (BMS) is a minicomputer that maintains overall battery operation preventing overcharging and ensuring safety.

2.1.2 Working chemistry

The chemistry involved during charging of a typical commercialized graphite (anode)/lithium cobalt oxide ($LiCoO_2$) (cathode) LIB is shown in Figure 2.2. Other materials in a LIB are electrolyte with Li salt dissolved in organic solvent (e.g., lithium hexafluorophosphate ($LiPF_6$) in ethylene carbonate (EC) and diethyl carbonate (DEC)), polymer separator membrane (e.g., polypropylene (PP)), positive (Aluminum (Al)), and negative (Copper (Cu)) current collectors. The main chemical reactions that undergo within the cell are typically reversible Li ion intercalation-de-intercalation reaction cycles between two layered compounds.

41
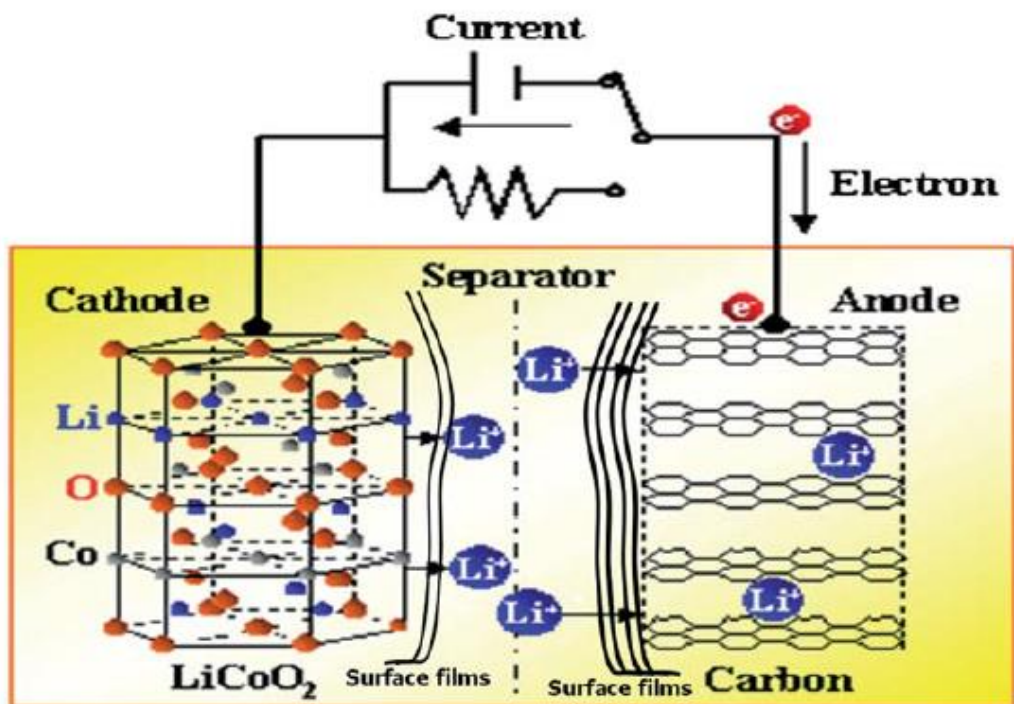
Figure 2. 2 Schematic of typical LIB based on graphitic anode and $LiCoO_2$ cathode showing involved electrochemistry [216].

The source of Li in most of LIBs are the cathode materials, in contrast to LMBs where LMA serves as a reservoir of Li. In charging process for $LiCoO_2$ based cathode material, the oxidation or delithiation of $LiCoO_2$ (equation 2.1) occurs. At the mean time the reduction or lithiation of graphite occurs (equation 2.2) at the anode, forming LiC_6 as the product. The intercalation of Li ions into graphite occurs in various transition stages such as LiC_{24}, LiC_{27}, and LiC_{12} which is governed by first-order phase transition process [217]. This process will form passivating films (SEI) at the electrode surface to cease further irreversible reaction stages and stabilize the condition for forming Li_xC_6 stage [218]. Thus, one limiting factor to minimize the reversible charge consumption is the availability of excess Li ions in the cathode material that is required to

form the passivating surface films on the graphite anode. Further, during discharge process the reverse chemical reaction occurs and Li ions travel back to cathode (equation 2.3, 2.4).

$$LiCoO_2 \rightarrow Li_{1-x}CoO_2 + xLi^+ + xe^- \qquad (2.1)$$

$$6C + xLi^+ + xe^- \rightarrow Li_xC_6 \qquad (2.2)$$

$$Li_{1-x}CoO_2 + xLi^+ + xe^- \rightarrow LiCoO_2 \qquad (2.3)$$

$$Li_xC_6 \rightarrow 6C + xLi^+ + xe^- \qquad (2.4)$$
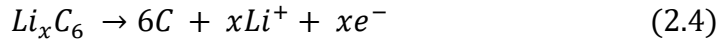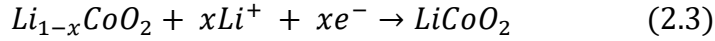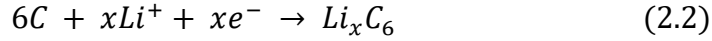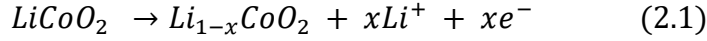
2.2 Understanding Battery specifications

Not all batteries are created equal, even if they follow same chemistries. So, it is very important to understand the terminologies that are used to describe, classify, and compare different kinds of batteries. The knowledge of these specifications will provide a basic background for defining the parameters used for battery operating conditions and describing the manufacturers specifications used for characterizing a battery.

2.2.1 Cell Voltage

The electromotive force (EMF) is defined as the potential difference across the terminals (anode/cathode) of a battery when no current is drawn and depends on its state of charge. Or in other words it can also be characterized as open-circuit voltage, which is the voltage across battery terminals with no load applied. The EMF of a particular cell quantitatively measures the likelihood of the cell reaction to occur and is related to the free energy change for the process. The free energy variation related to one mole of reaction defines the maximum work and is given by equation 2.5.

$$\Delta G^0 = -zFV^0 \qquad (2.5)$$

where z is the number of moles of electrons transferred per one mole of reaction, F is the Faraday's constant (F = 96,487 C mol^{-1}), and V^0 is the standard EMF. When there is different conditions other than the standard, the cell voltage (V) is given by the Nernst equation (2.6).

$$V = V^0 - \left(\frac{RT}{nF}\right) \ln(a_i) \hspace{2cm} (2.6)$$

where a_i gives the activity of the relevant species e.g., Li, R is the universal gas constant, and T is the absolute temperature.

This change in the standard free energy, $\varDelta G^0$ of a cell reaction as defined by Nernst equation drives the battery and makes it capable to deliver electrical energy to external circuit. Further, not only the changes in free energy, but data on entropies, enthalpies, activity coefficients, equilibrium constants and solubility products can be obtained by measuring EMF.

Similarly, some other voltage terminologies related to battery are: (1) terminal voltage, which is the voltage between the battery terminals with applied load, (2) nominal voltage, which is the reported or reference battery voltage, (3) cut-off voltage, is the minimum allowable or threshold voltage of a battery.

2.2.2 Specific capacity

The amount of charge stored by applying current (I) for a particular period of time (t) is defined as the capacity (Q) and given by the equation (2.7).

$$Q = I \times t \hspace{2cm} (2.7)$$

Similarly, the specific capacity of an electrode is defined as the amount of charge that can be stored per its unit mass and is given by equation (2.8).

$$Specific\ Capacity\ (SC) = \frac{F \times z}{M \times 3.6} \qquad (2.8)$$

where, F is the Faraday's constant, z is the number of electrons transferred per mole, and M is the molar mass of the active material.

2.2.3 Energy density

The product of average voltage and the capacity (Wh) gives the energy delivered by a battery. Then, energy density is the maximum energy delivered by the battery per unit mass, including the weight of the non-energy-producing components such as packaging and cell construction materials. Mathematically, energy density is given by the integration of average voltage range and specific capacity of a battery (equation (2.9)).

$$Energy\ density\ (Wh\ kg^{-1}) = \int V\ dSC \qquad (2.9)$$

2.2.4 Power density

The power density of a battery is defined as its maximum available power per unit volume, volumetric power density (W L^{-1}) or mass specific power density (W kg^{-1}). Power density is the characteristic of both battery chemistry and packaging. It is calculated by multiplying the cell voltage by current density for charge/discharge. In physical sense, it determines the battery weight or size required to achieve a given performance target.

2.2.5 C and E- rates

While describing charging/discharging current of a battery it is often expressed in terms of C-rate which is a normalized value against battery capacity. So, a C-rate can be defined as the rate at which a battery is being charged/discharged relative to its maximum capacity. For e.g., a 1C charging rate means that the applied charge current will charge the entire battery in 1 hour. So, if

1C charging rate is applied to a battery with capacity of 100 Ah, this will equate to charging current of 100 A and it will take 1 h to fully charge the battery. Similarly, E-rate is related to the charge/discharge power. For e.g., a 1 E-rate of charge is the charging power applied to completely charge the battery in 1 h.

2.2.6 Depth of discharge

The depth of discharge (DOD) (%) is defined as the percentage of discharged battery capacity relative to maximum capacity percentage. Generally, a discharge of at least 80 % DOD is defined as a deep discharge.

2.2.7 Maximum continuous discharge current

The maximum current defined by the battery manufacturer at which the battery can be continuously discharged is known as maximum continuous discharge current. This discharging current limit is defined in order to prohibit excessive discharging rates that can damage the battery and reduce its capacity.

2.2.8 State of charge and health

The state of charge (SOC) of a battery is defined as the ratio of remaining charge capacity ($Q(t)$) of it at any given time (t) to its total usable capacity (Q_{total}) in a fully charged state. It is given by equation (2.10).

$$SOC(t) = \frac{Q(t)}{Q_{total}} \qquad\qquad (2.10)$$

Accurate estimation of battery SOC can maximize the battery performance by protecting it from overcharge/discharge. In an electric vehicle, the SOC provides the measure of the amount of electricity stored in its battery. This parameter is analogous to the fuel gauge installed on the conventional internal combustion engine vehicles.

Similarly, the state of health (SOH) is defined as the condition of the battery life between the beginning and end of life percentage. The beginning of battery life is the point at which battery operation begins and its end of life is the point at which it cannot perform according to a predefined minimum requirement. SOH is mathematically represented as ratio of instantaneous total capacity at any given time (t) to the capacity of a new battery (equation (2.11)).

$$SOH\ (t) = \frac{Q_{total}(t)}{Q_{new}}$$
(2.11)

where Q_{total} (t) is the instantaneous total battery capacity at any given time t, and Q_{new} is the capacity of a new battery. The Q_{total} (t) value starts to decline over time as the battery starts aging by being in use.

2.2.9 Cycle life and Coulombic efficiency

The cycle life of a battery is defined as the total number of charge-discharge cycles it can undergo before it fails to meet a predefined performance criteria or end of life threshold. The operating cycle life of a battery is affected by the conditions such as rate of cycles, DOD, temperature and humidity. For e.g., higher the DOD, minimum will be the cycle life.

Similarly, coulombic efficiency (CE) is defined as the ratio of the battery discharge capacity to the charge capacity. This parameter is the indication of capacity loss of the battery in a cycle. So, CE of 100 % means that the capacity of the battery is reversible with no loss. On the other hand, CE < 100 % means that the battery experiences capacity loss that can be due to parasitic irreversible reactions between electrodes and electrolyte. CE can be used to determine the loss of battery capacity over cycle number. For e.g., a 0.1 % decrease in CE for each cycle will lead to 10 % capacity loss after 100 cycles.

2.2.10 Internal resistance

The internal resistance of a battery is defined as the resistance that is within the battery. The internal resistances are generally different during charging and discharging and is dependent upon the battery SOC. As the internal resistance of the battery increases, its efficiency decreases. Increase in internal resistance also reduces the thermal stability of the battery as more of the charge energy is converted to heat.

2.3 Theories on Li dendrite growth

Deposition of dendritic structure and its growth is somewhat a common occurrence not only in case of Li metal but also when electroplating metals such as Cu, Ni, and Zn at high current densities [219]. There are mainly two theories that have been reported explaining the mechanisms governing the Li dendrite growth on metal surfaces: (1) space charge layer theory, and (2) theory of non-uniform SEI formation.

2.3.1 Space charge theory

Space charge theory describes that at higher current densities, as there is rapid Li ion flux, cations are consumed rapidly in the Li metal electrode, this causes sharp concentration depletion leading to formation of local space charge layers with strong negative electric field [220]. Large amount of Li ions will get electroplated in short time due to this strong electronegative field, causing formation of dendritic structures in LMA surface [41, 49, 50]. Figure 2.3, shows the density functional based tight biding (DFTB) model calculations for charge distribution on an uncharged and charged Li metal tips [221]. For an uncharged Li metal, the tip atoms create a positive potential which repels the Li cations approaching from the electrolyte solution, promoting deposition towards the side leading to inhibition of tip growth (Figure 2.3(a)). Whereas, for the charged one (Figure 2.3 (b)) the negative potential gradient is strongly directed

towards the tip which favors Li cations from the solution getting plated in it, favoring its further growth.
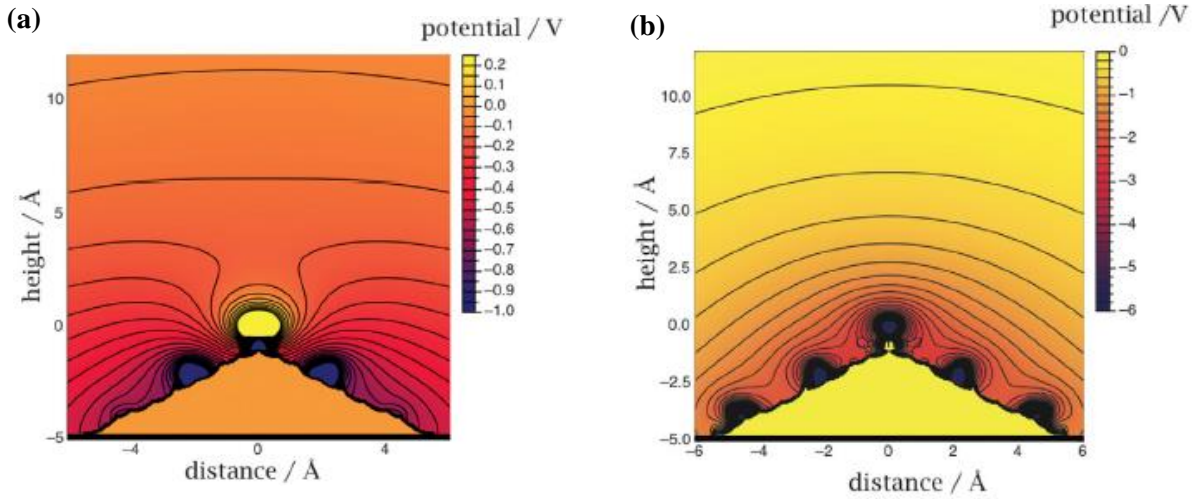
Figure 2. 3 DFTB model calculations showing electrostatic potential contours for (a) an uncharged Li metal electrode, and (b) a Li electrode with an excess charge of $\sigma = -2.9 \times 10^{-2}$ C m^{-2} [221].

The critical current density (J^*) is the current density at which electrical neutrality at the electrode surface starts to break and local space charge start to build up, causing amplified deposition of Li metal cations. The time required to reach J^* after which dendrites start to grow is called Sand's time (τ), and the process is called Sand's behavior of dendrite growth [42, 222, 223]. The Sand's time, equation (2.12) gives the time (τ) at which dendrite starts to grow or in other words time after which J^* cannot be sustained.

$$\tau = \pi D \left(\frac{e C_0}{2 J t_a} \right)^2 \tag{2.12}$$

$$V_{tip} = \frac{JV}{F} \tag{2.13}$$

where *J* gives the effective current density at the electrode surface, *D* is the ambipolar diffusion coefficient, *e* is the value of electronic charge, C_o gives the initial Li salt concentration, and t_a is the anionic transference number [224]. Similarly, equation (2.13) gives the Li dendrite growth rate (V_{tip}) at the tip, where *J* is the current density, *V* is the molar volume and *F* is Faraday's constant [225]. This expression shows that at lower current density (*J*) the tendency of Li dendrite growth may get reduced.

2.3.2 Theory of non-uniform SEI formation

This theory explains that the Li dendrite growth is due to formation of non-uniform and fragile SEI in the Li electrode surface. Non-uniform SEI will lead to uneven current distribution which will affect the electric field distribution and ion flux at the electrode surface. This will favor electron accumulation at the tip which will promote preferential deposition of Li ions at it leading to further protruding growth instead of flat layer formation.

Similarly, a fragile SEI layer will crack under successive cycling and strain induced during electrode volume change. These cracks will expose fresh Li metal surface to the electrolyte solution forming high electronegative regions again promoting preferential deposition and electrolyte decomposition. Therefore, to prevent the occurrence of this phenomenon, the SEI layer should have properties such as : (1) high Young's modulus for suppressing dendrite growth and less prone to developing cracks, (2) high Li ion conductivity for promoting good Li ion transport, and (3) low electronic conductivity for impeding preferential or top surface deposition.

2.4 Electrolyte engineering for stabilizing LMA

Engineering of electrolyte, especially by using additives, have been extensively investigated to suppress dendritic growth and enhance LMA performance. The main principle behind using

electrolyte additives is that the components of these additives can get reduced, polymerize or adsorb on the Li metal surface, altering the physico-chemical behavior of the SEI leading to current distribution regulation during deposition of Li ions [226]. Additives that are used to modify the SEI layer should get reduced (anode additives) prior to the electrolyte reduction, thus passivating the electrode surface and preventing further electrolyte decomposition. It has been demonstrated that the Li deposition morphology and cycling efficiency can be altered by presence of additives even at millimolar (mM) amount.
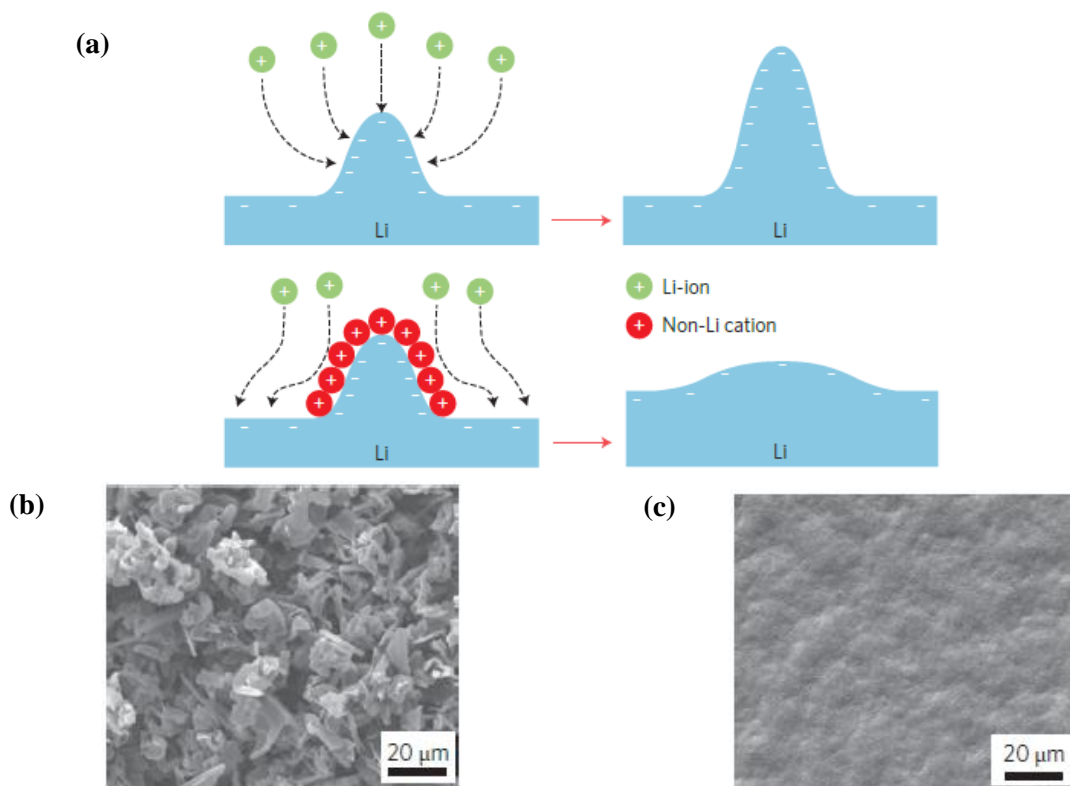
Figure 2. 4 (a) Schematic showing Li deposition process with presence of electrostatic shield [34], SEM images of cycled Li metal surface showing (b) Dendritic morphology for control electrolyte without additive, and (c) uniform surface for additive added electrolyte [227].

The change in Li deposition morphology is mainly attributed to formation of self-healing electrostatic shield enabled by reduction of electrolyte additives. Li deposition with no dendrites were obtained in carbonate based electrolyte by using Cs^+ and Rb^+ cation based salt as additives [227, 228]. Inclining to Nernst equation, the reduction of these metal cations (M^+) before Li^+ reduction was attributed to their lower effective reduction potential below to that of Li^+. Therefore, these M^+ will adsorb first to the Li electrode surface during Li deposition forming an electrostatic shield (Figure 2.4 (a)). This positively charged electrostatic field will repel the incoming Li^+ and thus suppressing the growth of Li protrusions and favoring more uniform deposition. Further, the SEM images of Figure 2.4 (c) shows significant improvement in Li deposition morphology compared to Figure 2.4 (b), when 0.05 M of $CsPF_6$ was using as additive in 1M $LiPF_6$/propylene carbonate (PC) electrolyte [227].

2.5 Ceramic solid-state ionic conductors

2.5.1 Mechanism of ion transport in SSE

In classical approximation of ion transport, the ionic motion is defined as the movement of ions through vacancies and interstitial sites of a crystalline compound material. This model is known as ion hopping model as shown in Figure 2.5. The concentration of defects and vacancies are considered uniform throughout the crystal structure. So, the high ionic conductivity in ceramic electrolytes is possible when there is high concentration of mobile species and low energy barrier associated with ion motion from one site to another. Thus, in presence of electric field, the Li ions would hop randomly through the ceramic crystal structure and still migrate towards the direction of electric field, which defines the basic Li ion conduction mechanism in crystalline solids. In hopping model, the Li ion (Li^+) conduction is considered as its jumping process through the crystal lattice. The hopping of ions from one site to its vicinity site is based upon two

52

factors: (1) jumping frequency, which is the probability of Li$^+$ jumping to an adjacent site in a given direction at a unit time, and (b) defects concentration $\times$ nearest neighbor site number, defined as probability of availability of neighboring sites for ion conduction from a given site.
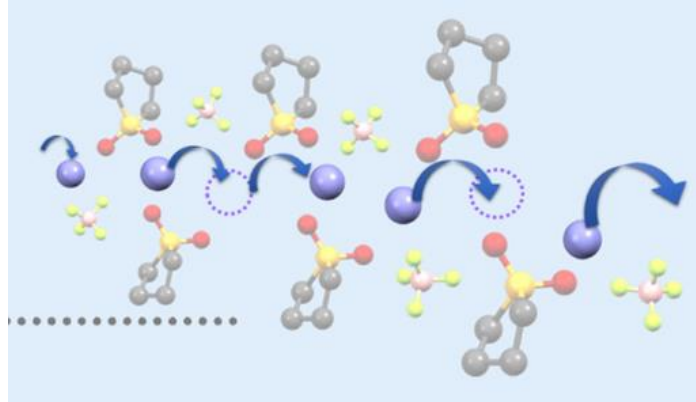
Figure 2. 5 Schematic showing hopping model for ion conduction [229].

2.5.2 Garnet crystalline structure

The general formula for garnet type solid crystalline ceramics is given by $A_3B_2X_3O_{12}$, where site A are 8-fold, B are 6-fold, and X are 4-fold coordinated. The first reported garnet type LLZO SSE with Li ion conductivity of 10^{-3} to 10^{-4} S cm^{-1} was by Murugan et al [156]. The reported LLZO structure, $Li_7La_3Zr_2O_{12}$ had Li higher than 3 per formula unit and so were called Li-stuffed garnets. As shown in Figure 2.6 (a), the LLZO structure is formed by connecting ZrO_6 octahedra, and LaO_8 dodecahedra. In this structure, the Li ions (Li$^+$) and Li vacancies (V_{Li}) are located at the invasive tetrahedral sites and octahedral sites. As one of the Li$^+$ is located at tetrahedral 24 d position, and another at octahedral 96 h position, the conduction pathway for Li$^+$ in LLZO structure is 24 d $\rightarrow$ 96 h $\rightarrow$ 24 d (Figure 2.6 (c,d)) [230]. The lattice disorder and presence of vacancies ensures the conduction of Li$^+$ through this pathway.

(a)

La

Zr

O

b
c a

Li2   Li1

1.602(18) Å

(b)

b

Li(1)O₄

Li(2)O₆

Li(3)O₆

(c)

Li2 site
(g = 0.35)

Li1 site
(g = 0.94)

(d)

Unit cell

b
c a

Li2 site

Li1 site

Li-ion migration
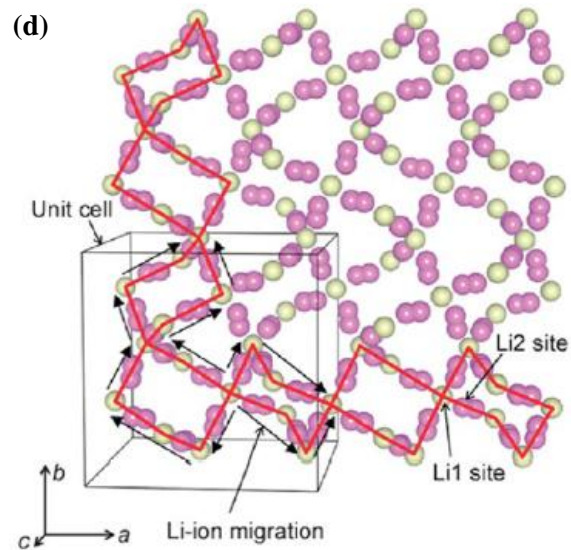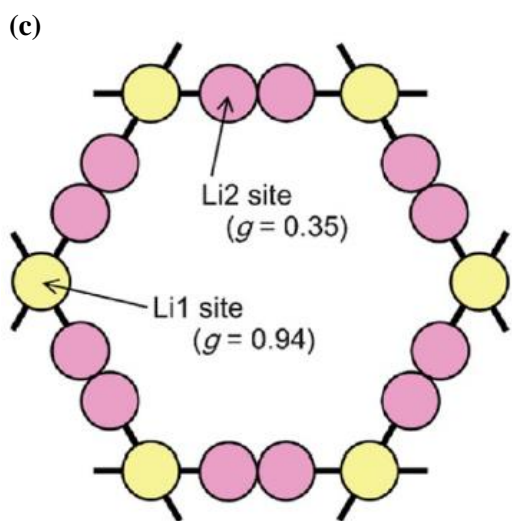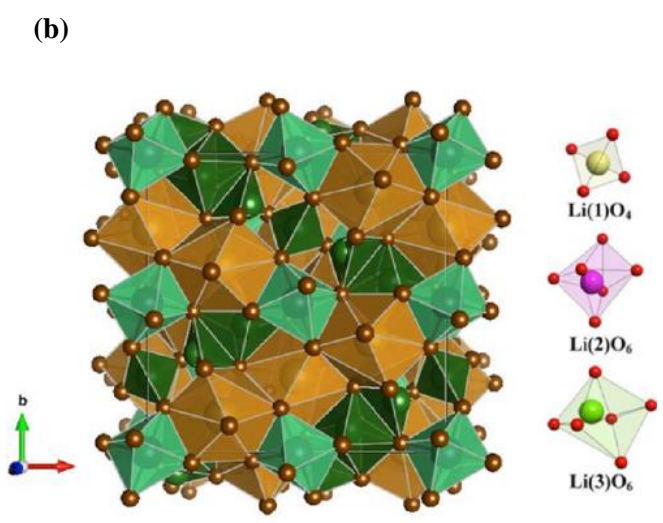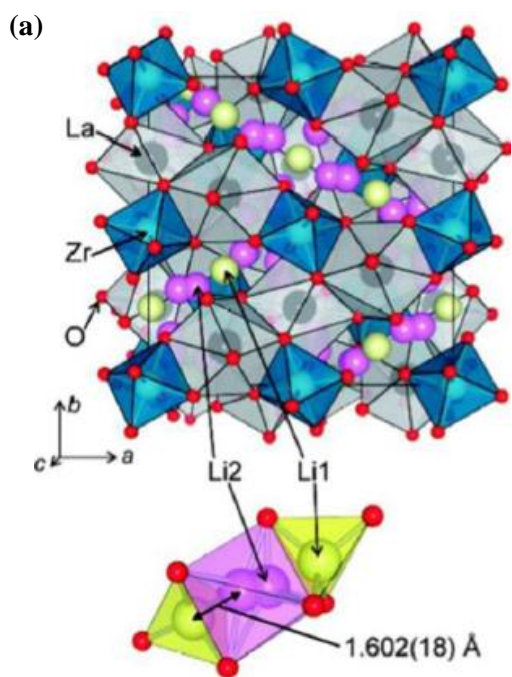
Figure 2. 6 (a) crystal structure of LLZO, (b) crystal structure of tetragonal LLZO, (c) arrangement of Li atoms with their occupancy value, *g*, for each site in loop structure, and (d) 3D network structure showing Li$^+$ conduction channel (Li1- 24 d, Li2- 96 h) [231, 232].

The crystalline phase of LLZO exists in two polymorphs: (1) cubic phase (*c*-LLZO), and (2) tetragonal phase (*t*-LLZO). Figure 2.6 (b) shows the tetragonal phase of LLZO with its lattice structure. Between these two phases, the *c*-LLZO has two orders higher ionic conductivity (~10^{-4} S cm^{-1}) than *t*-LLZO (~10^{-6} S cm^{-1}) at RT. This is due to the fact that in *c*-LLZO there is a uniform movement of Li$^+$ in *x,y*, and *z* directions, whereas in *t*-LLZO, Li$^+$ only moves in *x* and *y* directions [233]. Similarly, Li$^+$ distributions are also different in these two phases. In cubic phase the Li sublattice is highly disordered with presence of partially occupied Li symmetry sites, whereas in tetragonal phase the sublattice is ordered with either full or empty Li occupancy sites. This results in lower electrostatic energy for *t*-LLZO than *c*-LLZO as for *t*-LLZO the coulombic repulsion among Li$^+$ will be highly reduced [234]. This is the reason why *t*-LLZO can be thermodynamically stable at RT, whereas *c*-LLZO are only stable at high temperatures, usually > 1200 °C.

Different strategies such as optimizing sintering time and temperature, using different types of crucibles, elemental doping, use of additives, and altering the sintering atmosphere have been developed by the researchers to stabilize the cubic phase LLZO at RT. Elemental doping have shown to effectively stabilize the cubic phase at RT. Doping of ions at different sites such as Ta^{5+} and Nb^{5+} at Zr^{4+} sites, or Al^{3+} and Ga^{3+} at Li$^+$ sites, will change the number of V_{Li}, thus creating more disorder at the Li and V_{Li} sites. As the disorder increases the entropy of doped *c*-LLZO also increases at RT leading to decrease in its Gibbs free energy, which results in

stabilization of doped *c*-LLZO at RT [189, 235-243]. In addition, the doping of garnet LLZO have also been shown to increase its ionic conductivity. Using density function theory (DFT) first-principle calculations, the doping sites and oxidation states preferred by each dopants in periodic table have been identified and shown in Figure 2.7 [244].
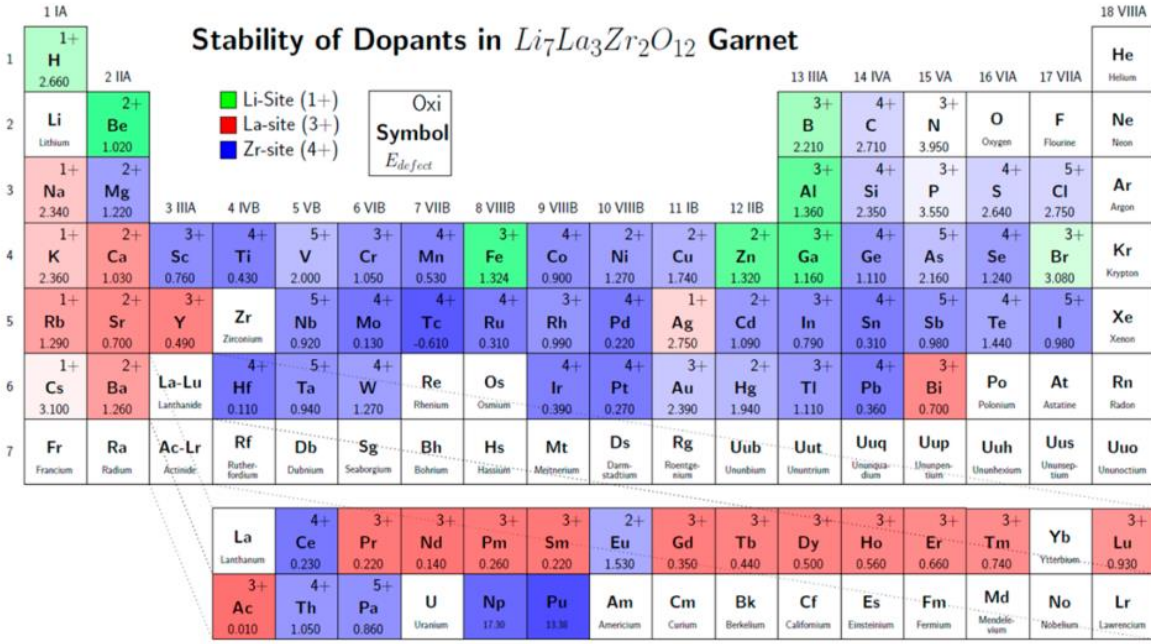
Figure 2. 7 Periodic table showing doping site and oxidation state preference of dopants in LLZO structure from DFT calculations. Different color shows different doping site (green: Li site, red: La site, and blue: Zr site), where defect energy decreases with increasing color darkness [244].

Besides the effect of doping, the sintering process and temperature also plays a vital role in Li^+ vacancies concentration. As the temperature increases, more Li^+ volatilize in the LLZO structure

inducing more Li$^+$ vacancies. The total ionic conductivity of a LLZO sample is calculated by using equation (2.14).

$$\sigma = \frac{l}{RS}$$
(2.14)

where R is the resistance, l is the sample thickness, and S is the electrode area. Similarly, the increase in temperature shows decrease in resistance (R) from the Nyquist plot which leads to increase in ionic conductivity of garnet LLZO. This relationship is expressed by the Arrhenius equation (2.15).

$$\sigma = A \exp\left(\frac{-E_a}{K_b T}\right)$$
(2.15)

where σ is the ionic conductivity, A is the pre-exponential factor, T is the absolute temperature, E_a is the activation energy, and K_b is the Boltzmann constant. The activation energy (E_a) is calculated as the slope of *log σ* v/s *1000/T* plot, shown in Figure 2.8.
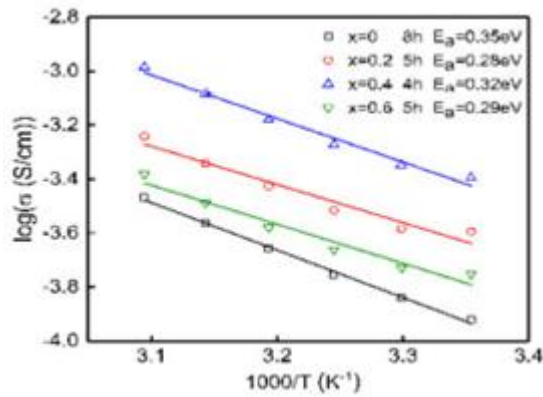
Figure 2. 8 Arrhenius plots showing temperature dependance of ionic conductivity for different dopant concentration (x), at different sintering duration (h). Solid symbols show experimental data and lines are the fitted curves according to Arrhenius equation. Activation energy (E_a) is calculated as slopes of respective fitted lines [245].

2.6 Electrode/electrolyte interface in SSBs

The major hurdle of solid-state LMBs is the high interfacial charge transfer resistance (R_{ct}) resulting from various issues at the electrode/electrolyte interface. This will lead to low power density, poor cyclability, and rapid capacity fade of SSBs [246]. It has been shown that EIS is one of the powerful characterization tools to analyze the resistance at the electrode/electrolyte interface of SSBs [247-249]. Among different bulk and surface layer resistances, the interfacial resistance accounts for about 60 % of the total resistance. Thus, it is necessary to solve the problem of high interfacial resistance in order to realize high energy density SSBs. The key reasons for poor electrode/electrolyte interfaces in SSBs can be broken down to: (1) minimum contact area, (2) formation of co-diffusion layer due to side reactions, (3) blocking of ion transport due to space charge layer, and (iv) stress at the interface caused by electrode volume change.

2.6.1 Electrode/electrolyte contact area

Formation of intimate contact at the electrode/electrolyte interface is highly favorable for obtaining efficient charge transfer at the interface. The main issue with for e.g., LMA/ garnet SSE interface is their poor wetting at the interface leading to less contact area and high area-specific resistance (ASR). Thus, to increase the contact area of LMA/garnet SSE interface the wetting behavior of garnet surface towards LMA should be improved, in other words, garnet surface should be lithiophilic. Different techniques such as surface polishing, Li alloy forming coatings on garnet, and advanced thin-film deposition of garnet on Li surface can enhance their contact area and lower the ASR at the interface.

2.6.2 Co-diffusion at the interface

The interaction between electrode and SSE when they come in contact results in formation of diffusion layer at the interface. For e.g. when the interface of $LiCoO_2$ with Li_2S-P_2S_5 was analyzed using transmission electron microscopy (TEM), co-diffusions of Co, P, and S was observed at the interface [248]. The formation of these diffusion layer can result in increase of interfacial resistance if it hinders the transfer of ions and worsens the electrode/electrolyte contact area. To overcome this issue scientists have investigated coating of different buffer layers that forms favorable diffusion products at the interface. Similarly, the insulating diffusion layer at the interface can also be formed by decomposition of SSE or electrode materials. Therefore, chemically stable electrode and SSE materials within themselves or when in contact should be employed.

2.6.3 Formation of space charge layer

Considering the ionic conductivity in SSEs the rate determining factor is the ion conduction at the electrolyte/electrolyte interface rather than the bulk [250-252]. The transport of ions at the interface is very different than that at the bulk. This phenomena of difference in ionic conduction of bulk compared to the interface is attributed to formation of space charge layer at the interface with different mobile ion concentration (Figure 2.9). Although the thickness of these space charge layers are generally only around 10 nm, the ion conduction in them are in nanoscale which will trigger significant difference in Li ion concentration compared to bulk [253]. This variation in Li ion concentration at the interface is more pronounced during initial stages of charge/discharge cycles as shown in Figure 2.9 (a, c). The evidence of this variation or existence of space charge layer was also verified by increased potential slope of voltage profile at initial charge/discharge stage [254].

59
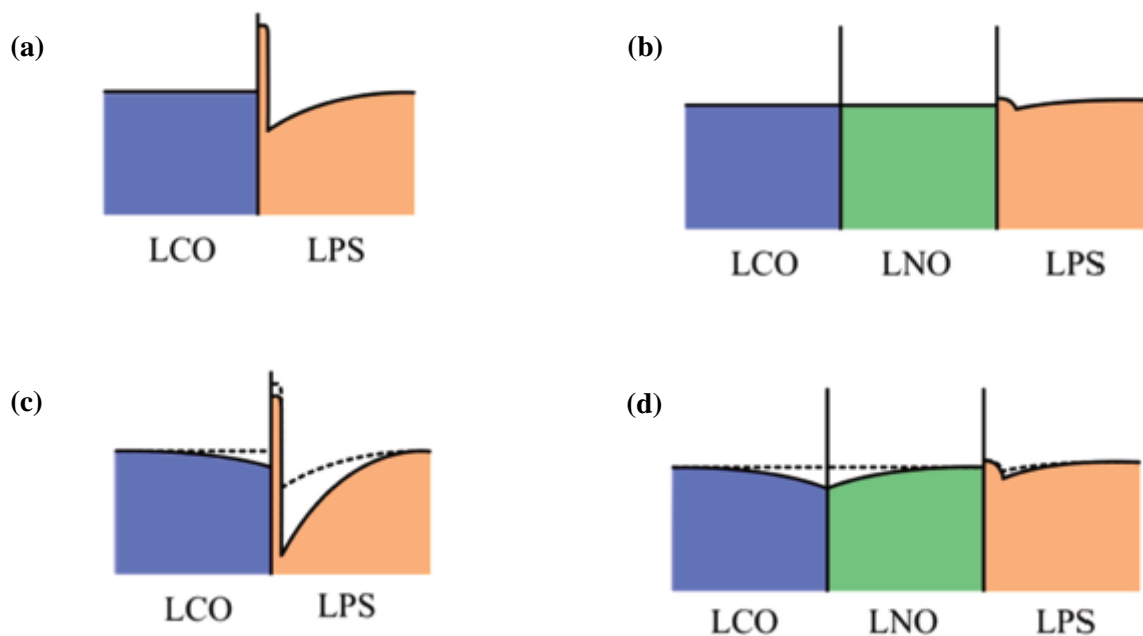
Figure 2. 9 Schematics showing effect of interfacial buffer layers to the Li ion concentration at the electrode/electrolyte interface. Li concentrations at equilibrium for (a) without, (b) with buffer layer, and at initial stage of charging (c) without and (d) with buffer layer [254].

Further, it was verified that the introduction of buffer layer with high ionic conductivity and electronic insulator can be effective to protect the electrolyte from high potential (oxidation/reduction) electrodes. By coating of this layer at electrolyte surface the formation of space charge layer was suppressed and more homogeneous Li ion concentration at the electrode/electrolyte interface was obtained (Figure 2.9 (b, d)).

2.6.4 Stress by electrode volume change

As lithiation and delithiation of electrodes occur repeatedly during battery cycling, its surface experiences significant volume change. The lattice expansion and contraction of electrode materials induces high stress at the electrode/electrolyte interface which can result in local

distortion and formation of cracks leading to high charge transfer resistance. Use of electrode nanomaterials can relieve the stress from volume change during cycling [255, 256]. Similarly, using amorphous buffer layers with high ionic conductivity at the interface can effectively compensate the interface distortion and subsequent increase in interfacial resistance due to electrode volume change [257].

2.7 Material characterization techniques

2.7.1 X-ray diffraction (XRD)

X-rays are the part of electromagnetic spectrum, which have wavelength shorter than ultraviolet light. Different part of X-ray spectrum is used for different applications such as soft or hard X-rays for X-ray crystallography, mammography, medical CT scan, and airport security scan, etc. XRD is an X-ray crystallography technique that is used to determine the atomic and molecular structure of the crystal and in which the atoms of a crystalline solid causes beam of incident X-rays to diffract into many specific directions. In an XRD experiment, to generate X-rays usually an electrically heated tungsten filament emit electron. These emitted electrons are accelerated under high potential difference (20 to 50 kV) and then incident on a water cooled anode which generates continuous spectrum of white X-ray radiation. The generated X-rays are radiated onto a solid crystal sample whose structure is of interest. In most crystalline solids, there are parallel rows of atoms separated by a unique distance, typically these interatomic spaces are of approximately 2-3 Å. So, X-rays are suitable radiation to study these crystal structures as they get diffracted when incident on these atomic spaces. In XRD, reflection of X-rays only occurs when the condition of constructive interference is fulfilled. This is defined as Bragg's condition for X-ray reflection and shown in Figure 2.10. The array of black dots in the figure shows the

61

sectioned crystal lines, joining each dot marks are set of parallel planes with Miller indices *hkl* and d_{hkl} represents the interplanar spacing.
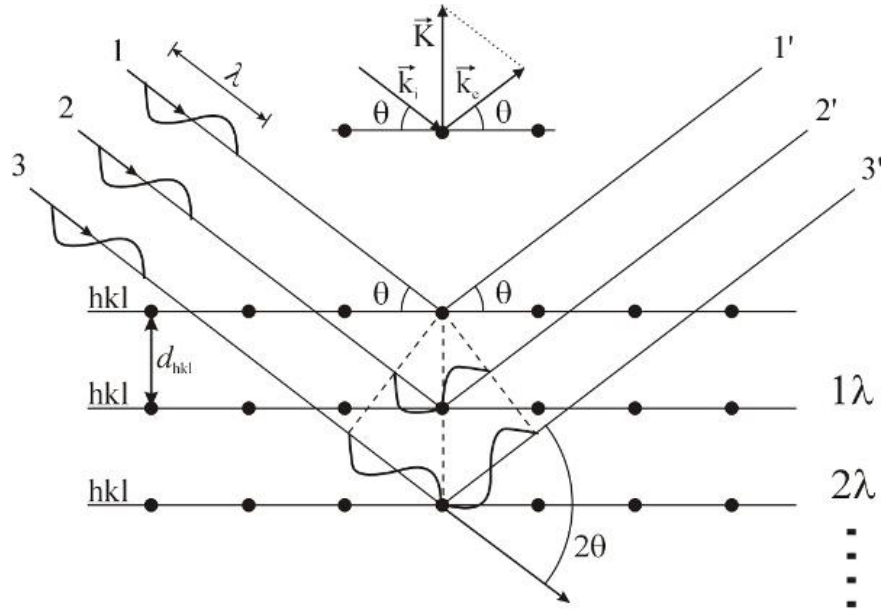
Figure 2. 10 Example of constructive interference showing Bragg's reflection from crystal planes with d_{hkl} spacings [215].

The relation of spacing between the crystal planes (*d*) and the angles from which these reflections are observed, Bragg's angle (*θ*) is given by the Bragg's equation (2.16).

$$n\lambda = 2d \ sin\theta \qquad (2.16)$$

where *2d sinθ* gives the path difference between scattered and incident rays, *n* is an integer, and *λ* is the wavelength of incident X-ray.

2.7.2 X-ray photoelectron spectroscopy (XPS)

XPS is a spectroscopic technique used to quantify the elements, their concentrations, and chemical state at the samples surface. In this characterization technique, the samples are bombarded with monochromatic beam of soft X-rays (1-3 keV) which causes photoemission,

release of photoelectrons from core or valence levels of surface atoms. This phenomenon is governed by the Einstein's photoelectric principle (equation (2.17)) , which states that if a solid sample is subjected to X-rays with energy hv, electrons in the orbitals of sample with binding energies less than hv can be ejected and subsequently detected in a spectrometer by measuring its kinetic energy (KE_i) and number of electrons that are emitted.

$$KE_i = hv - BE_i - \phi_{sp} \qquad (2.17)$$

where BE_i gives the binding energy of an electron in orbital i, and ϕ_{sp} is the correction work function of the spectrometer ($\sim 3 \pm 5$ eV).

Thus, XPS is an important tool to analyze the change in chemical state of battery materials or surface layers before and after charge/discharge cycles. It can also provide the information about change in the chemical bonding of some element in a surface layer such as SEI by shift in the core electron's binding energy. Further, the information on effect of electrolyte additives in SEI composition, components of *in-situ* formed SEI, and overall understanding of SEI formation can be revealed using XPS characterization.

2.7.3 Field emission SEM (FESEM)

The FESEM is an imaging technique in which high energy monochromatic electrons that are generated by a field emission source at potential of 1-30 kV, accelerated through a high electric field gradient, and focused into a fine beam using lenses are rastered across the sample. When these electrons interact with the sample inside high vacuum different signals are obtained such as: (1) back-scattered electrons (reflected electrons by elastic scattering), (2) emitted secondary electrons (from inelastic scattering), and (3) characteristic X-rays (from production of secondary electrons). The SEM images are formed mainly due to signals detected from secondary electrons.

The emitted secondary electrons after interaction with samples are accelerated towards the scintillation detector, amplified through photomultiplier, and finally displayed as a video scan-image where the brightness of image depends on the number of electrons detected. SEM images can produce maps of surface topography of samples such as polymers, ceramics, metals, etc. in a micro to nano scale. It is also applicable for analyzing the particle size, crystal morphology, and surface defects in a sample. The samples or at least the sample surface that are being analyzed using SEM must be electron conductive. The non-conducting samples are generally coated with gold (Au), to prevent charge build up at the sample surface.

2.7.4 Energy dispersive spectroscopy (EDS)

EDS or sometimes known as EDX is an elemental analysis tool usually used in junction with SEM or FESEM. The back-scattered electrons obtained during SEM analysis have higher energy, which are collected and when higher atomic number elements back-scatter even stronger electrons the quantitative elemental analysis of the surface is obtained. Similarly, during production of secondary electrons inelastic scattering occurs, in which electron vacancies are created and filled by electrons from higher state. This causes emission of characteristic X-rays to create energy balance between emitted and incident electrons. These X-rays carries the qualitative properties of the elements in sample surface. Therefore, EDS analysis can provide the information about elements present in the sample as well as their atomic % or weight %. Different elements present in the sample can be mapped in the sample area using different colors.

2.7.5 Atomic force microscopy (AFM)

AFM is microscopy imaging technique based on detection of very small forces, in an order of nanonewtons observed by the interaction between a nanometer scale sharp tip and atoms in the surface of the sample. Non-conducting samples can be easily analyzed without any

modifications, and in ambient conditions without use of vacuum in this technique. In this process, the tip is scanned across the sample surface, and its deflection due to attractive or repulsive forces when interacting with the surface are detected and mapped in atomic scale. This technique can be used to determine the forces acting on the sample surface, such as van der Waals, magnetic, capillary, chemical bonding, friction, etc. Various modes such as contact, non-contact, and tapping mode can be applied in the experiment depending upon the sample used. The AFM images can give the information about surface roughness, topography, and strength (Young's modulus). Similarly, using AFM a 3D map of the surface can also be generated.

2.7.6 Raman spectroscopy

Raman spectroscopy is non-destructive characterization technique used to observe vibrational, rotational, and other low frequency modes in an atomic or molecular system. It mainly uses a monochromatic laser light (300 to 1064 nm) in either visible, near infrared, or ultraviolet range. In this process, the monochromatic beam of laser light interacts with molecular vibrations, phonons or other excitations within the system that results in energy shift of incident laser photons, either up or down. Various information such as chemical structure, polymorphs, crystallinity, molecular interaction, and crystal phases of a system can be obtained using Raman spectroscopy. It can be considered as a light scattering tool, where incident laser light are scattered by the atoms or molecules in the sample. The wavelength of these scattered beams also known as Raman or inelastic scatter are recorded which provides the detailed information of the sample material. Although X-rays can also be used, Raman can detect different materials with same crystalline structure (e.g., Raman peaks for diamond, crystalline silicon, and crystalline germanium, all with diamond cubic structure are at different wavenumber) or materials made with same elements but showing different crystallinity (e.g., crystalline, polycrystalline,

65

amorphous silicon). Microscopic materials with spatial resolution of 0.5-1 µm can be detected using Raman spectroscopy. Different sample types such as solid, powder, gel, slurry, gas, etc. can be used for Raman analysis.

2.8 Electrochemical characterization techniques

2.8.1 Electrochemical impedance spectroscopy (EIS)

EIS is a vital electrochemical characterization tool which gives information about electrochemical reactions and charge transfer dynamics in different layers of an energy storage device. Typically, in an EIS experiment, small sinusoidal perturbations voltage (*E(t)*) is applied to an electrochemical system. The resulting linear current density (*J(t)*) is recorded whose frequency is equal to that of *E(t)*, but their phase and amplitude maybe different. Then, their ratio is taken to calculate the impedance (*Z(t)*) as shown in equation (2.18).

$$Z(t) = \frac{E(t)}{J(t)} \qquad\qquad (2.18)$$

For this experiment the input is a time dependent voltage, so it is known as potentiostatic EIS (PEIS). Whereas experiments with altering current as input is known as galvanostatic EIS (GEIS). In both PEIS and GEIS experiments the frequency is varied to observe the electrochemical phenomenon occurring at different timescales. For e.g., at high frequencies fast process such as ion migration are observed, whereas slow processes such as diffusion are realized at low frequency regions of the spectrum.

EIS experiments are generally used to analyze bulk electrolyte/electrode properties, test interfacial reactions, and examine full cell device behavior. As shown in Figure (2.11 (a)), Nyquist plots, fitted using equivalent circuit model (ECM), are used to interpret EIS results, where Z real axis corresponds to values of different resistances within the system. Each

component of Nyquist plot can be represented by either resistive, capacitive, or diffusive

elements. The point where the EIS starts gives the ohmic or series resistance (R_b), which is also

the bulk resistance. Similarly, the semicircle in higher frequency range gives the SEI impedance

(R_{SEI}) and that at the lower one gives the charge transfer resistance (R_{ct}), the constant phase

element (CPE) represents the electric double layer capacitance between the interfaces. However,

some alterations are possible when testing different electrochemical systems, for e.g., SEI

impedance in LIBs maybe represented as solid-solid interphase in SSBs. Figure 2.11 (b) shows

the Nyquist plot obtained by fitting generic ECM for SSBs with LMA which consists of bulk

resistance ($R_{SE, bulk}$), grain boundary resistance (R_{HF} or R_{gb}), electrodes interfacial layers (R_{MF} and

R_{LF}) [258, 259]. Also, the inclined line at the end of the lower frequency region shows Warburg

impedance (W), that represents charge diffusion.
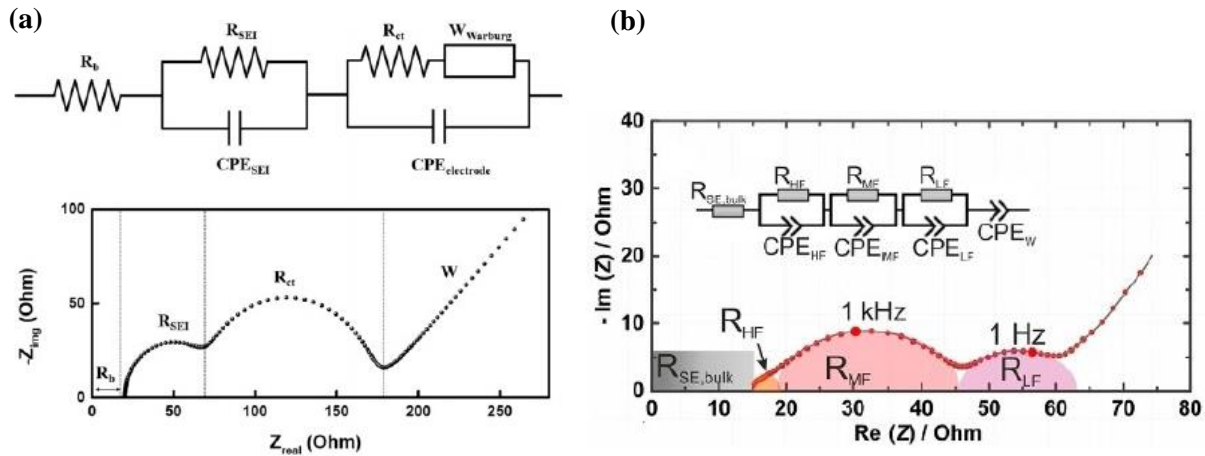
Figure 2. 11 Nyquist plot obtained by fitting parameters using ECM for typical (a) LIBs

[260], and (b) SSBs [259].

2.8.2 Linear sweep and cyclic voltammetry (LSV and CV)

LSV and CV are both widely used voltametric techniques to study the redox reactions involving organic or inorganic species. These electroanalytical processes, provides information on electrochemical redox processes, chemical reaction rates, electrochemical stability window, charge transfer processes, etc. In LSV experiment, a potential range (V_1-V_2) is defined, and the voltage is scanned form the lower to upper limit of that range. As the voltage increases, current begins to flow and eventually reaches a peak before it drops, which shows the chemical reactivity of electroactive species (Figure 2.12 (a)). The rate of electron transfer reaction can also be obtained from the LSV by observing the position of current maximum shifts.
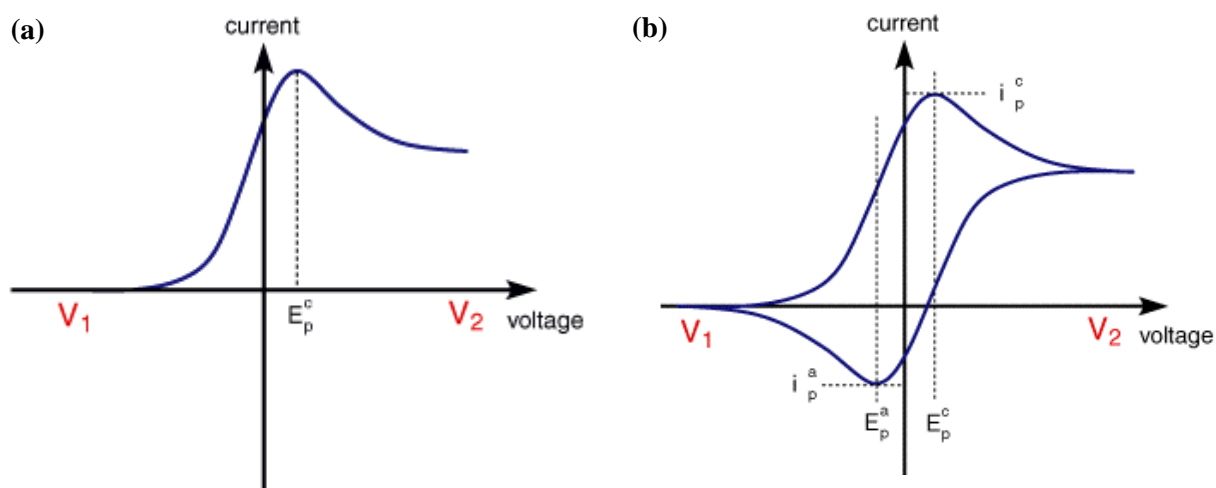
Figure 2. 12 Typical voltammetry curves for (a) LSV, and (b) CV [215].

Similarly, in case of CV as well the voltage is swept between a voltage range (V1-V2) at fixed rate, but now when voltage reaches V_2 the scan is reversed, and it is swept back to V_1, and the current response is observed (Figure 2.12 (b)). During reverse scan the chemical reaction is moved back to its equilibrium state gradually converting products to its reactants. So, the CV test

also shows the reversibility of a chemical reaction. Both of these techniques can be used in case of electrochemical cells, where the potential between the working electrode and the counter electrode is increased linearly by the means of potentiostat. The multiple recordings of current response according to change in voltage between the working and counter electrode are plotted.

2.8.3 Symmetrical cell test

Symmetrical cells are the electrochemical cell design in which same electrode material is used as both positive and negative electrode (so the name symmetrical). Typically, for LMBs research symmetrical cells with Li as both electrodes are tested to analyze their electrochemical plating/stripping behavior. The Li symmetrical cells show 0 V v/s Li/Li^+, so they cannot be used as practical batteries. However, symmetrical cell test can provide the comparison between modified Li electrode (e.g., electrolyte additive used, ASEI or interfacial layer coated, etc.) samples and bare or control Li electrode samples regarding the metrices such as critical current density, voltage stability, cycling longevity, overpotential loss, and achievable capacity.

2.8.4 Full cell test

Full cells are electrochemical cells which consists of different electropositive and electronegative electrodes. Thus, exhibiting voltage difference v/s Li/Li^+, so they can be considered for practical application. In case of LMBs, the full cells are assembled with Li metal as electronegative (anode) electrode and cathode materials such as lithium iron phosphate (LFP), lithium nickel manganese cobalt oxide (NMC), lithium cobalt oxide (LCO), etc. as electropositive (cathode) electrode. The full cells testing are performed in order to validate various enhancement strategies by comparing the parameters such as specific capacity, capacity retention, rate capability, cycling stability, high voltage stability etc. between control/baseline and modified/improved full cells.

Chapter 3: Experimental Procedures

3.1 Materials and sample preparations

3.1.1 Nitrate salt as electrolyte additive

3.1.1.1 Ether based electrolyte

For preparing baseline electrolyte, 1 M of lithium bis(trifluoromethanesulfonyl)imide (LiTFSI, Sigma Aldrich, 99.95 % purity) salt and 1 wt % lithium nitrate (LiNO$_3$, Sigma Aldrich, 99.99 % purity) were dissolved in ether solvent mixture (1:1 by volume) of 1,3-dioxolane (DOL, Sigma Aldrich, 99.8 % purity) and 1,2-dimethoxyethane (DME, Sigma Aldrich, 99.5 % purity). This solution was used as control electrolyte with no addition of additive. Then, the experimental electrolyte with additive was prepared by adding different concentrations of gadolinium (III) nitrate (Gd(NO$_3$)$_3$) onto the control electrolyte solution and stirring it under argon (Ar) atmosphere. The Gd(NO$_3$)$_3$ nitrate salt used as additive was prepared prior to adding onto control electrolyte solution by careful heating of Gd(NO$_3$)$_3$.6H$_2$O (Sigma Aldrich, 99.99 % purity) at around 120 °C under vacuum to remove the water. Finally, the as prepared solution was used to assemble samples with electrolyte additive.

3.1.1.2 Cathode and anode

LFP cathode electrodes were prepared first by mixing LFP (LiFePO$_4$, Xiamen Tmax, China, particle size 0.55 µm) as active material, Super P conductive carbon black (Alfa Aesar, 99 % purity) as conductive additive, and polyvinylidene fluoride (PVDF, Sigma Aldrich, M$_w$ ~ 534,000) as binder (8 : 1 : 1 weight ratio) in N-methyl-2-pyrrolidone (NMP, Sigma Aldrich, 99.5 % purity) solvent. The mixture was first well mixed in mortar and pestle and left to stir using magnetic stirrer for ~ 12 h. Then, the slurry was obtained, and it was made sure no lumps and accumulations were present in it. The as prepared slurry was coated onto an aluminum (Al) foil

(Xiamen Tmax, China, 0.0016 mm thick) current collector using mini tape casting coater (MTI Corp.) and then dried in a vacuum oven at 120 °C overnight to ensure solvent evaporation. The dried cathode strips with active material mass loading of ~ 4 mg cm^{-2} were cut into circular discs of 12 mm diameter by using disc cutter. Also, similar process was followed for preparing NMC 111 (LiNi$_{1/3}$Co$_{1/3}$Mn$_{1/3}$O$_2$) cathode electrodes which were used for testing high voltage stability of electrolytes.

For preparing LMAs, Li chips (diameter 15.6 mm and thickness 0.25 mm) were purchased from Xiamen Tmax, China. Before using them as anodes their surface were polished by 1500 grit sized sandpapers using a rotary tool set (Fire Mountain Gems and Beads, USA) inside Ar glovebox with moisture and O$_2$ level < 1 ppm. After ensuring uniform polish, these Li chips were immediately used to assemble coin-cell samples.

3.1.1.3 Symmetrical and full cell

For both symmetrical and full cells, CR2032 coin cell batteries were assembled. For symmetrical cell assembly, polished Li metal chips were stacked with 25 µm thick celgard type separator (Xiamen Tmax, China) sandwiched in their middle. About 60 µL of ether based electrolyte with and without Gd(NO$_3$)$_3$ additive were used as electrolyte to prepare additive added and control Li symmetrical cells, respectively. Similarly, to assemble full cells either LFP or NMC 111 as cathode material and polished Li chips were used as anode materials. Both symmetrical and full coin cells were crimped using manual hydraulic coin cell crimping machine (Xiamen Tmax, China).

3.1.2 Metal nitride lithiophilic SSE interlayer

3.1.2.1 Garnet Al-LLZO SSE pellet

For preparing garnet Al-LLZO pellets, firstly, 0.4 gm of cubic phase aluminum doped lithium lanthanum zirconate garnet nanopowder, $Li_{6.25}Al_{0.25}La_3Zr_2O_{12}$ (Ampcera Inc., 99.9 % purity) were pressed in a ½ inch diameter stainless steel pellet pressing die (MTI Corp.). The pressing die with Al-LLZO nanopowder in it was placed between two platens of the hydraulic laboratory press (Carver Inc.) and 80 MPa pressure was applied to press the powder into pellets. After that the pellets were laid on a magnesium oxide (MgO) crucible, the pellets surface were covered with same Al-LLZO mother powder both from top and bottom. The crucible was carefully placed in the furnace (Mellen, Microtherm) and sintered at different temperatures which was optimized to 1280 °C for 1 h. The sintered pellets were left to cool down to room temperature and were dry polished from 1000, 1500, 2000 to 3000 grit sized sandpapers using rotary tool set (Fire Mountain Gems and Beads, USA). Lastly, the polished pellets were stored in Ar glovebox for future use in assembling SSBs.

3.1.2.2 Metal nitride interlayer deposition

3400 N Torr IBAD system (Hitachi, Japan) was used to RF sputter deposit thin films of silicon nitride (Si_3N_4) onto the polished Al-LLZO SSE pellets. The polished pellet samples were carefully secured by using Kapton tape in a ceramic plate before attaching it to the sample stage inside the vacuum chamber. A 2-inch diameter $\times$ 0.125 inch thick, 99.9 % metals basis, silicon (IV) nitride (Si_3N_4) with MgO binder (Alfa Aesar) was used as target and screwed on the target gun for RF sputtering deposition. The sputtering deposition process was then carried out at deposition rate of 0.1 Å s^{-1} with 50 sccm constant flow of Ar gas. Using this system various

thicknesses (e.g. 20, 30, 40 nm etc.) of Si_3N_4 layer were deposited, and the thickness was later optimized to 30 nm.

3.1.2.3 Cathode and anode

LFP active materials were used to fabricate cathode films, and similar process as described in section 3.1.1.2 was used to obtain cathode films. However, for this process the dried cathode strips were punched into circular disks of 9 mm diameter with active material mass loading of ~2 mg cm^{-2}. Also, in this process LMAs were melt infused onto the Al-LLZO SSE pellets. So, in order to prepare the anodes, granular Li (Sigma Aldrich, 99 % purity) were melted around 200 °C and dip coated on the SSE pellets inside Ar glovebox. The top dull layer of melted Li was meticulously scrapped off exposing shining layer underneath before the coating process.

3.1.2.4 Solid-state symmetrical and full cell

For this process also, CR2032 Li symmetrical and full coin cells were assembled. The solid-state Li symmetrical cells were prepared by attaching melted Li at 200 °C on both sides of electrolyte pellets. After cooling down, symmetrical cell samples for both Si_3N_4 coated and bare garnet pellets were prepared in Ar glovebox for analyzing and comparing their ionic conductivity and cycling stability. Similarly, hybrid solid-state full cells were assembled by introducing tiny amount, 10 µL of LE (1 mol L^{-1} $LiPF_6$ dissolved in ethylene carbonate (EC) and diethyl carbonate (DEC) in volume ratio 1:1) between LFP cathode and SSE pellet to enhance the cathode/electrolyte interface contact. However, no trace of LE was applied on the other side, and melted Li was soldered on the top of it. Both Si_3N_4 coated and bare garnet full cell samples were prepared by sealing the assembled full cells in a CR2032 coin cell casings with nickel foam on the top for absorbing any extra pressure during crimping, in order to avoid damage to the SSE pellet.

3.2 Material characterizations

3.2.1 XRD

The crystal structure and crystalline phase of the samples were examined using XRD. The tests were performed on a Rigaku SmartLab diffractometer (Figure 3.1) with Cu-Kα radiation (λ = 1.54178 Å). For performing XRD analysis of air sensitive samples such as Li metal surface, Li infused garnet, etc. the samples were encapsulated using Kapton tape and placed in the XRD sample holder. The test parameters and 2-theta degree scanning rage were selected according to types of samples. After obtaining the XRD data, they were compared with other different references from the database. The indexing of obtained XRD diffraction peaks with standard pattern was performed to compare the resemblance and recognize the sample peaks, and any impurities if present.

Figure 3. 1 Rigaku SmartLab diffractometer equipment used for XRD analysis

3.2.2 XPS

The XPS analysis of samples were performed in scanning XPS microprobe, the VersaProbe 4 (Figure 3.2 (a)) instrument from Physical Electronics, Minnesota. Both Li symmetrical and full cell samples were kept in inert Ar atmosphere upon arrival. The LMA samples from disassembled cells were affixed into the sample holder using nonconductive double-sided adhesive tape (Figure 3.2 (c)). This sample holder was then transferred to the VersaProbe 4 instrument inside inert environment through a transfer vessel. The transfer vessel was mounted on a load-lock (Figure 3.2 (b)) which was pumped down to $\sim 2 \times 10^{-6}$ Torr before moving it to the XPS analysis chamber. The sensitivity factors for different elements analyzed by using this equipment were noted along with the XPS data. Further, the X-ray induced secondary electron imaging (SXI) was also performed over wide sample area, which was used to identify the important morphological features of the battery component samples (Figure 3.2 (d)).

(a)

(b)

(c)

(d)
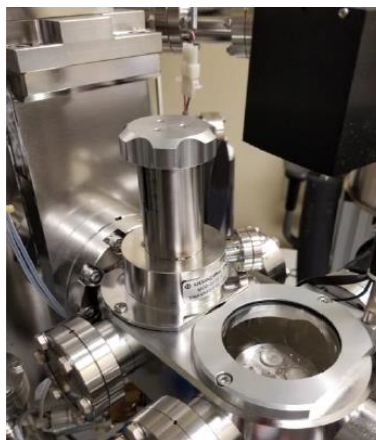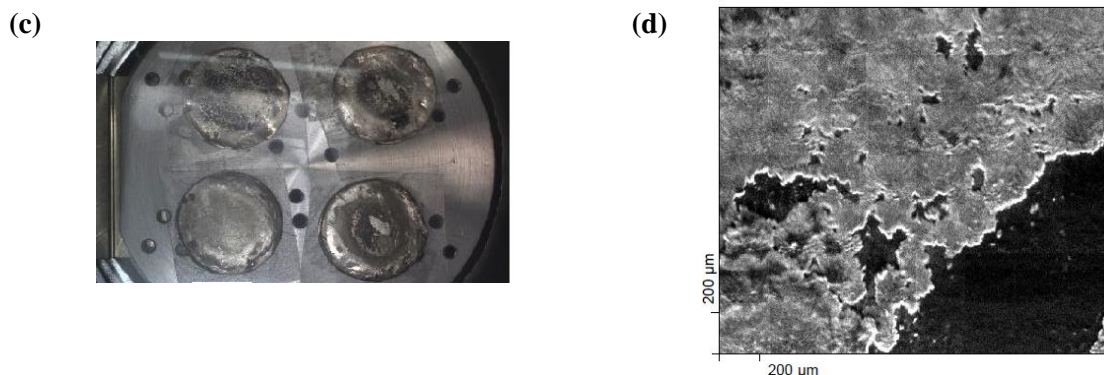
Figure 3. 2 (a) VersaProbe 4 equipment at Physical Electronics, MN, Digital images of (b) 60 mm transfer vessel mounted on the load-lock system, (c) LMA samples attached on the sample holder and loaded in the transfer vessel, and (d) SXI imaging on the surface of LMA.

3.2.3 FESEM/ EDS

To observe the LMA surface morphology and cross-section interface characteristics, SEM imaging of samples were performed using Hitachi S-4300 N (Figure 3.3) scanning electron microscope, which was also equipped with EDS, for performing elemental mapping characterizations. The EDS equipment from Oxford Instruments was used to record the EDS spectrum and elemental mapping images. The air and moisture sensitive samples were encapsulated in closed vial and instantly transferred to the SEM sample holder. Different accelerating voltage and rigorous focusing was performed on the sample surface to obtain good quality images. While examining semiconducting and non-conducting samples, a thin layer of Au was sputtered using CRC-sputtering deposition system in order to avoid charge build up during imaging. Images at different areas and with various scales were taken and saved using the SEM and EDS software.

Figure 3. 3 Hitachi S-4300 N equipment used for SEM imaging

3.2.4 AFM

The surface topography, roughness, and Young's modulus of the samples was measured by an

Agilent SPM 5500 atomic force microscope (Figure 3.4), equipped with a MAC III controller

and a RTESPA-525 tip which had the resonant frequency of 75 kHz. The average particle size of

different samples were also analyzed using this equipment. Also, quantitative nano-mechanical

(QNM) mode was used for measuring Young's modulus of the samples.

Figure 3. 4 Agilent SPM 5500 AFM equipment used for AFM analysis.

3.2.5 Raman spectroscopy

Raman spectroscopy was used to analyze crystalline phases of thin films and coated samples.

Horiba Raman system (Figure 3.5) was operated with 532 nm laser to obtain the Raman peaks of

different samples. The instrument was first calibrated with silicon (Si) crystal sample, after

which other samples were analyzed.
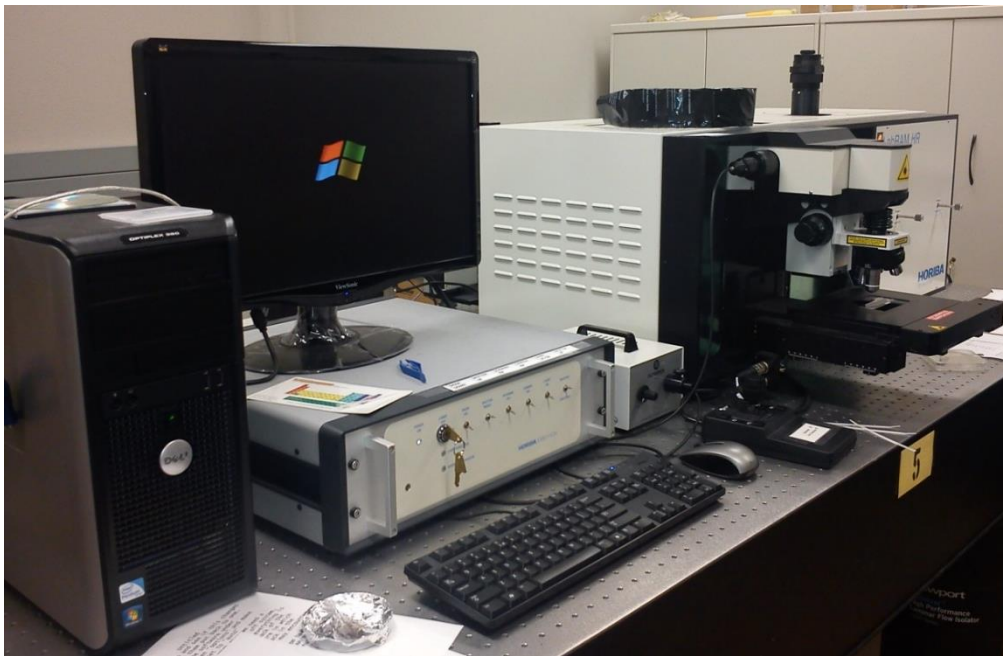
Figure 3. 5 Horiba Raman spectroscopy equipment used for Raman analysis.

3.3 Electrochemical characterizations

3.3.1 EIS, LSV, and CV

EIS measurements of symmetrical and full cell samples were performed using the Ametek

VERSASTAT3-200 potentiostat electrochemical workstation from Princeton Applied Research.

LSV and CV were measured using Biologic EC Lab potentiostat (Figure 3.6). For SSBs, EIS

measurements were performed over the working frequency range of 1 MHz to 100 mHz with

voltage amplitude of 10 mV AC signal. Also, 20 nm of gold (Au) layers were sputtered on both

sides of SSE pellet as blocking electrode. However, for LMBs with LE the frequency range was

set from 100 KHz to 0.1 Hz. Similarly, LSV measurements were performed from 0 to 5V range.

Also, CV was performed at voltage range of 2 to 4.5 V at scan rate of 0.5 mV s^{-1} v/s Li/Li$^+$.
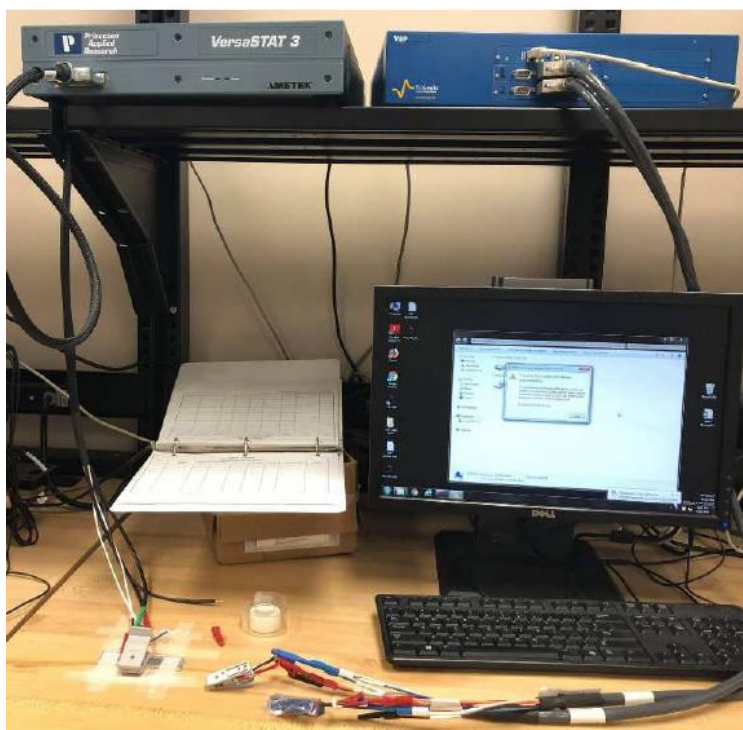
Figure 3. 6 VERSASTAT3-200 and Biologic EC Lab potentiostat equipment used for EIS,

LSV, and CV measurements.

3.3.2 Symmetrical and full cell test

Galvanostatic charge/discharge cycling measurements of assembled coin cells were performed using the LAND CT2001A and Neware battery analyzer systems (Figure 3.7). Li symmetrical cells with LEs were cycled at different current density such as 0.5, 1, 2, 3 mA cm^{-2} with capacity achieving 1 mAh cm^{-2}. Whereas those with SSE were cycled upto 0.2 mA cm^{-2} during plating/stripping cycles and upto 1 mA cm^{-2} during critical current density (CCD) cycling experiment. Similarly, for full cell with LEs, the cells with LFP cathodes were cycled in a voltage range of 4.2 to 2.5 V at different current densities (e.g., 1C = 170 mA g^{-1}). The specific capacity at 1 C was calculated by using the mass of active cathode material, LFP. For capacity retention and rate performance tests the cells were cycled at 0.2 C, 0.5 C, 1 C, 2 C, 5 C, and back to 0.5 C-rates. Whereas the solid-state hybrid LFP full cells were cycled at the voltage range of 4 to 2.5 V. The specific capacities at 0.2 C-rate current density was calculated and cells were further cycled at 0.1 C, 0.2 C, 0.5 C, 1 C, and back to 0.1 C-rate for capacity retention and rate performance tests.
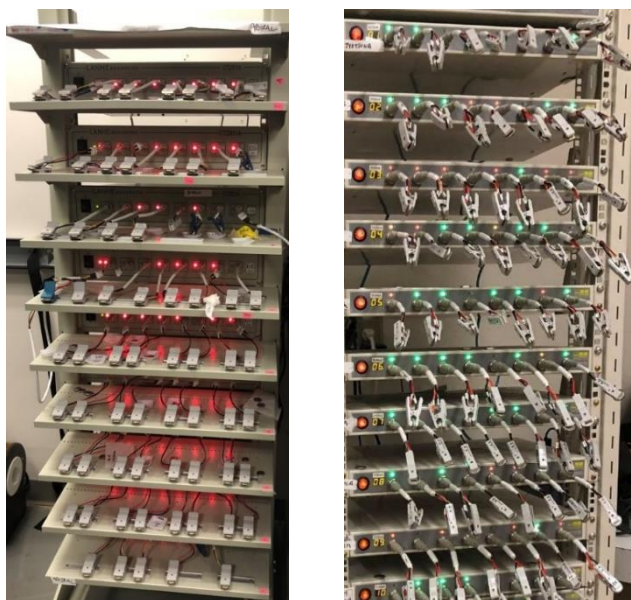
Figure 3. 7 LAND CT2001A and Neware battery analyzer for coin cells testing.

Chapter 4: Results and Discussions

4.1 Functional electrolyte additive engineering

In this work, the use of novel electrolyte additive, gadolinium nitrate ($Gd(NO_3)_3$) at optimal concentration of 3 mM added in $LiTFSI-LiNO_3$ ether solvent based LE was reported. The use of additive tuned the composition of SEI layer on the top of LMA as the components of the electrolyte additive get reduced prior (Gd^{3+} (E°) = - 2.279 V, Li^+ (E°) = -3.040 V v/s SHE) [261] to electrolyte reduction which passivated the Li metal surface preventing further electrolyte decomposition and formation of high electronegative fields that favors dendritic deposition of Li ions. Further, a nodular morphology of Li deposition was observed with use of this additive which promoted dendrite free Li deposition. As a result, much improved and enhanced battery cycling performance was obtained.

4.1.1 Li morphology and surface characterizations

SEM images were taken on the surface of Li metals (Figure 4.1), showing the morphology of deposited Li at different plating/stripping cycles. It can be observed from Figure 4.1 (a) that dendritic structures start to grow within 1st cycle of plating/stripping when no additive was added to the electrolyte. The condition exacerbates on the 10th cycling number (Figure 4.1 (b)) and gets even worse at 100th cycle (Figure 4.1 (c)), evidenced by the excessive presence of dendritic and dead Li on LMA surface. However, when electrolytes with presence of $Gd(NO_3)_3$ additive was used for Li plating/stripping cycles the growth of dead and dendritic Li were much suppressed (Figure 4.1 (d-f)), showing nodular morphology of Li deposition. The micro-sized nodular Li morphology with large particle deposition size and small area inhibits the parasitic side reactions between LMA and electrolyte, enabling significantly improved CE and leading to enhanced cycling stability of LMBs [262]. Further, the digital images on insets of Figure 4.1 (c, d) shows

the superior stability of SEI layer tuned by adding Gd(NO$_3$)$_3$ electrolyte additive. This is revealed from the surface of bare Li changing from shiny silver color to dark dull color (Figure 4.2 (c)) after 100 cycles, showing the formation of extra insulating layers due to side reactions and consumption of electrolyte. Whereas the cycled LMA with additive added electrolyte still looks shiny and silver in color even after 100 cycles, attributed to formation of stable SEI layer and improved passivation of Li metal.
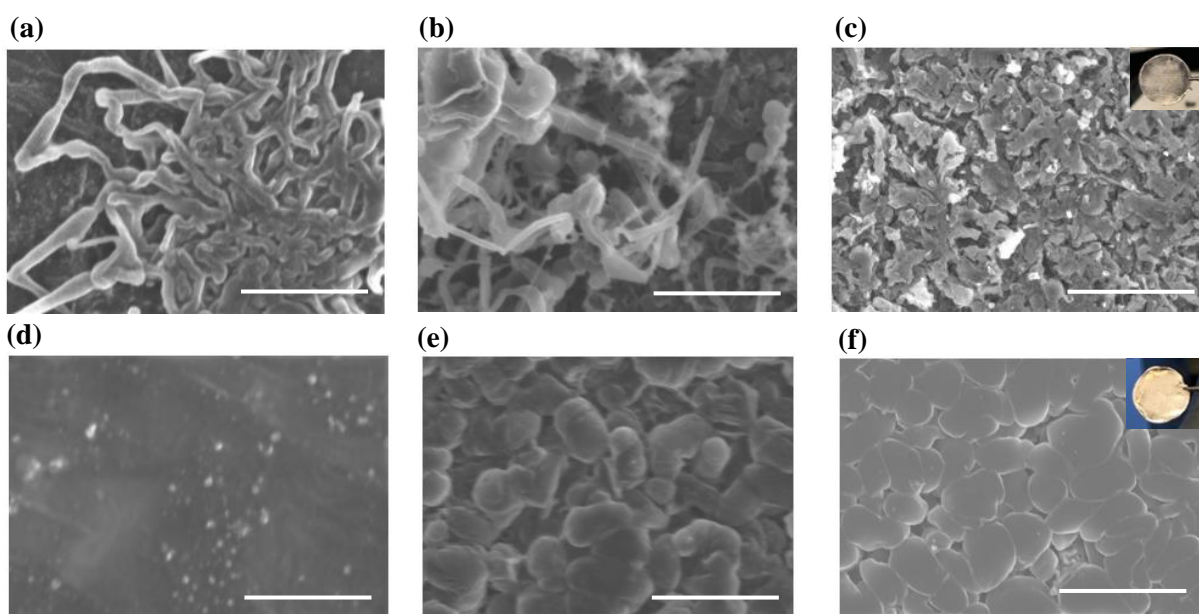
Figure 4. 1 SEM images of LMAs showing the Li deposition morphologies on it for 1st (a, d), 10th (b, e), and 100th (c, f) plating/stripping cycles without (a, b, c) and with (d, e, f) Gd(NO$_3$)$_3$ electrolyte additive. The inset on images (c) and (f) shows digital images of respective cycled LMAs. All SEM scale bars are 20 μm.

Generally, the nodular structures of Li are formed when Li deposition is carried out in highly concentrated electrolytes such as 4 M lithium bis(fluorosulfonyl)imide (LiFSI) +DME [99], 7 M

LiTFSI in DOL:DME [263], 4.5 M LiFSI in acetonitrile (AN) [264], 4 M LiNO$_3$ in dimethylsulfoxide (DMSO) [265], and 3 M LiTFSI-DME [266]. Although from the notion of solution theory, a higher fraction of free solvents for solvation should result in stronger and faster solvency, our results contradict this conventional wisdom demonstrating outstanding capabilities of dilute electrolytes enabled by use of functional additives. Also, batteries with diluted electrolytes are less expensive, lighter, have wider operating temperature, and uses less viscous electrolytes compared to conventional high-M electrolytes.

For the elemental and surface analysis of Li metal cycled without and with Gd(NO$_3$)$_3$ additive in electrolyte, EDS and contact angle measurements were performed. Figure 4.2 (a, b) shows the EDS spectrum of Li metal cycled without and with electrolyte additive, respectively. The EDS spectrum reveals the presence of Gd (Figure 4.2 (b)) in Li metal cycled with electrolyte additive along with nitrogen (N), oxygen (O), fluorine (F), and sulfur (S) relating to other elements present in LiTFSI in DOL-DME baseline electrolyte. On the other hand, there was no presence of Gd observed in EDS analysis of Li metal surface cycled in electrolyte without additive (Figure 4.2 (a)). Similarly, the wetting property of these electrolytes with Li metal was investigated using contact angle measurement on Li metal (Figure 4.2 (c, d)). It was observed that the wetting of additive added electrolyte (Figure 4.2 (d)) was much better compared to that for baseline electrolyte with no additive (Figure 4.2 (c)), evidenced by decrease in angle of contact from 26.20 to 13.50 °. This increase in wettability of additive added electrolytes with Li metal helps to form a uniform and stable SEI layer, covering the whole LMA area ensuring improved passivation of LMA without cracks and voids. This increase in wettability of additive added electrolyte can be associated with presence of Gd on the Li metal surface which was exhibited by EDS analysis as mentioned before.

(a)

(b)

(c)

Angles: [26.80°,26.20°]

(d)

Angles: [11.20°,13.50°]
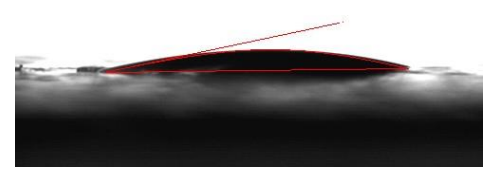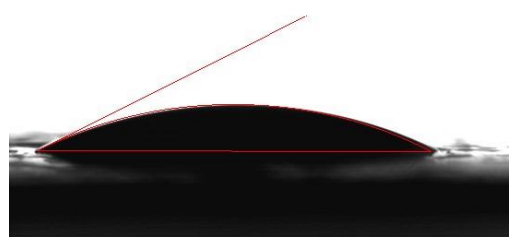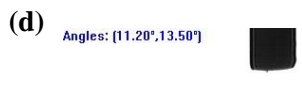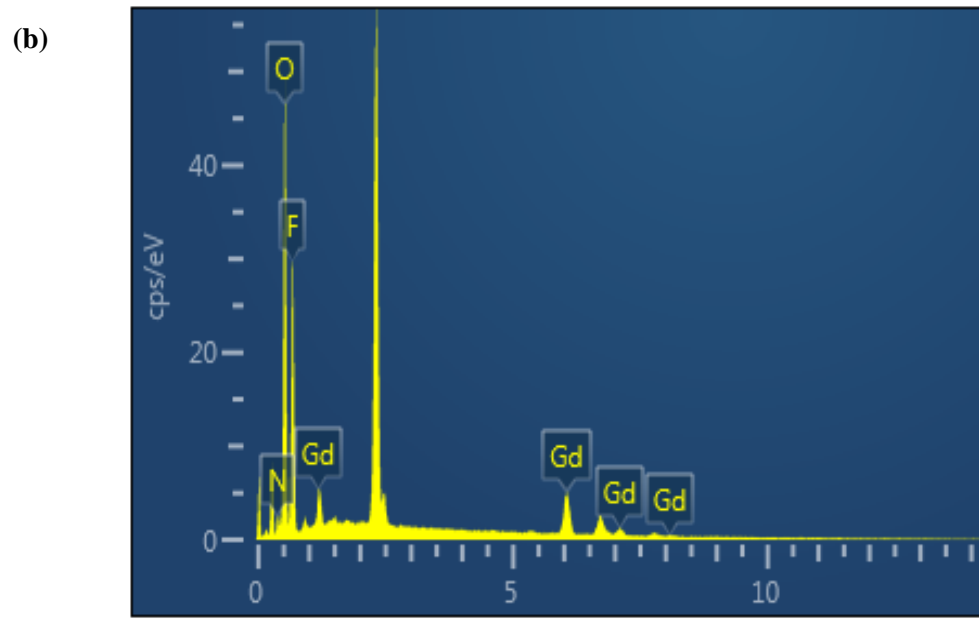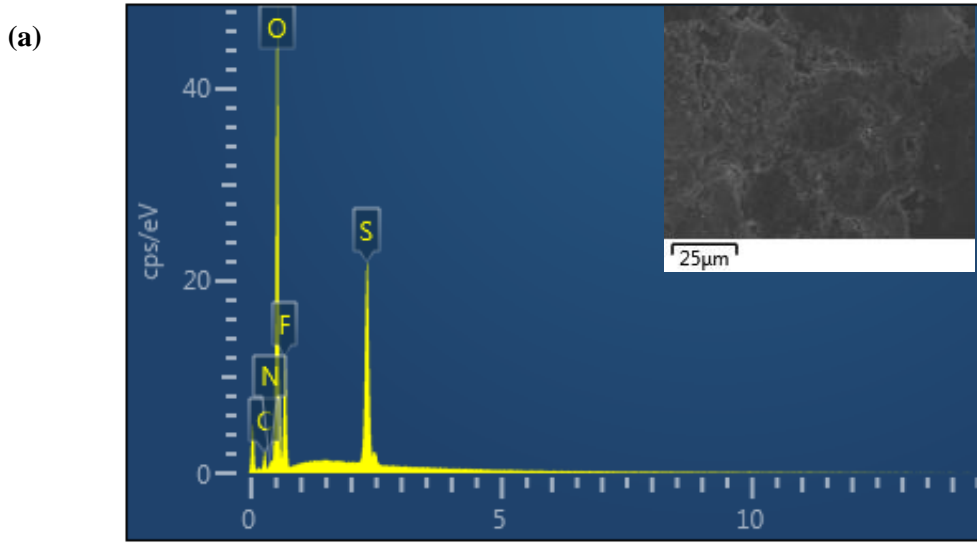
Figure 4. 2 EDS spectrum of LMA surface showing (a) absence of electrolyte additive element Gd for cells cycled without additive, whereas (b) its presence in cells cycled with additive, and contact angle measurements of electrolytes on Li metal (c) without $Gd(NO_3)_3$ additive, (d) with $Gd(NO_3)_3$ additive.

Additionally, for the chemical state analysis of surface SEI layer formed during cycling of LMAs, XPS analysis was performed which revealed the products formed by additive promoted reactions in SEI. Figure 4.3, shows the Gd 4d XPS spectra of cycled LMAs surface. For Li metal samples cycled without electrolyte additive (Figure 4.3 (a)), there was no significant peaks observed. Whereas those cycled with electrolyte additive (Figure 4.3 (b)), fitted peaks at ~142.4 eV and another peak at ~ 138.8 eV were observed which are very consistent with the formation of gadolinium oxide (Gd_2O_3) in the SEI layer [267].

(a)

(b)
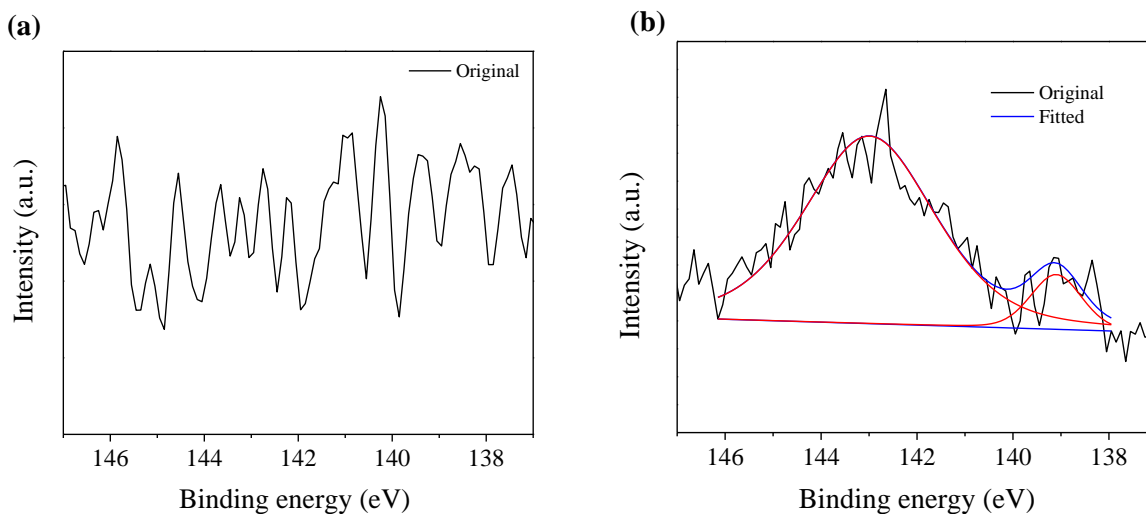
Figure 4. 3 Gd 4d XPS spectra for cycled LMA (a) without, and (b) with $Gd(NO_3)_3$ electrolyte additive.

Similarly, the XPS measurements for C 1s, N 1s, O 1s, F 1s, S 2p, and Li 1s spectra were also performed and their elemental ratio (%) in the Li metal surface were computed taking into consideration the sensitivity factors for each spectrum. As shown in Table 4.1, the SEI layer on LMAs for both set of electrolytes are composed of typical organic and inorganic compounds such as CH_2OCO_2Li, $ROCO_2Li$, and LiF [268-270]. However, the SEI layer on Li metal formed by reaction with additive added electrolyte consists of less oxygen, fluorine, and sulfur elements which are associated with LiTFSI lithium salt in the electrolyte. This indicates that the nitrate anions improve the stability of electrolytes against Li metal and prevents severe decomposition of Li salt such as LiTFSI during battery operation.

Table 4. 1 Elemental ratio (%) from different XPS analysis spectra

XPS spectra	No additive	$Gd(NO_3)_3$ additive
C 1s	27.6	30.1
N 1s	4.1	5.4
O 1s	23.3	20.8
F 1s	20.5	18.2
S 2p	7.4	6.8
Li 1s	17.1	18.5
Gd 4d	0.0	0.2

4.1.2 Electrochemical characterizations

Various electrochemical characterizations were performed on both Li symmetrical cells and full cells to analyze and compare the electrochemical performance of batteries cycled with and without adding electrolyte additive. At first, a series of symmetrical cell test with different amounts (mg ml^{-1}) of additives in electrolyte were carried out in order to optimize the amount of additive in the electrolyte. As shown in Figure 4.4, the 1 mg ml^{-1} amount which calculates around 3 mM of electrolyte additive in 1 M LiTFSI-LiNO$_3$ ether solvent based electrolyte, exhibits best performance with longer plating/stripping hours and lower voltage overpotential compared to samples with other additive concentrations. The lesser additive concentration may not be enough to show its full effect on SEI formation, similarly, high additive concentration can form more resistive SEIs. Thus, the additive concentration was optimized to 1 mg ml^{-1}.
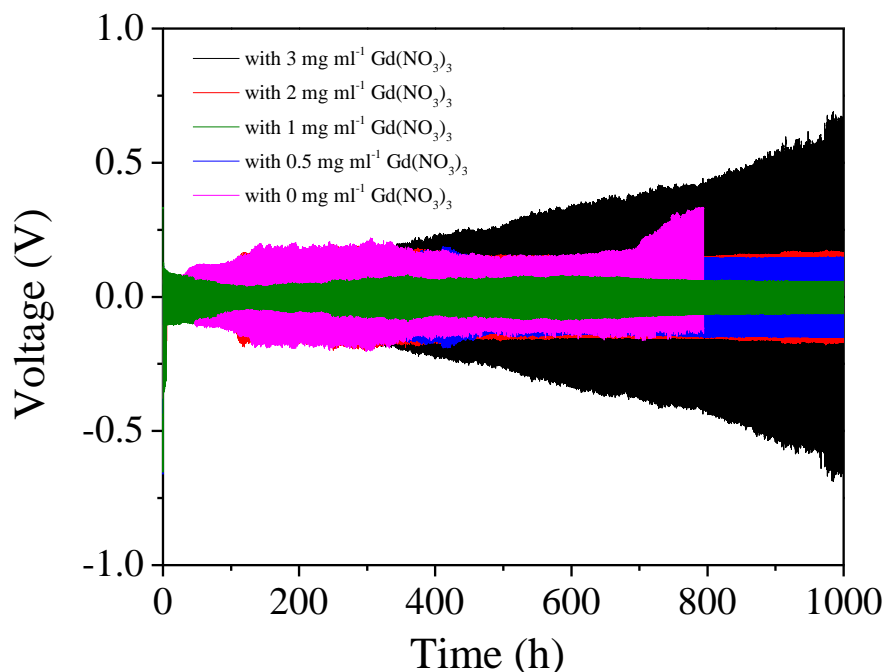
Figure 4. 4 Li symmetrical cell test with different additive amount in the electrolyte.

Further, to observe the charge transfer properties and Li plating/stripping stability, EIS and Li symmetrical cycling tests were performed. As shown in Figure 4.5 (a), the Nyquist plot derived from the EIS characterization depicted that introducing $Gd(NO_3)_3$ as electrolyte additive reduces the total charge transfer impedance from 130 Ω (without additive) to 60 Ω. The significant reduction of charge transfer resistance can be attributed to $Gd(NO_3)_3$ additive promoting conformal coating of LMAs with low resistance and ionically conductive SEI layer.

Similarly, galvanostatic Li plating/stripping cycling tests were performed under both low (0.5 mA cm^{-2}) and high (2 mA cm^{-2}) current densities. Figure (4.5 (b)) shows the voltage profile for plating/stripping cycles of Li symmetrical cells based on electrolytes with and without additive at current density of 0.5 mA cm^{-2}, reaching capacity of 1 mAh cm^{-2}. It can be observed in Figure (4.5 (c)), its voltage profile from 675 to 695 cycling hours (more stable region), that the symmetric cell cycled with no electrolyte additive shows large overpotential of $\pm$ 70 mV, while the cell with use of electrolyte additive suppressed this overpotential to $\pm$ 20 mV. This indicates that introducing electrolyte additive reduced the energy barrier of Li transfer process, thus facilitating efficient Li plating/stripping cycles. Also, longer plating/stripping cycles for additive added cells were observed as they were stable for 2000 h, compared to ~600 h for cells with no electrolyte additive, suggesting the formation of stable SEI on the LMAs for cells with electrolyte additive. Similar stable cycling of upto 1200 h at higher current density of 2 mA cm^{-2} and capacity 1 mAh cm^{-2} was demonstrated by the additive added Li symmetrical cells with voltage stabilized at $\pm$ 58 mV, while the cells cycled with no additive was stable for only 200 h with very large voltage overpotential of $\pm$ 200 mV (Figure 4.5 (d)).
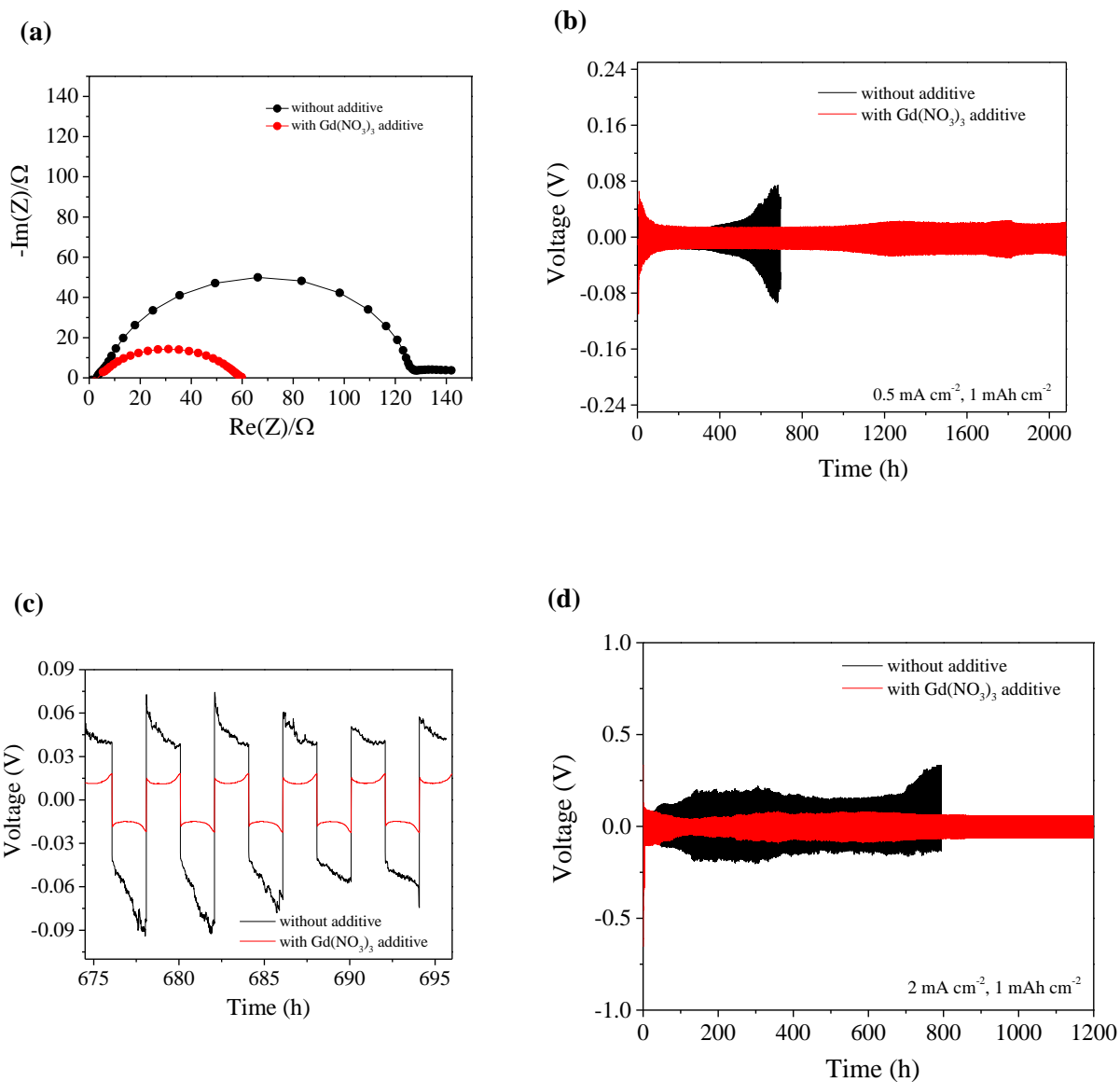
Figure 4. 5 Li symmetrical cell tests showing (a) Nyquist plots from EIS test, (b) cycling test at current density of 0.5 mA cm^{-2} and 1 mAh cm^{-2} capacity, (c) voltage profile between 675 to 695 cycling hours, and (d) cycling test at 2 mA cm^{-2} current density and 1 mAh cm^{-2}; for cells with and without Gd(NO$_3$)$_3$ electrolyte additive.

Further, to demonstrate the potential of enabling high energy density practical LMBs, full cells were assembled and tested. The LSV and CV characteristics of Li/NMC 111 full cells were analyzed to observe the high voltage stability and reaction mechanisms of cells with and without electrolyte additive (Figure 4.6). As shown in Figure 4.3 (a, b), electrolyte reduction peaks are observed on both type of cells. Whereas when the plots were enlarged, the cells without additive showed multiple reduction peaks (Figure 4.3 (a), inset), indicating multiple reduction side reactions occurring at the interface. These multiple peaks were suppressed showing only single peak of reduction reaction, indicating suppression of side reactions by use of electrolyte additive (Figure 4.3 (b), inset). Also, comparing Figure 4.3 (a) and (b), significant electrolyte decomposition is observed after ~ 4.2 V for cells without electrolyte additive, whereas such decomposition is inhibited as side reactions, main cause of electrolyte decomposition, are suppressed by use of electrolyte additive. Similarly, Figure (4.3(c)) shows the CV scanning of Li/NMC 111 cells, which suggests that the oxidation/stripping peak potential is increased to 4.08 V for additive added cells than that to 3.9 V for control electrolyte added ones.

(c)
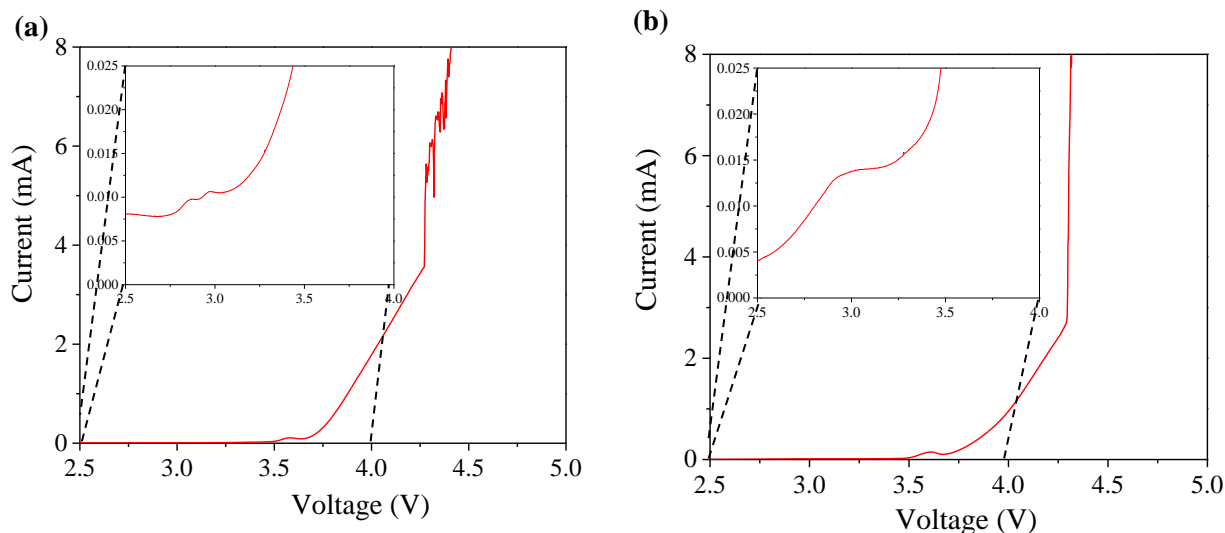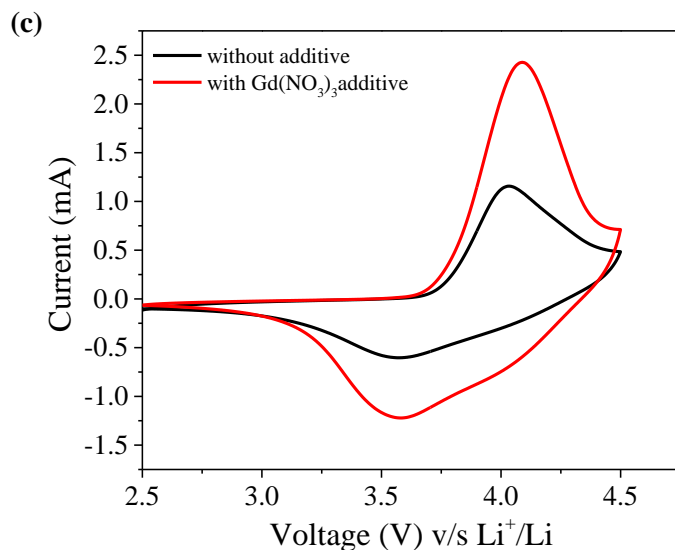
Figure 4. 6 LSV analysis of full cells (a) without, (b) with Gd(NO₃)₃ electrolyte additive, inset

on showing enlarged plot from 0-0.0025 mA current; and (c) CV plot of full cells with and

without electrolyte additive.

The CV curves also show much higher plating/stripping current, resulting in overall larger CV

curve area for cells cycled in electrolyte with additive than that without additive, verifying the

effectiveness of Gd(NO₃)₃ electrolyte additive to enhance the electrochemical kinetics, and

suggesting a lower energy barrier for the Li deposition thus improving cell capacity [271, 272].

In addition, the R_{ct} of Li/NMC 111 full cells at different cycles were also compared using EIS

and is listed in Table 4.2. It shows the evidence that full cells cycled with electrolyte additives

shows low R_{ct}, compared to those without additives, which supports the notion of enhanced

charge transfer and reaction kinetics are favored using electrolyte additives. The decrease in R_{ct}

for cells without additive after 10 and 50 cycles can be attributed to the formation of high surface

area Li dendrites allowing more electrolyte contact and consumption. In contrast, the similar

decrease for cells with Gd(NO₃)₃ additive can be attributed to stabilization of *in-situ* SEI after 10

and 50 cycles favoring Li deposition in smooth nodular morphology with less surface area,

reducing the undesired contact between Li an electrolyte during battery cycling.

Table 4. 2 Comparison of R_{ct} at different cycle numbers

Cycle number	Without additive	With Gd(NO₃)₃ additive
0 cycle	286.855 Ω	184.4999 Ω
5 cycles	700 Ω	439.87 Ω
10 cycles	734.71 Ω	490.89 Ω
50 cycles	515 Ω	477 Ω
100 cycles	500 Ω	286.94 Ω

To evaluate the application of electrolyte engineered batteries in the field, LFP cathode was used

as active cathode material to assemble a LMA full cell. Different metrices such as cycling

performance, discharging capacity, and CE were compared between full cells cycled using

electrolytes without and with additive (Figure 4.7).

(a)
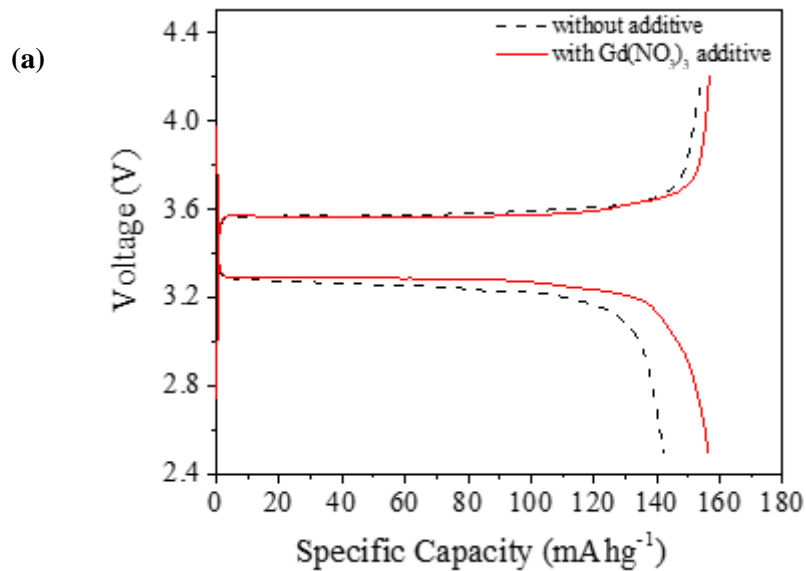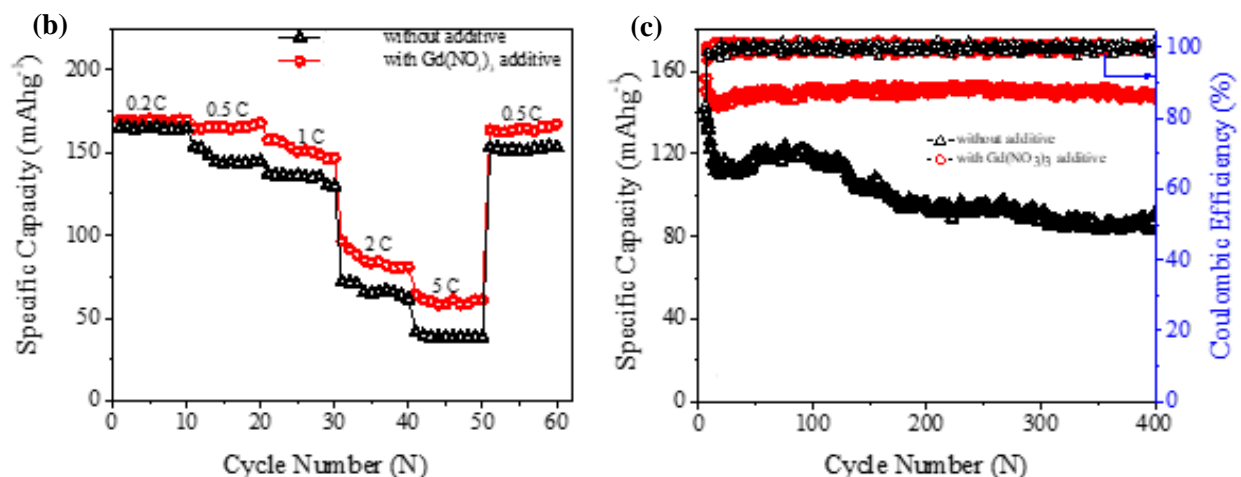
Figure 4. 7 (a) 1st cycle voltage profile of Li/LFP full cell at 1 C-rate. (b) Rate performance and capacity retention test of Li/LFP cells, (c) Long-term cycling performance of Li/LFP cells at 1 C-rate, with and without electrolyte additive.

Figure 4.7 (a), shows the charge/discharge voltage profile during 1st cycling of Li/LFP LMB at 1 C-rate. The first discharge capacities of 156.295 and 142.057 mAh g^{-1} with CE of 87.819 and 84.112 % were observed for cells with and without Gd(NO$_3$)$_3$ electrolyte additive, respectively. The lower CE observed in cells without electrolyte additive can be attributed to parasitic side reactions and formation of unstable SEI layer, on the other hand, use of additive shows high CE ensuring stabilized SEI and suppressed side reactions. These full cells were further cycled at different C-rates from 0.2, 0.5, 1, 2, 5 and back to 0.5 C. As shown in Figure 4.7 (b), the cell with/without electrolyte additive exhibited discharge capacities of 169.83/165.075, 164.84/153.275, 157.69/137.05, 96.58/71.925, and 64.15/41.228 mAh g^{-1} at 0.2, 0.5, 1, 2, and 5 C, respectively. Also, when the C-rate was set back to 0.5 C, the cells with electrolyte additive displayed the discharge capacity retention of 166.99 mAh g^{-1}, which accounts for 98.33 % of the

initial capacity after ten cycles of each higher C-rates. Similarly, long term cycling performance and capacity fade characteristics were tested by cycling Li/LFP cells for higher number of cycles as shown in Figure 4.7 (c). The cycling performance of additive added cells are highly improved as they still maintain the discharge capacity of 150.266 mAh g^{-1} at 400th cycle compared to 92.962 mAh g^{-1} for that without additive. This superior cycling performance and much reduced capacity fade further validates the efficacy of using $Gd(NO_3)_3$ as electrolyte additive and its contribution to form a stable SEI layer, promoting nodular Li deposition, inhibiting Li dendrite growth, and suppressing uncontrolled side reactions between electrolyte and LMA.

4.2 LMA/SSE interfacial engineering

In this work, a novel metal nitride LMA/SSE interface modifier, silicon nitride (Si_3N_4) thin film was coated onto the garnet $Li_{6.25}Al_{0.25}La_3Zr_2O_{12}$ (Al-LLZO) solid electrolyte by Radio frequency (RF) sputter deposition method. This interfacial layer ensured an intimate physical contact and homogeneous current distribution at the LMA and SSE interface. The deposited nitride interface, Si_3N_4@Al-LLZO, showed lithiophilic property when Li metal was melt infused in its surface. This lithiophilic behavior and reduction in contact resistance by depositing Si_3N_4 interfacial layer was attributed to formation of Li ion conductive ternary phase alloys at the interface. These alloys not only wets Li well but also provides open tunnels for Li ion conduction at the interface. Thus, deposition of this thin layer at the LMA/garnet SSE interface enabled exponential drop of resistance at the interface facilitating superior SSB cycling performance.

4.2.1 Material characterizations
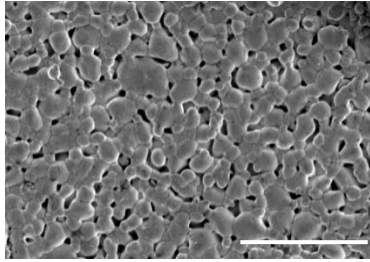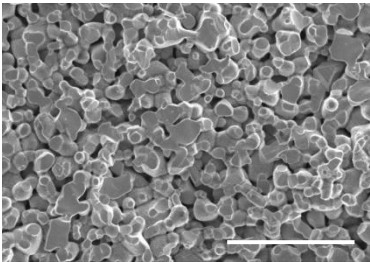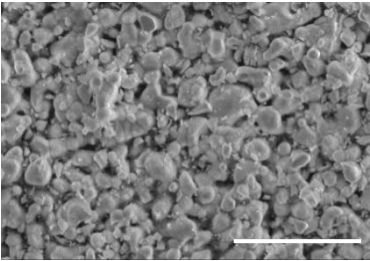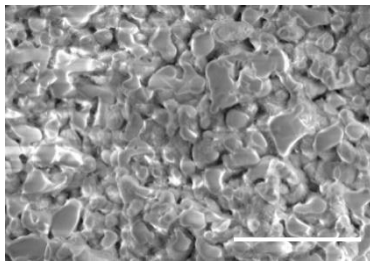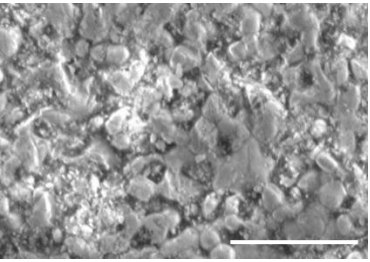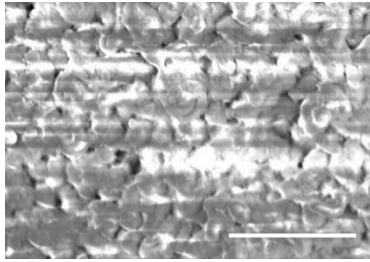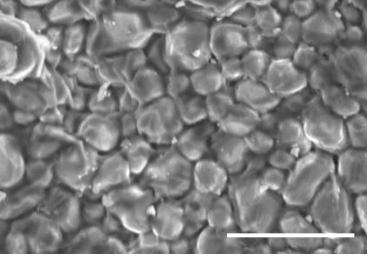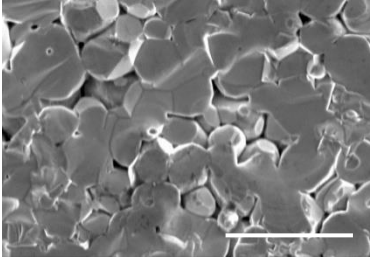
4.2.1.1 Structure and composition of Al-LLZO

Various amounts of Al-LLZO nanopowder was first pressed and sintered at different pressures and sintering temperatures. 0.4 mg and 80 MPa of nanopowder amount and pressing force, respectively, resulted in formation of 10 mm diameter and 1 mm thick pellets that can efficiently hold its pellet structure. Next the sintering temperature was optimized by sintering pressed pellets at different temperature and analyzing their crystal phase and relative density at each sintering trials. Table 4.3 shows the SEM images and relative density values for pellets sintered at different temperature.

The surface and cross-section images of pellets were densified with majority of grains tightly connected when sintering temperature was raised to 1280 °C (Table 4.3). When the relative density of sintered pellets were measured using Archimedes' principle with ethanol as immersion liquid, for temperatures below 1280 °C, not more than 90 % relative density was obtained [273]. Whereas for pellets sintered at 1280 °C, a relative density of ~ 92 % was observed. As the sintering temperature was increased above 1280 °C, the pellets melts and tend to stick on the surface of the crucible, so heating above 1280 °C was avoided. The digital photo of this occurrence is also provided in Table 4.3. Therefore, the optimal sintering temperature of 1280 °C with sintering duration of 1 h was applied for obtaining best quality SSE pellet samples.

After, optimizing the sintering temperature and duration, the crystal phase and presence of any impurities in it was tested. First, the garnet pellets sintered at different temperature were dry polished to remove Li_2CO_3 and LiOH insulting layers and XRD analysis was performed on them to find their crystal phase and purity.

Table 4. 3 SEM images and relative densities of Al-LLZO pellets sintered at different temperature. All the scale bars are 20 µm.

S.N.	Surface	Cross-section	Sintering temperature	Relative density
1			1100 ^{o}C	80%
2			1230 ^{o}C	87.5%
3			1250 ^{o}C	90.2%
4			1280 ^{o}C	92%

| 5 | | >1280 $^{\circ}$C | Pellets melts and attaches to the crucible above 1280 °C. |

The XRD results of polished pellets sintered at 1000 °C showed the presence of impurity peaks indexed to $La_2Zr_2O_7$ (PDF #50-0837) (Figure 4.8 (c)), marked as red asterisk (*) in Figure 4.8 (a). Formation of this impurity phase was attributed to reaction shown in equation (4.1).
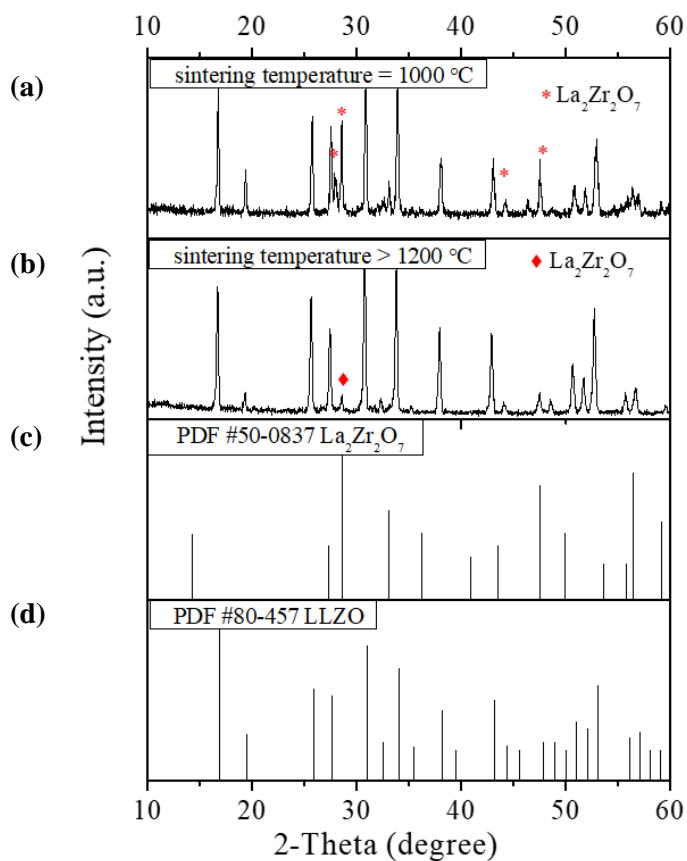
Figure 4. 8 XRD analysis showing presence of impurity phase on SSE pellet which was removed after increasing the sintering temperature above 1200 °C.

$$Li_2CO_3 + La_2O_3 + 2ZrO_2 \rightarrow Li_2O + La_2Zr_2O_7 + CO_2 \qquad (4.1)$$
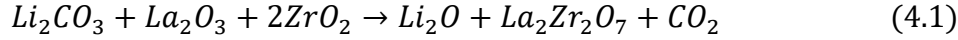
As the sintering was performed in ambient conditions, it might have introduced Li_2CO_3 to the samples during heating. However, when temperature is increased to 1200 °C, Li_2O reacts with $La_2Zr_2O_7$ to form LLZO particles again and releasing CO_2, as shown in equation (4.2) [274]. This was also evidenced by disappearance of $La_2Zr_2O_7$ impurity XRD peaks as shown in Figure 4.8 (b).

$$7Li_2CO_3 + 3La_2O_3 + 4ZrO_2 \rightarrow 2Li_7La_3Zr_2O_{12} + 7CO_2 \qquad (4.2)$$
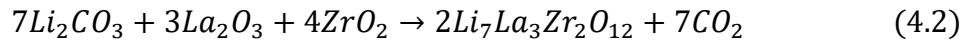
When XRD peaks of pellets sintered above 1200 °C were compared with cubic phase LLZO XRD peaks, PDF #80-457 (Figure 4.8 (d)), most of the impurity peaks of La_2ZrO_7 disappeared and the one at 29° was highly suppressed represented as red diamond ($\blacklozenge$).
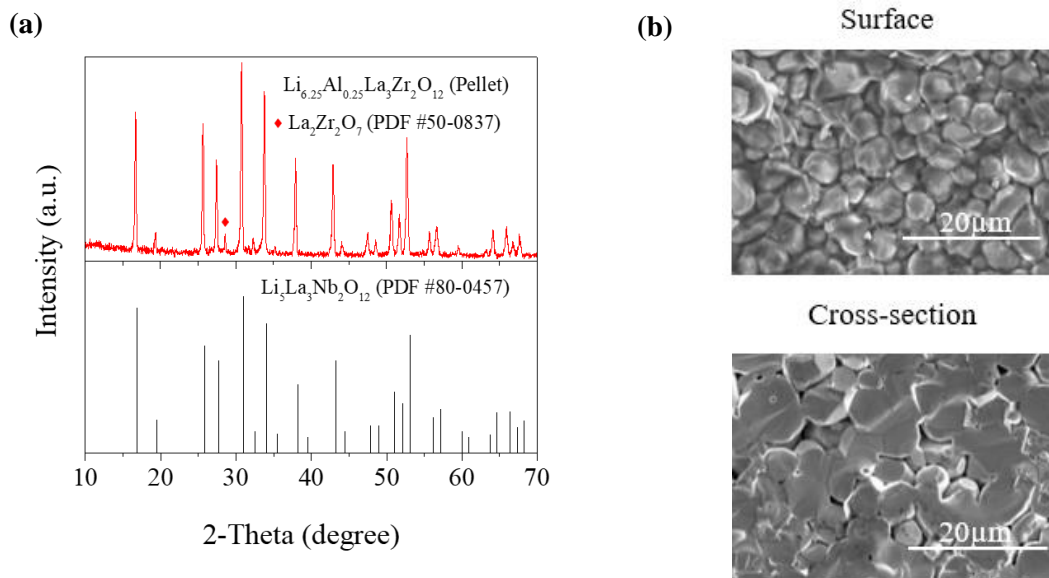
Figure 4. 9 (a) XRD comparison of optimized garnet pellets with cubic garnet structure, and (b) SEM images of thus obtained garnet Al-LLZO.

Thus, as shown in Figure 4.9 (a), when applying optimized sintering temperature of 1280 ℃, the Al-LLZO pellets showed resemblance to the standard pattern of cubic garnet phase $Li_5La_3Nb_2O_{12}$ (PDF #80-0457). Further, the SEM images of Figure 4.9 (b) shows formation of well densified pellets with tightly connected grains when pellets were sintered at 1280 ℃ for 1h.

4.2.1.2 Interfacial layer properties

After optimizing the parameters for obtaining dense and cubic phase Al-LLZO pellets, a thin film of Si_3N_4 was sputter coated on their top, Si_3N_4@Al-LLZO. Figure 4.10 (a, b), shows the digital images of as prepared bare Al-LLZO garnet pellet and that after depositing thin layer of Si_3N_4 on its surface, respectively. As observed from these figures, the Si_3N_4 layer was light grey to yellowish in color, which is typical color of it for nm range thickness [215]. Figure 4.10 (c), shows the Raman spectrum of Si_3N_4@Al-LLZO. The Raman peaks at 258, 363, 565, 850-870, and 951 cm^{-1} represents characteristic peaks of α- phase crystalline Si_3N_4 and is denoted by ♦ [275]. Whereas the remaining peaks denoted by * are characteristic peaks of cubic phase Al-LLZO [276].

(a)   (b)
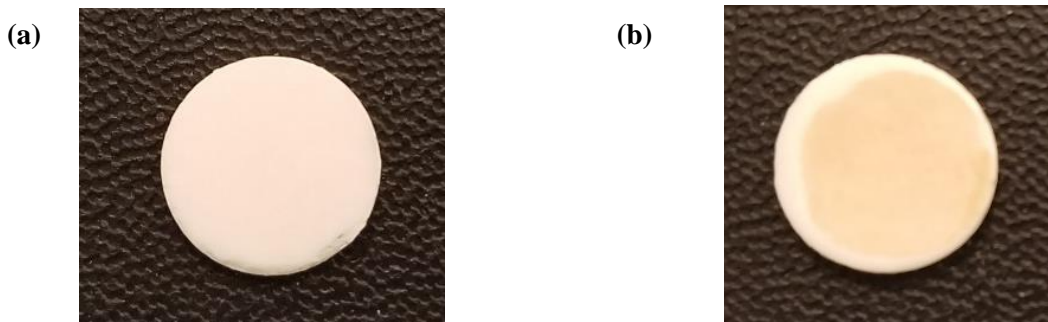
(c)
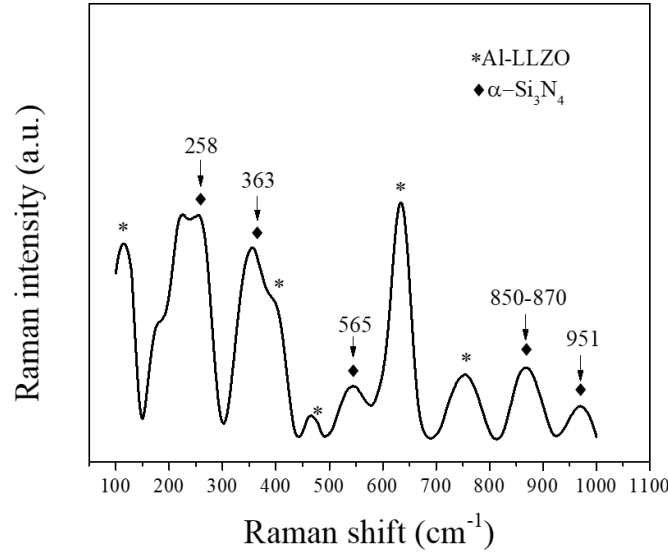
Figure 4. 10 Digital images of as-prepared (a) bare Al-LLZO, (b) Si_3N_4 layer coated Al-LLZO, SSE pellets around 1 mm thick, and (c) Raman spectroscopy of Si_3N_4@Al-LLZO.

Similarly, EDS characterization was performed on Si_3N_4@Al-LLZO for obtaining its elemental mapping information. Figure 4.11 (a) shows the EDS spectrum and elemental mapping of Si_3N_4@Al-LLZO pellet. The spectrum shows the presence of Si and N, conforming the deposited layer is of Si_3N_4, and other elements such as La, Zr, and Al that is attributed to the components from Al-LLZO solid electrolyte. Also, the elemental mapping shows the uniform distribution of Si and N on the garnet surface, assuring the conformal coating and full coverage of deposited area by Si_3N_4 thin film.

Additionally, AFM analysis was performed on dry polished bare (Figure 4.11 (b)) and Si_3N_4 modified (Figure 4.11(c)) pellet samples to analyze the surface roughness by comparing their root mean square (RMS) values. From AFM analysis, the RMS values of 640.2 nm and 394.4 nm were obtained for bare and Si_3N_4@Al-LLZO SSE pellet samples. The higher RMS value for bare samples shows its uneven and rough dry polished surface which will lead to poor contact
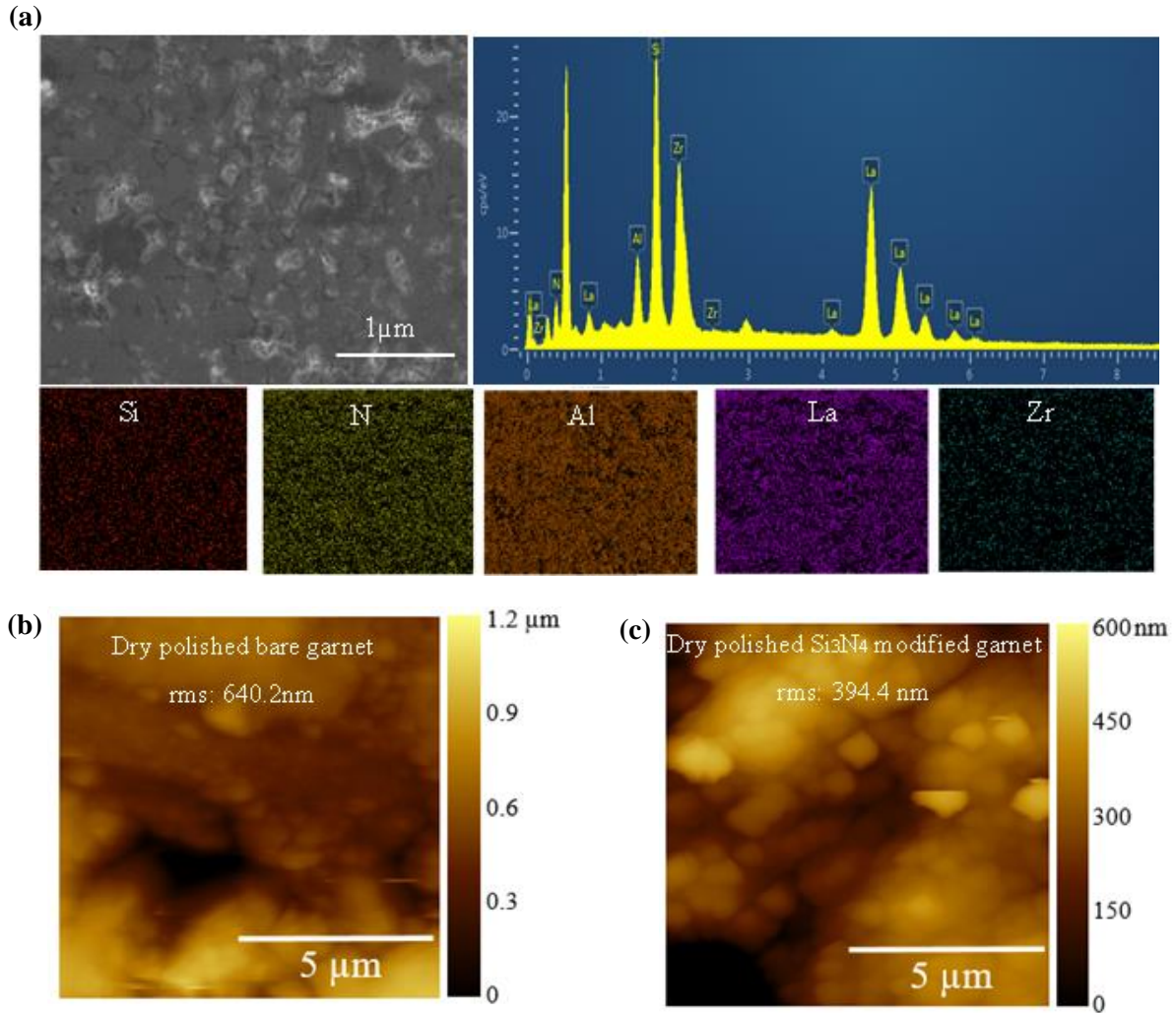
Figure 4. 11 (a) EDS spectrum of Si_3N_4@Al-LLZO samples showing presence of Si and N along with other elements from Al-LLZO, and AFM topography mapping of dry polished (b) bare garnet, and (c) Si_3N_4@Al-LLZO garnet.

[277], and uneven current distribution [278, 279] at the interface when these samples are in contact with LMA. This will further result in electron penetration in SSE bulk on certain spots leading to infiltration of SSE by whisker growth of Li metal [280]. However, the lower RMS

value observed for Si_3N_4@Al-LLZO samples ensures much more stable Li conduction at the interface and good interface contact which is conducive for long term cycling of SSBs [119].

The molten Li metal was brought in contact with Al-LLZO garnet SSE to test its surface Li wetting property. As shown in Figure (4.12 (a)), when molten Li was placed on the top of bare Al-LLZO garnet, it immediately curled to form a ball shape, revealing its lithiophobic surface property. On the other hand, when Si_3N_4@Al-LLZO was brought in contact with molten Li, the surface showed much better Li wetting as Li readily wets and spreads out on Si_3N_4 deposited Al-LLZO garnet surface. This showed that Si_3N_4 deposition turned the garnet surface to lithiophilic.
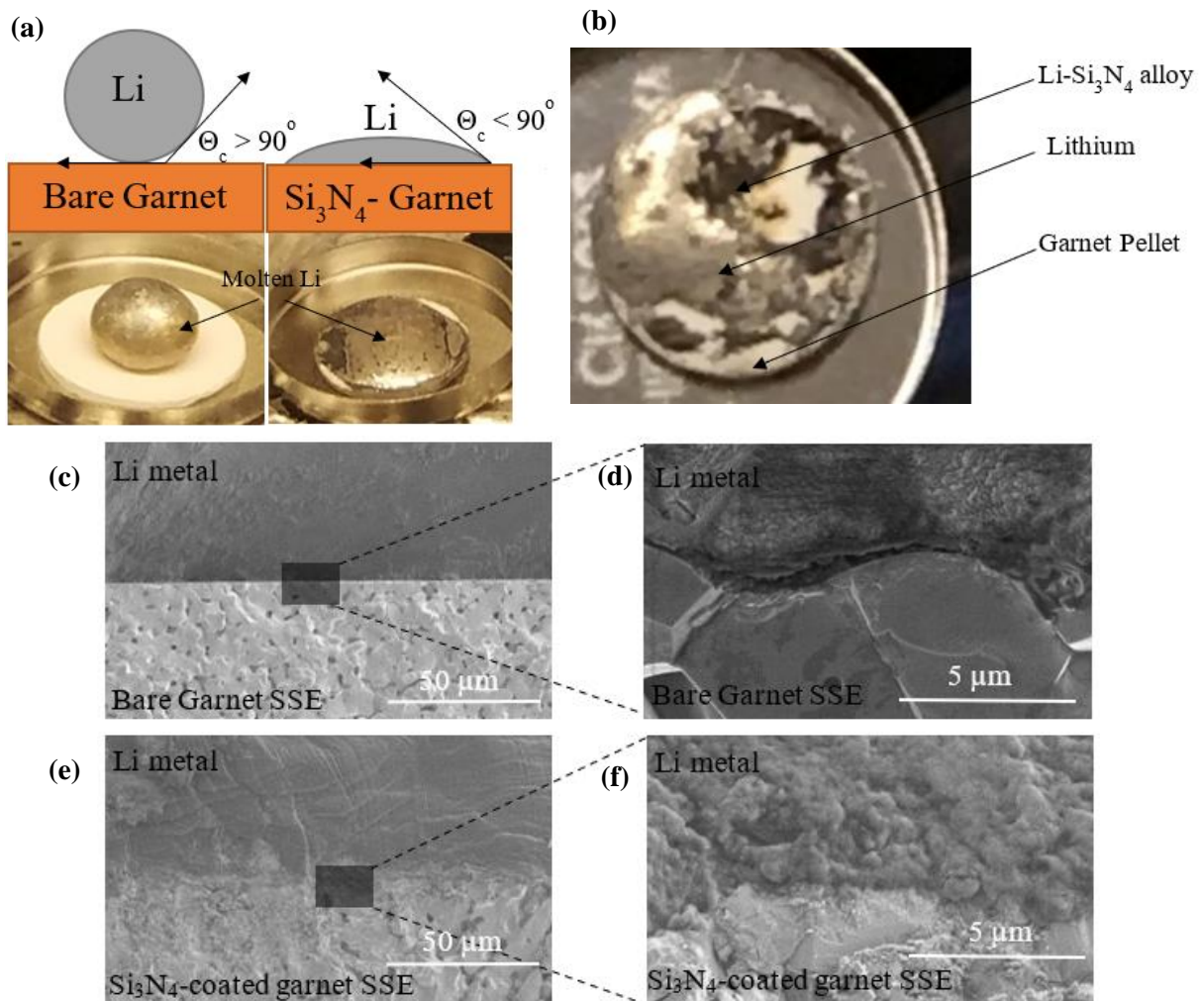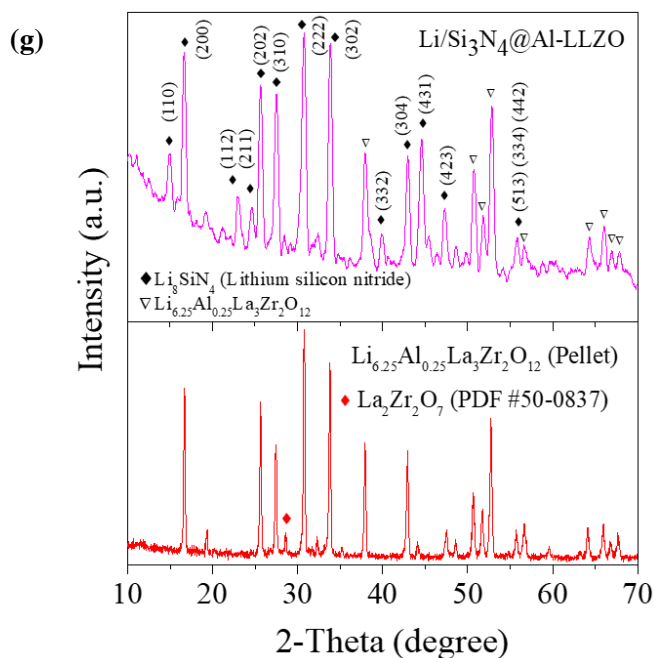
Figure 4. 12 Wetting behavior and interface characterization of Si₃N₄@Al-LLZO pellets (a) Digital images and schematics showing wetting property of Li metal on bare and surface modified garnet pellet, (b) Reaction propagation on lithiated Si₃N₄ layer deposited on garnet pellet, Cross-section SEM images of Li/Al-LLZO interface (c, d) without and (e, f) with Si₃N₄ interlayer; and (g) XRD spectrum showing formation of ternary phase alloys facilitated by Li metal and Si₃N₄ interlayer reaction.

To further decipher the reason behind the Li wetting property of Si₃N₄@Al-LLZO, the reaction propagation test was performed. In this experiment, Li granule was placed and heated on the top of Si₃N₄ coated garnet surface. Then, as shown in Figure 4.12 (b), when Li started to melt at around 190 °C, not only the Si₃N₄ coated area underneath the Li metal but also in proximity to it, started to change its color to black. This observation gave the visual assurance of the chemical reaction occurring between Li metal and interfacial Si₃N₄ layer. The reaction occurred not only

103

under Li metal surface but it also propagated around the entire Si_3N_4 coated area, emphasizing the reaction was chemically and kinetically favored.

Now, in order to visualize the impact of the lithiophilic Si_3N_4 layer at the Li/garnet interface, cross-section SEM images for bare and coated samples were taken. SEM images of coated garnet, Figure 4.12 (e, f) clearly shows the tight soldering between Li metal and Al-LLZO pellet as no gaps and voids are visible throughout the contact area. Whereas the bare garnet (Figure 4.12 (c, d)) contact with Li metal is plagued with presence of large voids and gaps suggesting poor interface. This visually validated the effectiveness of coating Si_3N_4 lithiophilic layer at the interface to promote interfacial contact of Al-LLZO grains with Li metal.

To understand the nature of chemical reaction at the interface and indicate the formation of intermediate product, XRD was performed after Li metal was infused on Si_3N_4@Al-LLZO. In this XRD analysis of Figure 4.12 (g), new peaks indicated by black-filled diamonds (♦) were observed. Also, as the sample for this XRD analysis consists of Al-LLZO substrate underneath the coated layer, the common diffraction peaks related to Al-LLZO were also observed. Further, these pronounced new peaks were indexed to lithium silicon nitride (JCPDS #40-1449), indicating the formation of tetragonal phase Li_8SiN_4 due to Li and Si_3N_4 reaction at the interface [281, 282]. The favorable kinetics for reaction between Li and Si_3N_4 to occur and formation of the ternary alloy phase Li_8SiN_4 is further verified by identifying peaks using Miller indices as reported in previous literature [283-290]. To be more specific the denoted peaks match the XRD data reported by Yamashita et al. in [291], Yamane et al. in [283], and JCPDS card # 40-1449. Similarly, studies by Yamane [283], and Ulvestad [284] et al. have analyzed the thermal promotion of reaction between Si_3N_4 and Li metal, forming different ternary lithium silicon nitride products. As in this work during processing heat was applied to infuse molten Li on Si_3N_4

layer, which further favors the occurrence of alloying reaction and formation of these ternary

phase alloys. These alloys not only ensure intimate contact at the interface but also provides Li

ion conduction tunnels as all phases of alloys formed by Li and Si_3N_4 reaction are shown to be

good Li ion conductors with phases such as Li_8SiN_4 exhibiting ionic conductivity reaching as

high as 5×10^{-2} S m^{-1} at elevated temperature of 400 K with lowest activation energy of 46 kJ

mol^{-1} [283]. The alloy formed at the Li/ Si_3N_4@Al-LLZO interface were also ionically

conductive which is apparent by the lithiophilic nature and decrease in charge transfer resistance

(from EIS measurements) when Si_3N_4 interlayer is introduced. The chemical reaction that best

describe this reduction reaction is given in equation (4.3) [284], which further explains the

conversion reaction of Si_3N_4 film with Li metal at interface resulting the formation of Li_8SiN_4

that promoted the interfacial contact.

$$n\,SiN_x + y\,Li^+ + ye^- \rightarrow na\,Li_{3.5}Si + n\,Li_bSi_{1-a}N_x + cA\,Li^{SEI} \qquad (4.3)$$
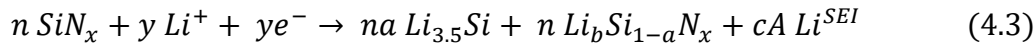
4.2.2 Electrochemical characterizations

4.2.2.1 SSE ionic conductivity analysis

To analyze the ion conduction kinetics of as prepared Al-LLZO pellets, their ionic conductivity

were calculated using EIS with Au layers sputtered as blocking electrodes. Figure 4.13 (a) shows

the Nyquist plot for EIS analysis of Al-LLZO pellets sintered at low temperature of 1100 °C. As,

in this sintering temperature the Al-LLZO crystals have not densified enough, clearly two

semicircles are visible, which indicates presence of both grain and grain boundary resistances.

Whereas the EIS spectra for Al-LLZO pellets sintered at optimized sintering temperature of 1280

°C shows mainly the bulk response with negligible grain boundary contribution, ensuring high

relative density of as sintered pellets (Figure (4.13 (c)). Similarly, Figure 4.13 (c) also shows the

EIS measurements of Al-LLZO at temperature range of 22-60 °C. It is further observed from the
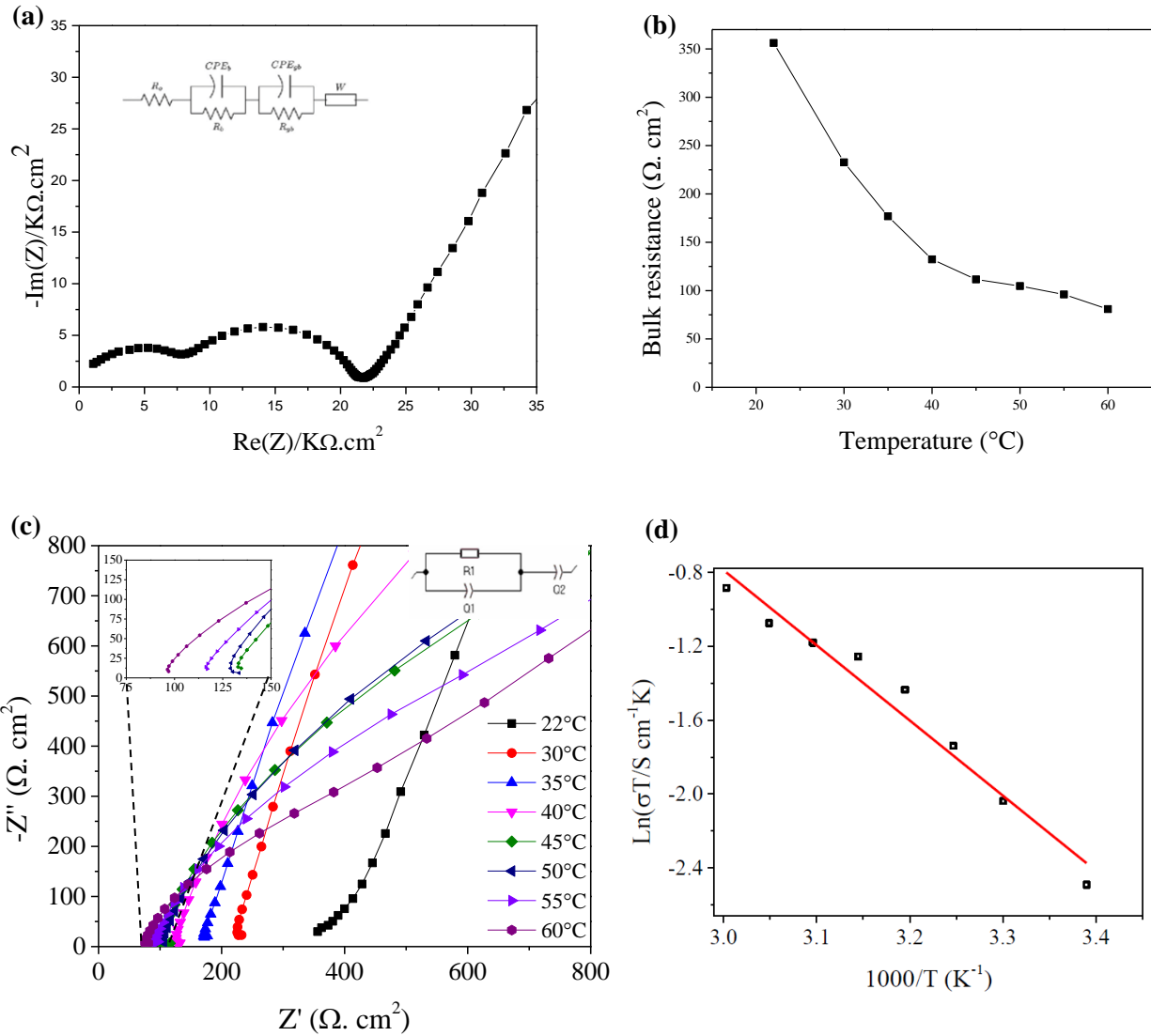
Figure 4. 13 EIS analysis of (a) garnet Al-LLZO pellets sintered at lower sintering temperature of 1100 ℃, (b) plot showing bulk resistance response to increase in temperature for Al-LLZO pellets sintered at 1280 ℃ for 1h, (c) Al-LLZO electrolyte at temperature ranging from 22-60 ℃ with inset showing spectra from 45-60 ℃; and (d) Arrhenius plot derived from ionic conductivity measurement of Al-LLZO at different temperature.

Figure 4.13 (b) that the bulk EIS response value of Al-LLZO at low-frequency intercept decreases as temperature increases from 22 to 60 °C. This follows the typical Arrhenius behavior, which is again validated by linearly fitted curve in the Arrhenius plot of Figure 4.13 (d). This fitted curve's slope gives the activation energy (E_a) for Li ion conduction calculated using Arrhenius equation (equation (2.15)). Also, the Li ion conductivity of Al-LLZO solid electrolyte pellet at 22 °C (RT) was calculated using equation 2.14. Thus, the E_a and Li ion conductivity (σ) of 0.34 eV and 2.81×10^{-4} S cm^{-1} was observed for garnet SSE, respectively.

4.2.2.2 Li symmetrical and full cell

Li symmetrical cell cycling test with different thicknesses of Si$_3$N$_4$ interfacial layer was carried out under constant current density of 0.1 mA cm^{-2} for optimizing the interlayer thickness. As shown if Figure 4.14, Si$_3$N$_4$@Al-LLZO coupled with Li metal was assembled to obtain Li symmetrical cells with Si$_3$N$_4$ thickness from 0, 20, 30 to 40 nm. The symmetrical cells with bare garnet (0 nm Si$_3$N$_4$) showed very high overpotential about $\pm$ 250 mV from the first cycle and short circuited after only 15 h of cycling time (Figure 4.14 (a)). Similarly, the cells with 20 nm thick interlayer showed stable Li plating/stripping only until 150 h, after which the overpotential
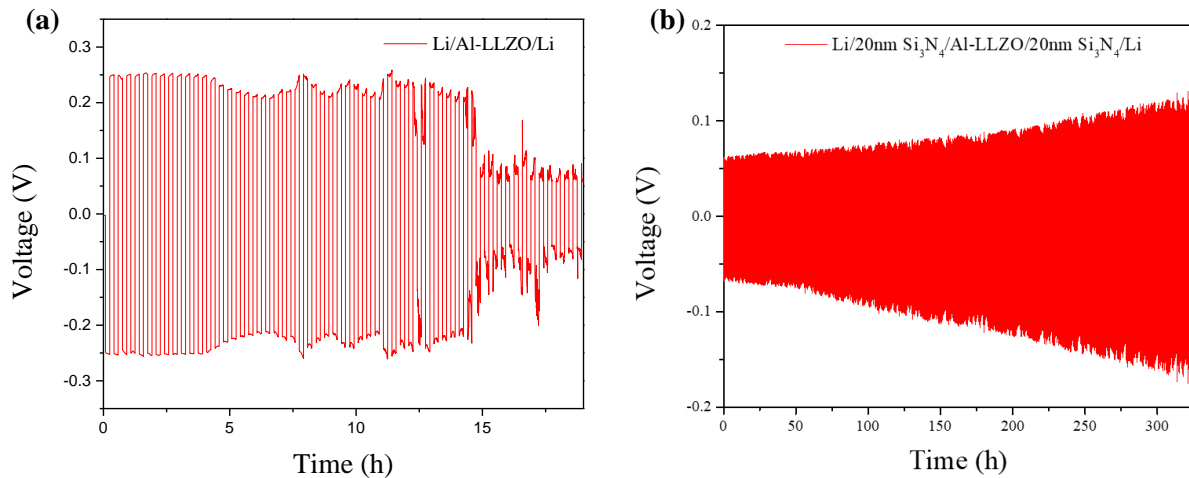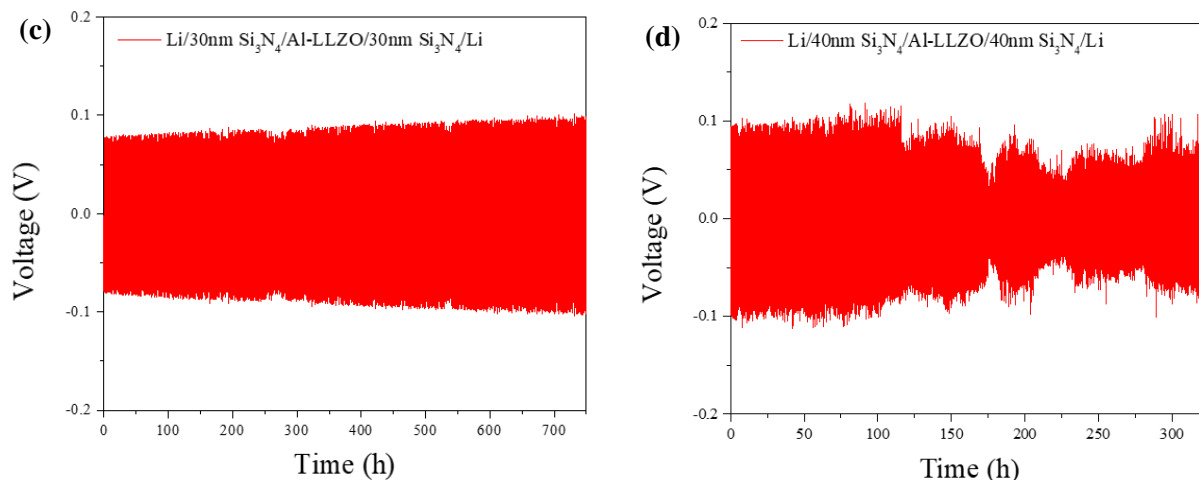
Figure 4. 14 Li symmetrical cell cycling stability tests at 0.1 mA cm^{-2} current density with different Si$_3$N$_4$ interlayer thicknesses of (a) 0 nm (bare Al-LLZO), (b) 20 nm, (c) 30 nm, and (d) 40 nm.

began to destabilize and drastically increase, eventually reaching upto $\pm$ 127 mV (Figure 4.14 (b)). While the cells with 30 nm deposited Si$_3$N$_4$ interlayer showed the superior cycling performance with stable plating/stripping and low overpotential of $\pm$ 80 mV for more than 700 h (Figure 4.14 (c)). Also, cycling of symmetrical cells assembled with 40 nm interlayer modified Al-LLZO showed increased voltage polarization and fluctuations after 100 h of Li deposition/ dissolution, indicating premature cell failure [292-295]. Thus, the thickness of Si$_3$N$_4$ interlayer was optimized to 30 nm, as it showed outstanding Li symmetrical cell cycling compared to cells assembled with other interlayer thicknesses.

Next, the effectiveness of Si$_3$N$_4$ layer in decreasing the resistance at Li/Al-LLZO interface was analyzed. Similarly, to further access the Li plating/stripping enhancement after interface modification, Li symmetrical cells were cycled at different current densities and their performance was compared with cells assembled using bare Al-LLZO.
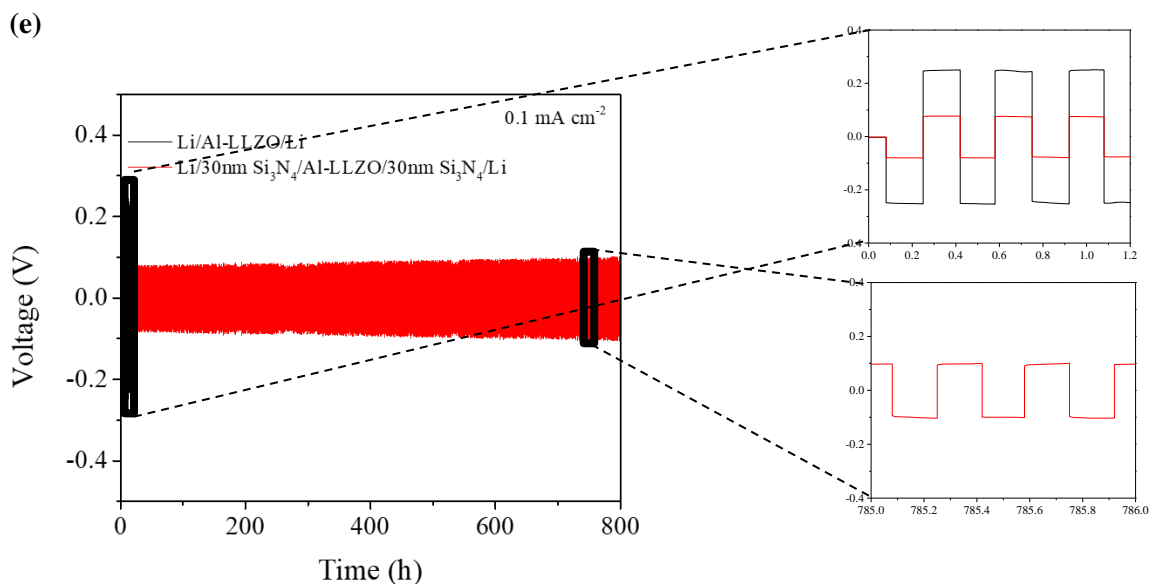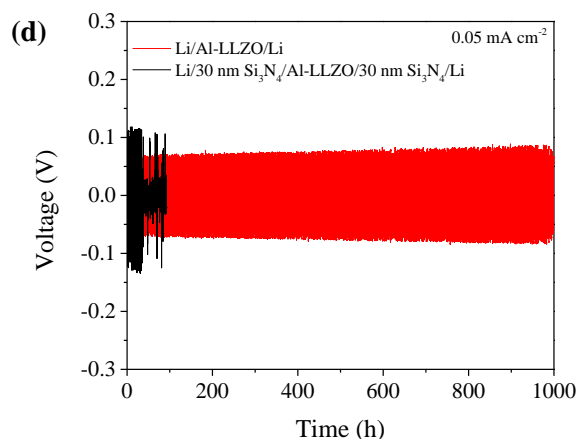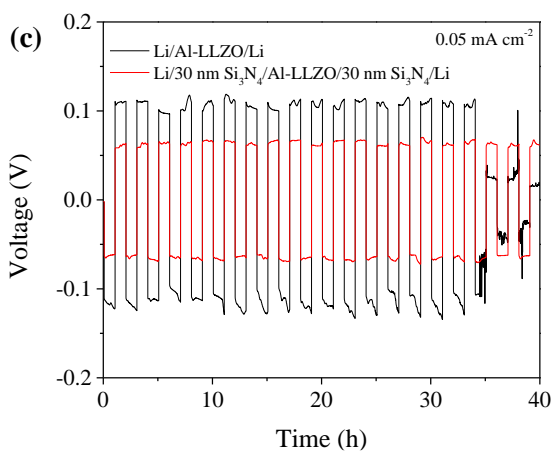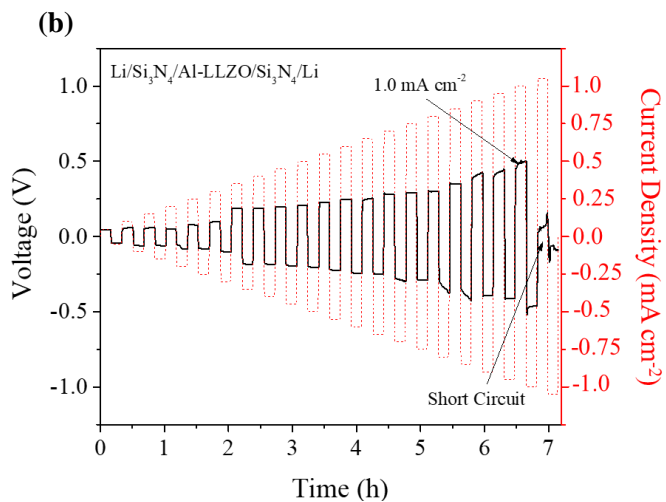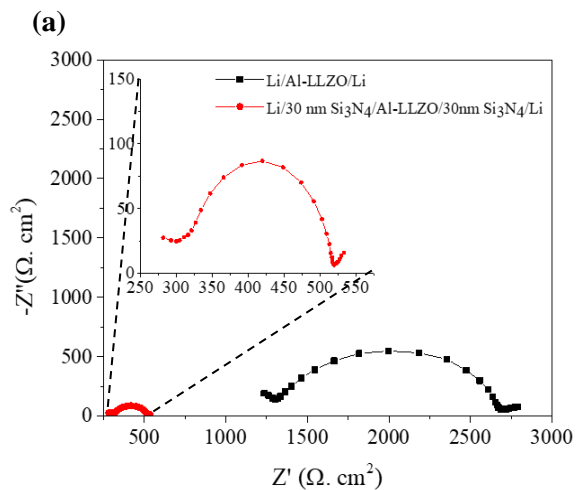
Figure 4. 15 Electrochemical stability analysis of Si_3N_4 modified Al-LLZO showing (a) Nyquist plots of Li-symmetrical cells for Al-LLZO with and without Si_3N_4 modification. (b) Critical current density (CCD) plot for Si_3N_4 modified symmetric cell. Galvanostatic cycling performance of Li symmetrical cells with and without Si_3N_4 interlayer at 0.05 mA cm^{-2}, 0.05 mAh cm^{-2} showing (c) initial few cycles and (d) long term cycling; and (e) Galvanostatic cycling performance of Si_3N_4 modified symmetric cells at constant current density of 0.1 mA cm^{-2}.

EIS measurements of Li symmetric cells with Si_3N_4 interface modification (Li/Si_3N_4/Al-LLZO/Si_3N_4/Li) and without modified interlayer (Li/Al-LLZO/Li) showed that introducing Si_3N_4 at the interface reduces the total impedance (Al-LLZO electrolyte pellet + Li/Al-LLZO interface) from 2750 Ω cm^2 for bare garnet to 525 Ω cm^2 for interlayer modified cells (Figure 4.15 (a)). The total bulk impedance of Al-LLZO was observed from EIS of Au/Al-LLZO/Au as 356 Ω cm^2 (Figure 4.13 (c)). After subtracting this bulk resistance value from the total impedance and considering interface on one side of symmetric cell, the interfacial area specific resistance (ASR) is calculated to be reduced from 1197 Ω cm^2 to 84.5 Ω cm^2. Similarly, critical current density (CCD) test for Li plating/stripping cycles were performed, which was confirmed to be 1 mA cm^{-2} for Li/Si_3N_4/Al-LLZO/Si_3N_4/Li cells (Figure 4.15 (b)). The significant reduction in interfacial ASR confirms the promotion of conformal contact between Li metal and Al-LLZO by introduction of Si_3N_4 interlayer which forms a thermally lithiated ternary phase alloy and inhibits evolution of insulating impurity layers such as Li_2CO_3, LiOH, etc. at the interface.

Galvanostatic Li plating/stripping cycling stability experiments were performed on Li symmetrical cells to examine the enhancement of Li ion conduction across the interface facilitated by Si_3N_4 interlayer modification. First, the Li symmetrical cells were cycled at low

current density of 0.05 mA cm^{-2} reaching capacity of 0.05 mAh cm^{-2} (Figure 4.15 (c, d)). The initial few cycles for this current density cycling are compared in Figure 4.15 (c), which shows that the cell with bare garnet is marred with large overpotential $> \pm$ 100 mV, whereas that with Si$_3$N$_4$ interface layer promote stable cycling and overpotential suppression to $\pm$ 60 mV. Further, when these cells were cycled for long time period, the cell with bare garnet short circuits after only 35 h, whereas that with Si$_3$N$_4$ modification showed stable cycling upto 1000 h (Figure 4.15 (d)), indicating stabilized interface enabled by interlayer introduction. Similarly, Li symmetrical cells were also tested at higher current densities of 0.1 mA cm^{-2} and 0.2 mA cm^{-2}. As shown in Figure 4.15 (e), superior cycling upto 800 h was observed at 0.1 mA cm^{-2} for Si$_3$N$_4$ modified garnet with stable voltage at $\pm$ 80 mV (inset of Figure 4.15 (e)) compared to bare garnet which only lasted for 20 h incurring excessive voltage polarization of $\pm$ 250 mV.
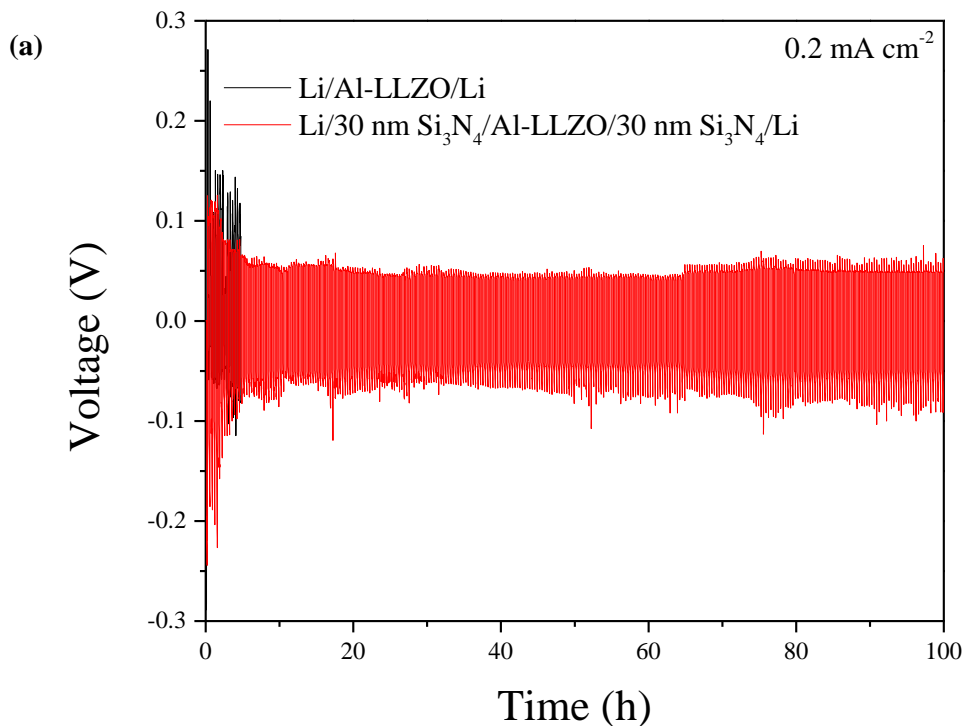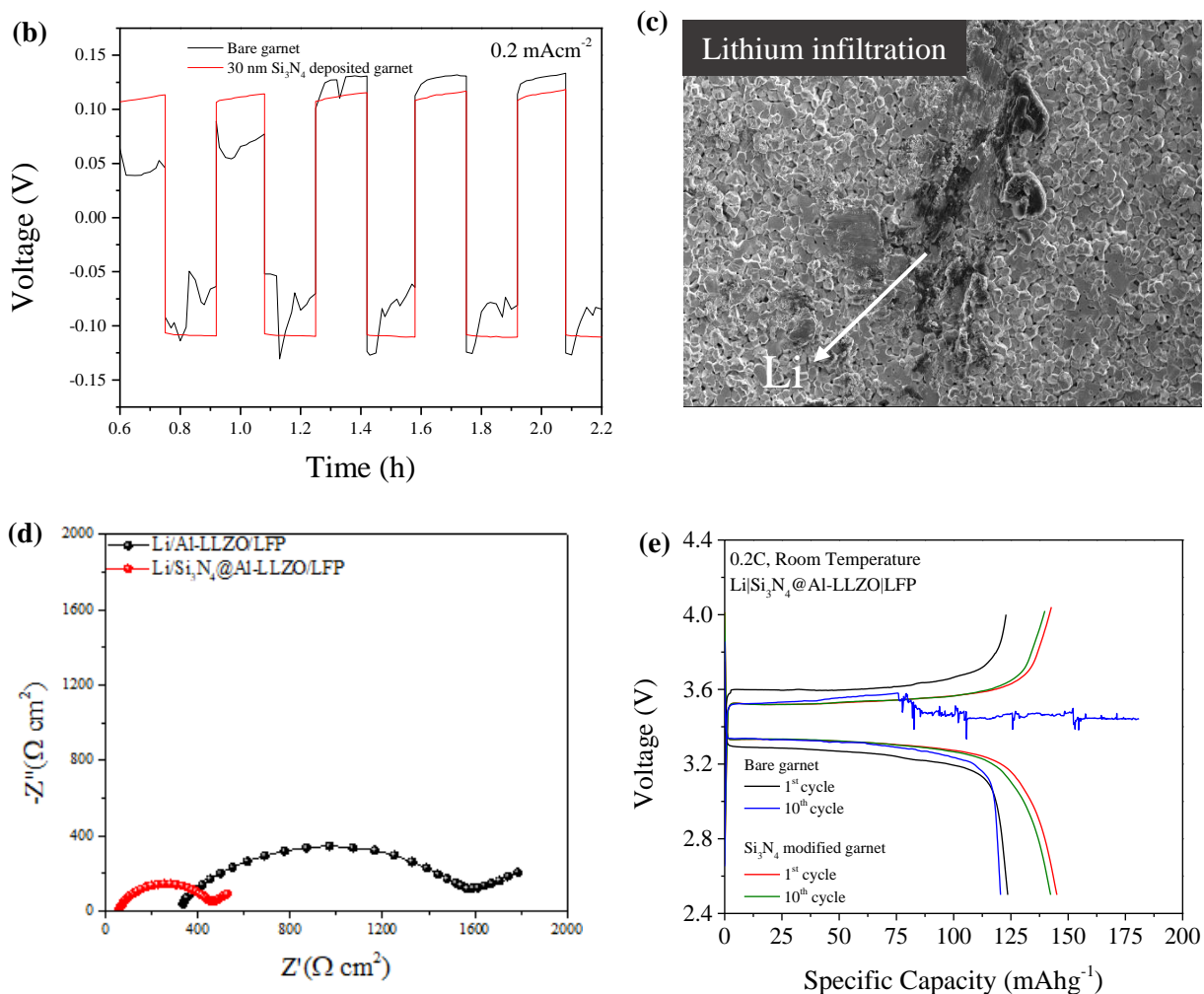
Figure 4. 16 Li symmetrical and full cell test showing (a) galvanostatic plating/stripping cycles of symmetrical cells at high current density of 0.2 mA cm^{-2}, (b) First few cycles for symmetrical cells at 0.2 mA cm^{-2}, (c) Al-LLZO cross-section SEM image of short-circuited symmetrical cell; (d) Nyquist plot of Li/LFP full cells, and (e) Li/LFP full cell cycling voltage profiles for bare and Si$_3$N$_4$ modified garnet.

When current density was further increased to 0.2 mA cm^{-2} (Figure 4.16 (a)), Li symmetrical cells with bare garnet showed unstable voltage profile with overpotential value reaching $> \pm 150$

mV. This cell was only stable for ~ 15 h, whereas the cells with Si$_3$N$_4$@Al-LLZO electrolyte

showed stable plating/stripping cycles upto 100 h with stabilized voltage of ~ $\pm$ 100 mV (Figure

4.16 (b)). However, after 100 h the cells were shorted, showing the typical mechanism of short

circuit failure in SSBs by Li growth in SSE as shown in Figure 4.16 (c). Table 4.4 shows the

comparison of Si$_3$N$_4$ interlayer performance in this work with other reported interlayers.

Table 4. 4 Performance comparison between different nitride and other interlayers at LMA/SSE

interface for reducing interfacial resistance

Material	SSE	Interlayer thickness	Interface ASR (Ω cm^2)	Operating temperature (°C)	SE thickness	Voltage Overpotential/ Current density (mV/ mAcm^{-2})	CCD (mA cm^{-2})	Method	Ref
Boron nitride	LATP with liquid electrolyte wetting	1-2 µm	3×10^4	60	0.5-1 mm	156 / 0.3	0.5	LPCVD	[296]
Lithium nitride	LLZTO	N/A	~120	40	N/A	60 / 0.1	0.2	Ebeam	[199]
Boron nitride nanosheet	PEO-based	150 nm	~100	60	~ 40 µm	100 / 0.3	0.3	Chemical exfoliation	[297]
ITO	LLZTO	40 nm	32	30	N/A	20 / 0.1	1.05	Magnetron Sputtering	[298]
Candle soot	LLZTO	1.5 µm	50	60	~ 1mm	28 / 0.1	0.6	Flame vapor deposition	[299]
PVC-TPU	LAGP	50 µm	~ 890	25	N/A	100 / 0.1	0.5	Drop casting	[300]
Silicon nitride	**Al-LLZO**	**30 nm**	**84.5**	**22**	**1 mm**	**80 / 0.1**	**1**	**RF sputtering**	**This work**

It can be observed in Table 4.4, that at RT (22°C), the Si_3N_4 interlayer modified cells shows remarkably low interfacial resistance and reduced overpotential voltage. In addition, achieving the CCD of 1 mA cm^{-2} considering the electrolyte thickness and deposition process used, this work implies Si_3N_4 as excellent interlayer that can address the interface mismatch between LMA and garnet SSE.
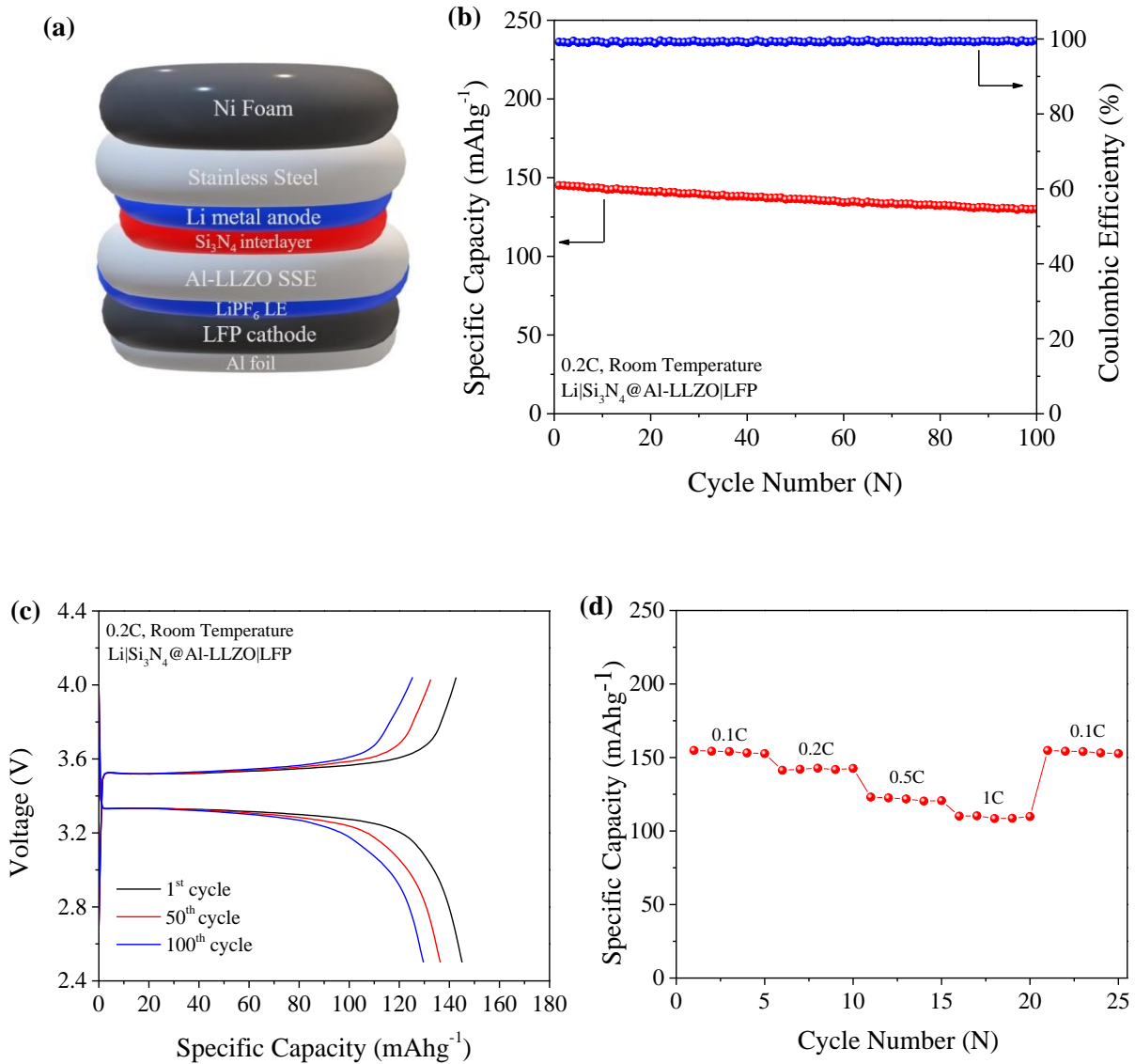
Figure 4. 17 Full cell electrochemical testing showing (a) Schematic of full cell device structure for Li/Si$_3$N$_4$@Al-LLZO/LFP cells, (b) cycling performance at 0.2 C-rate in RT, (c) Galvanostatic charge/discharge voltage profile for different cycles (1st, 50th, and 100th), and (d) Rate performance and capacity retention test at various C-rates.

In order to demonstrate the practicality of this work by enabling potential use of this technique in high energy density LMBs, the Li/Si$_3$N$_4$@Al-LLZO/LFP hybrid full cells were assembled and tested following the device design as shown in Figure 4.17 (a). In Nyquist plot obtained from EIS test shown in Figure (4.16 (d)), the total ASR for full cells with Si$_3$N$_4$@Al-LLZO was < 500 Ω cm^2, whereas that for bare garnet was ~ 1600 Ω cm^2 at RT. Similarly, when full cells were cycled at 0.2 C in RT, the cells with bare Al-LLZO displayed larger overpotential and unstable charging voltage curves within 10 cycles, suggesting short lived cycling. On the other hand, the Si$_3$N$_4$@Al-LLZO full cells showed stable and prolong charge/discharge cycling with enhanced specific capacity (Figure 4.16 (e)). Further, it is also observed that the full cells with/without Si$_3$N$_4$ interlayer delivered initial discharge capacities of 145.11/125.02 mAh g^{-1}. Figure 4.17 (b) shows the long term cycling performance of Si$_3$N$_4$@Al-LLZO full cells with initial galvanostatic charge and discharge capacities of 146.25 and 145.11 mAh g^{-1}, respectively, this is equivalent to CE of 99.2 %. After 100 cycles the cell capacity of 130 mAh g^{-1} was observed with CE maintenance ~ 100 %. The full cell with Si$_3$N$_4$@Al-LLZO electrolyte shows a well-defined and flat charge/discharge voltage plateau with minimal polarization voltage of 0.15 V observed in the voltage profiles of 1st, 50th, and 100th cycles tested at 0.2 C in RT (Figure 4.17 (c)).

The rate capability and capacity retention tests were also performed on Si_3N_4@Al-LLZO full cells in RT. As shown in Figure 4.17 (d), the cells showed discharge capacities of 153.8, 142.1, 121.7 and 109.5 mAhg^{-1} at 0.1, 0.2, 0.5 and 1C, respectively. When the C-rate was drawn back to 0.1 C, the cell showed retained capacity of 153.8 mAh g^{-1}. This accounts for 100 % retention of initial capacity after cycling the cell at higher C-rates for five cycles each. Therefore, the stable charge/discharge voltage profile, minimum voltage hysteresis, long term cycling stability, suppressed capacity fade, and excellent capacity retention facilitated by the introduction of Si_3N_4 interlayer at the Li/Al-LLZO garnet SSE interface confirms and validates the efficacy of this interlayer in establishing an intimate contact with enhanced charge transfer and low interfacial resistance. The Li wetting property of Si_3N_4 by favoring the alloy reaction when infused with molten Li, forming highly ion conductive ternary phase alloys at the interface are the grounds on which this process was developed and successfully implemented.

Chapter 5: Conclusion and Future work

5.1 Summary and significance

Advancement in two major LMB systems are successfully demonstrated in this dissertation work. First, the electrolyte additive engineering in liquid electrolyte based LMBs have enabled the suppression of dendrite growth in LMAs. Inclining towards superior nitrate anion electrochemical chemistry against Li metal and SEI layer stabilization potential of lanthanides, a novel electrolyte additive, gadolinium nitrate ($Gd(NO_3)_3$) have been introduced in ether solvent electrolyte based LMBs. The use of only 3mM of this additive have shown to tune the composition of SEI layer formed on Li metal during battery cycling. The additive's nature to initiate the sacrificial reaction with Li metal to form the SEI prior to electrolyte reduction facilitated passivation of LMA and prevented electrolyte decomposition. From chemical state analysis of SEI layer, the existence of gadolinium compounds on Li metal surface layer after activation of it on LMA was observed. The incorporation of electrolyte additive compounds into the surface layer stabilized and passivated the composite film on the Li metal surface by forbidding the formation of highly negative electrostatic fields leading to nodular morphology of Li deposition. As a result, a dendrite free LMA was obtained which showed outstanding plating/stripping properties when assembled in symmetrical and full cells. For instance, nearly 4 times increase in plating/stripping hours (h) was observed when Li symmetrical cells were cycled with use of additive in the electrolyte at 0.5 mA cm^{-2}, reaching capacity of 1 mAh cm^{-2}. Similarly, when Li symmetrical cells with electrolyte additive were cycled at high current density of 2 mA cm^{-2} and capacity 1 mAh cm^{-2}, stable cycling with voltage stabilized at $\pm$ 58 mV was obtained for 1200 h, whereas cells with no additive only lasted for 200 h with high voltage overpotential of $\pm$ 200 mV. Similarly, Li/LFP full cells with electrolyte additive

maintained 88.5 % of its initial capacity even after 400 cycles compared to 56.3 % capacity maintenance for cells without additive. Also, when charged at higher C-rates, the cells with electrolyte additive displayed an impressive capacity retention of 98.33%. Therefore, this superior cycling performance with reduced capacity fade for high cycle number validated the effectiveness of using $Gd(NO_3)_3$ as electrolyte additive. This work provides significant contribution in solving problems associated with LMBs by formulating an additive engineered electrolyte design to form stable SEI layer, promote nodular Li deposition, suppress Li dendrite growth, inhibit uncontrolled side reaction and reduce electrolyte decomposition. These findings shed light into the potential of nitrate salt-based metal cations electrolyte additives in achieving high energy density and safe LMBs.

Similarly, the second work is based on developing SSBs by using SSEs which holds promise of realizing next-generation safe energy storage devices as long as these solid electrolytes are stable in the presence of LMA and high voltage cathode. However, the practical use of these SSBs has been hindered by poor solid-solid interfaces, especially between LMA and SSE, incurring high impedance and non-uniform current density at the interface. So, the objective of this work is to tackle this hurdle by accessing interfacial engineering technique for establishing superior contact at the interface that facilitates low interfacial charge transfer resistance and enhanced battery cycling performance. Thus, a facile and effective process of depositing silicon nitride (Si_3N_4) interlayer was introduced in this work to address the interfacial mismatch issue between LMA and garnet Al-LLZO SSE. The RF sputtered Si_3N_4 nanolayer on the Al-LLZO garnet SSE (Si_3N_4@AL-LLZO) exhibited a highly lithiophilic behavior evidenced by excellent wetting of Li metal on its surface. This interlayer promoted the alloying reaction with Li metal to form a highly Li ion conductive ternary phase alloy, Li_8SiN_4 on the Li/Al-LLZO garnet interface. The

ion conductive nature of thermally lithiated intermediate alloy formed at the interface was confirmed by the significant reduction of interfacial ASR from 1197 Ω cm^2 to 84.5 Ω cm^2 for Li ion conduction. This was also attributed to formation of smooth interface with inhibition of impurity layers (e.g., Li_2CO_3, LiOH) evolution. Further, the interlayer deposited Si_3N_4@Al-LLZO SSEs was assembled into Li symmetrical solid-state cells and hybrid full cells, and their electrochemical performance was compared with cells using bare garnet. The Li symmetrical cells with Si_3N_4@ Al-LLZO cycled at low current density of 0.05 mA cm^{-2} showed stable plating/stripping cycles for 1000 h compared to bare garnet cells that short circuited after only 35 h. This indicated the interface was stabilized during cycling by introduction of Si_3N_4 interlayer. When current density was increased to 0.1 and 0.2 mA cm^{-2}, still superior cycling was observed for symmetrical cells with Si_3N_4@ Al-LLZO, showing stabilized voltage and longer cycle time compared to cells with bare garnet. Further, when the interface engineered SSE were employed in practical LFP/Li batteries, the first discharge capacity of 145.11 mAh g^{-1} was obtained compared to only 125.02 mAh g^{-1} for bare garnet full cells. Also, the Si_3N_4 interface engineered cells maintained the cell capacity of 130 mAh g^{-1} after 100 cycles with ~ 100 % CE, whereas the bare garnet cells were unstable after 10 charge/discharge cycles. This shows the efficacy of process of depositing these interlayers to homogenize the Li/SSE interface contact and enhance the interfacial Li ion transport with low resistance. The introduction of Si_3N_4 at the interface promotes the formation of lithiophilic interface, facilitating alloying reaction to form Li ion conductive phase alloys, which in turn contributes to development of intimate and conformal contact, both physical and chemical, between garnet type SSE and Li metal. The findings from this work provides important insights into significance of engineered interfaces for solving solid-solid interfacial mismatch eventually for developing energy dense and safe solid-state LMBs.

5.2 Future work

To further widen the extensiveness of this dissertation work, some of the suggested future works are essential which can prove vital under circumstances such as mass manufacture and product commercialization of LMBs.

For the work of functional electrolyte additive engineering, computer simulations using algorithms such as first principal density functional theory (DFT) can be implemented to further understand the formation and effect of SEI layer on LMA when additives are used. The simulations can provide wide variety of information on Li transport on SEI layer, electrostatic field development in Li surface due to SEI layer, Li deposition behavior on LMA, etc. without exploiting large quantity of resources. Similarly, these powerful tools can also be used to predict new electrolyte additive materials by analyzing their effect on LMA which can open whole new avenues in LMB research. Also, the electrolyte additives can show a major role in changing the local environment and solvation shells of Li cations in the electrolyte which is needed to be deciphered in order to fully understand their effect on Li deposition. Advanced characterization tools such as nuclear magnetic resonance (NMR) can be used to further understand the solvation sheath and desolvation behavior of Li ion during Li deposition.

Secondly, for the work on LMA/SSE interface engineering, although use of SSE in LMBs can solve safety issues associated with LE, the major remodeling is required in manufacture of this SSE to compete with 20 µm thin polymer separators currently in market for use in LIBs. Although great efforts have been made recently in the development of SSE materials with high Li ion conductivity, the material chemistry analysis are drawn mostly from thick bulky ceramic pellets. The performance of thus assembled SSBs is limited by these thick solid electrolytes and not only by high impedance at the electrode/electrolyte impedance. So, to compete with ~ 20 µm

thick polymer separators used in current LIBs, the ceramic solid electrolyte manufacturing techniques needs a major revolution. Therefore, to obtain these thin SSEs, advanced techniques such as co-sputtering deposition, wet-chemical thin film coating, chemical vapor deposition, etc. should be investigated. The development of SSE thin film coating techniques that well aligns with current manufacturing method for LIBs can also facilitate lean manufacturing of pouch type SSBs.

Furthermore, as the electrochemical characteristics in this dissertation are tested using coin cell design which is reasonable for proof of concept and foundational study. These techniques and inventions should be employed to fabricate pouch cell type batteries in future providing more commercial and practical conditions. Similarly, extreme condition testing experiments such as wide temperature range tests, bending and puncture tests, extreme fast charging conditions, etc. should be investigated in order to ensure safe operation and meet commercialization goals.

References

1.   Ali, A., *Natural resources depletion, renewable energy consumption and environmental degradation: a comparative analysis of developed and developing world.* 670216917, 2021.

2.   Lindsey, R. and L. Dahlman, *Climate change: Global temperature.* Available online: climate. gov (accessed on 22 March 2021), 2020.

3.   Trigg, T., et al., *Global EV outlook: understanding the electric vehicle landscape to 2020.* Int. Energy Agency, 2013. **1**: p. 1-40.

4.   Cozzi, L., et al., *World Energy Outlook 2020.* vol, 2020. **2050**: p. 1-461.

5.   Andrew, R.M., *Towards near real-time, monthly fossil CO2 emissions estimates for the European Union with current-year projections.* Atmospheric pollution research, 2021. **12**(12): p. 101229.

6.   Zhongming, Z., et al., *EIA projects nearly 50% increase in world energy use by 2050, led by growth in renewables.* 2021.

7.   Yang, Z., et al., *Electrochemical energy storage for green grid.* Chemical reviews, 2011. **111**(5): p. 3577-3613.

8.   Gurung, A. and Q. Qiao, *Solar charging batteries: advances, challenges, and opportunities.* Joule, 2018. **2**(7): p. 1217-1230.

9.   Adhamash, E., et al., *Gamma-radiated biochar carbon for improved supercapacitor performance.* RSC advances, 2020. **10**(50): p. 29910-29917.

10.   Adhamash, E., et al., *High-energy plasma activation of renewable carbon for enhanced capacitive performance of supercapacitor electrode.* Electrochimica Acta, 2020. **362**: p. 137148.

11.	Pathak, R., et al., *Advances in conversion-type Li-metal fluoride battery: a mini-review.* 2019.

12.	Zhao, Z., et al., *Sulfiphilic FeP/rGO as a highly efficient sulfur host for propelling redox kinetics toward stable lithium-sulfur battery.* Electrochimica Acta, 2020. **364**: p. 137117.

13.	Pokharel, J., et al., *MOF-derived hierarchical carbon network as an extremely-high-performance supercapacitor electrode.* Electrochimica Acta, 2021. **394**: p. 139058.

14.	Gurung, A., et al., *Rear-Illuminated Perovskite Photorechargeable Lithium Battery.* Advanced Functional Materials, 2020. **30**(30): p. 2001865.

15.	Enos, D.G., *Lead-Acid Batteries and Advanced Lead-Carbon Batteries*. 2014, Sandia National Lab.(SNL-NM), Albuquerque, NM (United States).

16.	May, G.J., A. Davidson, and B. Monahov, *Lead batteries for utility energy storage: A review.* Journal of energy storage, 2018. **15**: p. 145-157.

17.	Whittingham, M.S., *Electrical energy storage and intercalation chemistry.* Science, 1976. **192**(4244): p. 1126-1127.

18.	Goodenough, J.B., *How we made the Li-ion rechargeable battery.* Nature Electronics, 2018. **1**(3): p. 204-204.

19.	Yoshino, A., *The birth of the lithium-ion battery.* Angewandte Chemie International Edition, 2012. **51**(24): p. 5798-5800.

20.	Wakita, S. and I. Okae, *Lithium ion battery*. 2008, Google Patents.

21.	Ramanan, A., *Nobel Prize in Chemistry 2019.* Resonance, 2019. **24**(12): p. 1381-1395.

22.	Xu, K., *A long journey of lithium: from the big bang to our smartphones.* Energy & Environmental Materials, 2019. **2**(4): p. 229-233.

23.   Wu, H. and Y. Cui, *Designing nanostructured Si anodes for high energy lithium ion batteries.* Nano today, 2012. **7**(5): p. 414-429.

24.   Gurung, A., et al., *Tin selenide–multi-walled carbon nanotubes hybrid anodes for high performance lithium-ion batteries.* Electrochimica Acta, 2016. **211**: p. 720-725.

25.   Zhang, W.-J., *A review of the electrochemical performance of alloy anodes for lithium-ion batteries.* Journal of Power Sources, 2011. **196**(1): p. 13-24.

26.   Chan, C.K., et al., *High-performance lithium battery anodes using silicon nanowires.* Nature nanotechnology, 2008. **3**(1): p. 31-35.

27.   Su, X., et al., *Silicon-based nanomaterials for lithium-ion batteries: a review.* Advanced Energy Materials, 2014. **4**(1): p. 1300882.

28.   Li, P., et al., *Recent progress on silicon-based anode materials for practical lithium-ion battery applications.* Energy Storage Materials, 2018. **15**: p. 422-446.

29.   Shen, X., et al., *Research progress on silicon/carbon composite anode materials for lithium-ion battery.* Journal of Energy Chemistry, 2018. **27**(4): p. 1067-1090.

30.   Zhang, M., et al., *Latest development of nanostructured Si/C materials for lithium anode studies and applications.* Energy Storage Materials, 2016. **4**: p. 1-14.

31.   Zuo, X., et al., *Silicon based lithium-ion battery anodes: A chronicle perspective review.* Nano Energy, 2017. **31**: p. 113-143.

32.   Sun, Y., N. Liu, and Y. Cui, *Promises and challenges of nanomaterials for lithium-based rechargeable batteries.* Nature Energy, 2016. **1**(7): p. 1-12.

33.   Xu, W., et al., *Lithium metal anodes for rechargeable batteries.* Energy & Environmental Science, 2014. **7**(2): p. 513-537.

34. Lin, D., Y. Liu, and Y. Cui, *Reviving the lithium metal anode for high-energy batteries.* Nature nanotechnology, 2017. **12**(3): p. 194-206.

35. Bruce, P.G., et al., *Li–O2 and Li–S batteries with high energy storage.* Nature materials, 2012. **11**(1): p. 19-29.

36. Andre, D., et al., *Future generations of cathode materials: an automotive industry perspective.* Journal of Materials Chemistry A, 2015. **3**(13): p. 6709-6732.

37. Liu, J., et al. *Directions of High Energy Batteries and Status of Battery500 Consortium.* in *ECS Meeting Abstracts.* 2020. IOP Publishing.

38. Cohen, Y.S., Y. Cohen, and D. Aurbach, *Micromorphological studies of lithium electrodes in alkyl carbonate solutions using in situ atomic force microscopy.* The Journal of Physical Chemistry B, 2000. **104**(51): p. 12282-12291.

39. Frenck, L., et al., *Factors that control the formation of dendrites and other morphologies on lithium metal anodes.* Frontiers in Energy Research, 2019. **7**: p. 115.

40. Li, J., et al., *Strategies to anode protection in lithium metal battery: a review.* InfoMat, 2021. **3**(12): p. 1333-1363.

41. Cheng, X.-B., et al., *Toward safe lithium metal anode in rechargeable batteries: a review.* Chemical reviews, 2017. **117**(15): p. 10403-10473.

42. Li, S., et al., *Developing high-performance lithium metal anode in liquid electrolytes: challenges and progress.* Advanced Materials, 2018. **30**(17): p. 1706375.

43. Yang, H., et al., *Recent progress and perspective on lithium metal anode protection.* Energy Storage Materials, 2018. **14**: p. 199-221.

44. Lang, J., et al., *High performance lithium metal anode: progress and prospects.* Energy Storage Materials, 2017. **7**: p. 115-129.

45.   Chen, K., et al., *Flower-shaped lithium nitride as a protective layer via facile plasma activation for stable lithium metal anodes.* Energy Storage Materials, 2019. **18**: p. 389-396.

46.   Chen, K., et al., *A copper-clad lithiophilic current collector for dendrite-free lithium metal anodes.* Journal of Materials Chemistry A, 2020. **8**(4): p. 1911-1919.

47.   Ji, X., et al., *Solid-State Electrolyte Design for Lithium Dendrite Suppression.* Advanced Materials, 2020. **32**(46): p. 2002741.

48.   Xiao, J., *How lithium dendrites form in liquid batteries.* Science, 2019. **366**(6464): p. 426-427.

49.   Guo, W., et al., *Mixed Ion and Electron-Conducting Scaffolds for High-Rate Lithium Metal Anodes.* Advanced Energy Materials, 2019. **9**(20): p. 1900193.

50.   Ghazi, Z.A., et al., *Key aspects of lithium metal anodes for lithium metal batteries.* Small, 2019. **15**(32): p. 1900687.

51.   Ye, L., et al., *Cu coated soft fabric as anode for lithium metal batteries.* Energy Storage Materials, 2020. **26**: p. 371-377.

52.   Pathak, R., et al., *Advanced strategies for the development of porous carbon as a Li host/current collector for lithium metal batteries.* Energy Storage Materials, 2021. **41**: p. 448-465.

53.   Jeong, H., J. Jang, and C. Jo, *A Review on Current Collector Coating Methods for Next-generation Batteries.* Chemical Engineering Journal, 2022: p. 136860.

54.   Issatayev, N., et al., *Three-dimensional foam-type current collectors for rechargeable batteries: A short review.* Journal of Power Sources Advances, 2021. **10**: p. 100065.

55.   Yang, C.-P., et al., *Accommodating lithium into 3D current collectors with a submicron skeleton towards long-life lithium metal anodes.* Nature communications, 2015. **6**(1): p. 1-9.

56.   Bard, A.J., L.R. Faulkner, and H.S. White, *Electrochemical methods: fundamentals and applications.* 2022: John Wiley & Sons.

57.   Li, Q., S. Zhu, and Y. Lu, *3D porous Cu current collector/Li-metal composite anode for stable lithium-metal batteries.* Advanced Functional Materials, 2017. **27**(18): p. 1606422.

58.   Yun, Q., et al., *Chemical dealloying derived 3D porous current collector for Li metal anodes.* Advanced Materials, 2016. **28**(32): p. 6932-6939.

59.   Zhang, R., et al., *N-doped graphene modified 3D porous Cu current collector toward microscale homogeneous Li deposition for Li metal anodes.* Advanced Energy Materials, 2018. **8**(23): p. 1800914.

60.   Huang, G., et al., *In situ constructing lithiophilic NiFx nanosheets on Ni foam current collector for stable lithium metal anode via a succinct fluorination strategy.* Chemical Engineering Journal, 2020. **395**: p. 125122.

61.   Hou, G., et al., *Growth direction control of lithium dendrites in a heterogeneous lithiophilic host for ultra-safe lithium metal batteries.* Journal of Power Sources, 2019. **416**: p. 141-147.

62.   Hou, Z., et al., *Lithiophilic Ag nanoparticle layer on Cu current collector toward stable Li metal anode.* ACS applied materials & interfaces, 2019. **11**(8): p. 8148-8154.

63.   Wang, J.-r., et al., *A lithiophilic 3D conductive skeleton for high performance Li metal battery.* ACS Applied Energy Materials, 2020. **3**(8): p. 7265-7271.

64.   Sun, C., et al., *ZnO nanoarray-modified nickel foam as a lithiophilic skeleton to regulate lithium deposition for lithium-metal batteries.* Journal of Materials Chemistry A, 2019. **7**(13): p. 7752-7759.

65.   Hou, G., et al., *Dendrite-free Li metal anode enabled by a 3D free-standing lithiophilic nitrogen-enriched carbon sponge.* Journal of Power Sources, 2018. **386**: p. 77-84.

66.   Peled, E., *The electrochemical behavior of alkali and alkaline earth metals in nonaqueous battery systems—the solid electrolyte interphase model.* Journal of The Electrochemical Society, 1979. **126**(12): p. 2047.

67.   Peled, E., D. Golodnitsky, and G. Ardel, *Advanced model for solid electrolyte interphase electrodes in liquid and polymer electrolytes.* Journal of the Electrochemical Society, 1997. **144**(8): p. L208.

68.   Aurbach, D., et al., *Identification of surface films formed on lithium in propylene carbonate solutions.* Journal of The Electrochemical Society, 1987. **134**(7): p. 1611.

69.   Aurbach, D., Y. Ein-Ely, and A. Zaban, *The surface chemistry of lithium electrodes in alkyl carbonate solutions.* Journal of the Electrochemical Society, 1994. **141**(1): p. L1.

70.   Xu, K., *Nonaqueous liquid electrolytes for lithium-based rechargeable batteries.* Chemical reviews, 2004. **104**(10): p. 4303-4418.

71.   Fong, R., U. Von Sacken, and J.R. Dahn, *Studies of lithium intercalation into carbons using nonaqueous electrochemical cells.* Journal of The Electrochemical Society, 1990. **137**(7): p. 2009.

72.   Aurbach, D., *Review of selected electrode–solution interactions which determine the performance of Li and Li ion batteries.* Journal of Power Sources, 2000. **89**(2): p. 206-218.

73.   Ma, C., F. Xu, and T. Song, *Dual-Layered Interfacial Evolution of Lithium Metal Anode: SEI Analysis via TOF-SIMS Technology.* ACS Applied Materials & Interfaces, 2022. **14**(17): p. 20197-20207.

74.   He, D., et al., *Recent Advances in Solid-Electrolyte Interphase for Li Metal Anode.* Frontiers in Chemistry, 2022. **10**.

75.   Yu, Z., Y. Cui, and Z. Bao, *Design principles of artificial solid electrolyte interphases for lithium-metal anodes.* Cell Reports Physical Science, 2020. **1**(7): p. 100119.

76.   Zhang, H., et al., *Lithiophilic-lithiophobic gradient interfacial layer for a highly stable lithium metal anode.* Nature communications, 2018. **9**(1): p. 1-11.

77.   Pathak, R., et al., *Ultrathin bilayer of graphite/SiO2 as solid interface for reviving Li metal anode.* Advanced Energy Materials, 2019. **9**(36): p. 1901486.

78.   Kazyak, E., K.N. Wood, and N.P. Dasgupta, *Improved cycle life and stability of lithium metal anodes through ultrathin atomic layer deposition surface treatments.* Chemistry of Materials, 2015. **27**(18): p. 6457-6462.

79.   Kozen, A.C., et al., *Next-generation lithium metal anode engineering via atomic layer deposition.* ACS nano, 2015. **9**(6): p. 5884-5892.

80.   Wang, L., et al., *Long lifespan lithium metal anodes enabled by Al2O3 sputter coating.* Energy Storage Materials, 2018. **10**: p. 16-23.

81.   Pan, J., Y.-T. Cheng, and Y. Qi, *General method to predict voltage-dependent ionic conduction in a solid electrolyte coating on electrodes.* Physical Review B, 2015. **91**(13): p. 134116.

82.   Lu, Y., Z. Tu, and L.A. Archer, *Stable lithium electrodeposition in liquid and nanoporous solid electrolytes.* Nature materials, 2014. **13**(10): p. 961-969.

83. Yuan, Y., et al., *Regulating Li deposition by constructing LiF-rich host for dendrite-free lithium metal anode.* Energy Storage Materials, 2019. **16**: p. 411-418.

84. Zhang, X.Q., et al., *Fluoroethylene carbonate additives to render uniform Li deposits in lithium metal batteries.* Advanced Functional Materials, 2017. **27**(10): p. 1605989.

85. Choudhury, S., et al., *Electroless formation of hybrid lithium anodes for fast interfacial ion transport.* Angewandte Chemie International Edition, 2017. **56**(42): p. 13070-13077.

86. Liang, X., et al., *A facile surface chemistry route to a stabilized lithium metal anode.* Nature Energy, 2017. **2**(9): p. 1-7.

87. Yan, K., et al., *Selective deposition and stable encapsulation of lithium through heterogeneous seeded growth.* Nature Energy, 2016. **1**(3): p. 1-8.

88. Pathak, R., et al., *Fluorinated hybrid solid-electrolyte-interphase for dendrite-free lithium deposition.* Nature communications, 2020. **11**(1): p. 1-10.

89. Zheng, Y., et al., *High Performance Li Metal Anode Enabled by Robust Covalent Triazine Framework-Based Protective Layer.* Advanced Functional Materials, 2021. **31**(6): p. 2006159.

90. Wu, J., et al., *Polycationic polymer layer for air-stable and dendrite-free Li metal anodes in carbonate electrolytes.* Advanced Materials, 2021. **33**(12): p. 2007428.

91. Wang, Q., et al., *Rigid and Flexible SEI Layer Formed Over a Cross-Linked Polymer for Enhanced Ultrathin Li Metal Anode Performance.* Advanced Energy Materials, 2022: p. 2103972.

92. Li, N.W., et al., *A flexible solid electrolyte interphase layer for long-life lithium metal anodes.* Angewandte Chemie International Edition, 2018. **57**(6): p. 1505-1509.

93.   Chen, D., et al., *In situ preparation of thin and rigid COF film on Li anode as artificial solid electrolyte interphase layer resisting Li dendrite puncture.* Advanced Functional Materials, 2020. **30**(7): p. 1907717.

94.   Ma, Y., et al., *Enabling reliable lithium metal batteries by a bifunctional anionic electrolyte additive.* Energy Storage Materials, 2018. **11**: p. 197-204.

95.   Qian, Y., et al., *How electrolyte additives work in Li-ion batteries.* Energy storage materials, 2019. **20**: p. 208-215.

96.   Fu, J., et al., *Lithium nitrate regulated sulfone electrolytes for lithium metal batteries.* Angewandte Chemie, 2020. **132**(49): p. 22378-22385.

97.   Zheng, J., et al., *Electrolyte additive enabled fast charging and stable cycling lithium metal batteries.* Nature Energy, 2017. **2**(3): p. 1-8.

98.   Wahyudi, W., et al., *Lithium-Ion Desolvation Induced by Nitrate Additives Reveals New Insights into High Performance Lithium Batteries.* Advanced Functional Materials, 2021: p. 2101593.

99.   Qian, J., et al., *High rate and stable cycling of lithium metal anode.* Nature communications, 2015. **6**(1): p. 1-9.

100.   Yamada, Y., et al., *Advances and issues in developing salt-concentrated battery electrolytes.* Nature Energy, 2019. **4**(4): p. 269-280.

101.   Adams, B.D., et al., *Long term stability of Li-S batteries using high concentration lithium nitrate electrolytes.* Nano Energy, 2017. **40**: p. 607-617.

102.   Beyene, T.T., et al., *Concentrated dual-salt electrolyte to stabilize Li metal and increase cycle life of anode free Li-metal batteries.* Journal of The Electrochemical Society, 2019. **166**(8): p. A1501.

103.   Weber, R., et al., *Long cycle life and dendrite-free lithium morphology in anode-free lithium pouch cells enabled by a dual-salt liquid electrolyte.* Nature Energy, 2019. **4**(8): p. 683-689.

104.   Xue, W., et al., *FSI-inspired solvent and "full fluorosulfonyl" electrolyte for 4 V class lithium-metal batteries.* Energy & Environmental Science, 2020. **13**(1): p. 212-220.

105.   Lin, S. and J. Zhao, *Functional Electrolyte of Fluorinated Ether and Ester for Stabilizing Both 4.5 V LiCoO2 Cathode and Lithium Metal Anode.* ACS Applied Materials & Interfaces, 2020. **12**(7): p. 8316-8323.

106.   Xie, Z., et al., *Fluoropyridine family: Bifunction as electrolyte solvent and additive to achieve dendrites-free lithium metal batteries.* Journal of Materials Science & Technology, 2021. **74**: p. 119-127.

107.   Yamada, Y., et al., *Hydrate-melt electrolytes for high-energy-density aqueous batteries.* Nature Energy, 2016. **1**(10): p. 1-9.

108.   Younesi, R., et al., *The SEI layer formed on lithium metal in the presence of oxygen: A seldom considered component in the development of the Li–O2 battery.* Journal of Power Sources, 2013. **225**: p. 40-45.

109.   Zheng, J., et al., *Ionic liquid-enhanced solid state electrolyte interface (SEI) for lithium–sulfur batteries.* Journal of Materials chemistry A, 2013. **1**(29): p. 8464-8470.

110.   Woo, J.-J., et al., *Symmetrical impedance study on inactivation induced degradation of lithium electrodes for batteries beyond lithium-ion.* Journal of the Electrochemical Society, 2014. **161**(5): p. A827.

111. Doi, T., et al., *Dilution of highly concentrated LiBF4/propylene carbonate electrolyte solution with fluoroalkyl ethers for 5-V LiNi0. 5Mn1. 5O4 positive electrodes.* Journal of The Electrochemical Society, 2017. **164**(1): p. A6412.

112. Zeng, Z., et al., *Non-flammable electrolytes with high salt-to-solvent ratios for Li-ion and Li-metal batteries.* Nature Energy, 2018. **3**(8): p. 674-681.

113. Yan, C., et al., *Lithium nitrate solvation chemistry in carbonate electrolyte sustains high-voltage lithium metal batteries.* Angewandte Chemie, 2018. **130**(43): p. 14251-14255.

114. Yan, C., et al., *Dual-layered film protected lithium metal anode to enable dendrite-free lithium deposition.* Advanced Materials, 2018. **30**(25): p. 1707629.

115. Trinh, N.D., et al., *An artificial lithium protective layer that enables the use of acetonitrile-based electrolytes in lithium metal batteries.* Angewandte Chemie International Edition, 2018. **57**(18): p. 5072-5075.

116. Sun, Y., et al., *A novel organic "Polyurea" thin film for ultralong-life lithium-metal anodes via molecular-layer deposition.* Advanced Materials, 2019. **31**(4): p. 1806541.

117. Xu, X., et al., *Robust pitaya-structured pyrite as high energy density cathode for high-rate lithium batteries.* ACS nano, 2017. **11**(9): p. 9033-9040.

118. Wood, K.N., M. Noked, and N.P. Dasgupta, *Lithium metal anodes: toward an improved understanding of coupled morphological, electrochemical, and mechanical behavior.* ACS Energy Letters, 2017. **2**(3): p. 664-672.

119. Liu, Y., et al., *An artificial solid electrolyte interphase with high Li-ion conductivity, mechanical strength, and flexibility for stable lithium metal anodes.* Advanced Materials, 2017. **29**(10): p. 1605531.

120.	Fang, C., X. Wang, and Y.S. Meng, *Key issues hindering a practical lithium-metal anode.* Trends in Chemistry, 2019. **1**(2): p. 152-158.

121.	Pranay Reddy, K., et al., *Improved Li–Metal Cycling Performance in High Concentrated Electrolytes for Li-O2 Batteries.* ChemElectroChem, 2018. **5**(19): p. 2758-2766.

122.	Jiao, S., et al., *Stable cycling of high-voltage lithium metal batteries in ether electrolytes.* Nature Energy, 2018. **3**(9): p. 739-746.

123.	Alvarado, J., et al., *Bisalt ether electrolytes: a pathway towards lithium metal batteries with Ni-rich cathodes.* Energy & Environmental Science, 2019. **12**(2): p. 780-794.

124.	Zheng, J., et al., *High-fluorinated electrolytes for Li–S batteries.* Advanced energy materials, 2019. **9**(16): p. 1803774.

125.	Li, L., et al., *Self-heating–induced healing of lithium dendrites.* Science, 2018. **359**(6383): p. 1513-1516.

126.	Fan, X., et al., *Highly fluorinated interphases enable high-voltage Li-metal batteries.* Chem, 2018. **4**(1): p. 174-185.

127.	Ren, X., et al., *Localized high-concentration sulfone electrolytes for high-efficiency lithium-metal batteries.* Chem, 2018. **4**(8): p. 1877-1892.

128.	Chen, S., et al., *High-voltage lithium-metal batteries enabled by localized high-concentration electrolytes.* Advanced materials, 2018. **30**(21): p. 1706102.

129.	Yamada, Y. and A. Yamada, *Superconcentrated electrolytes for lithium batteries.* Journal of The Electrochemical Society, 2015. **162**(14): p. A2406.

130.	Zheng, J., et al., *Highly stable operation of lithium metal batteries enabled by the formation of a transient high-concentration electrolyte layer.* Advanced Energy Materials, 2016. **6**(8): p. 1502151.

131. Fan, X., et al., *Non-flammable electrolyte enables Li-metal batteries with aggressive cathode chemistries.* Nature nanotechnology, 2018. **13**(8): p. 715-722.

132. Li, W., et al., *The synergetic effect of lithium polysulfide and lithium nitrate to prevent lithium dendrite growth.* Nature communications, 2015. **6**(1): p. 1-8.

133. Rosenman, A., et al., *The effect of interactions and reduction products of LiNO3, the anti-shuttle agent, in Li-S battery systems.* Journal of The Electrochemical Society, 2015. **162**(3): p. A470.

134. Liu, S., G.-R. Li, and X.-P. Gao, *Lanthanum nitrate as electrolyte additive to stabilize the surface morphology of lithium anode for lithium–sulfur battery.* ACS applied materials & interfaces, 2016. **8**(12): p. 7783-7789.

135. Cao, R., et al., *Anodes for rechargeable lithium-sulfur batteries.* Advanced Energy Materials, 2015. **5**(16): p. 1402273.

136. Jia, W., et al., *Extremely accessible potassium nitrate (KNO3) as the highly efficient electrolyte additive in lithium battery.* ACS applied materials & interfaces, 2016. **8**(24): p. 15399-15405.

137. Lin, Z., et al., *Phosphorous pentasulfide as a novel additive for high-performance lithium-sulfur batteries.* Advanced Functional Materials, 2013. **23**(8): p. 1064-1069.

138. Wu, F., et al., *Lithium iodide as a promising electrolyte additive for lithium–sulfur batteries: mechanisms of performance enhancement.* Advanced Materials, 2015. **27**(1): p. 101-108.

139. Liu, Y., et al., *Solubility-mediated sustained release enabling nitrate additive in carbonate electrolytes for stable lithium metal anode.* Nature communications, 2018. **9**(1): p. 1-10.

140.   Zhang, X.-Q., et al., *Regulating anions in the solvation sheath of lithium ions for stable lithium metal batteries.* ACS Energy Letters, 2019. **4**(2): p. 411-416.

141.   Cui, X., et al., *Study of gadolinium based protective coating for magnesium alloys.* Surface engineering, 2012. **28**(10): p. 719-724.

142.   Xu, R., et al., *Artificial soft–rigid protective layer for dendrite-free lithium metal anode.* Advanced Functional Materials, 2018. **28**(8): p. 1705838.

143.   Stone, G., et al., *Resolution of the modulus versus adhesion dilemma in solid polymer electrolytes for rechargeable lithium metal batteries.* Journal of The Electrochemical Society, 2011. **159**(3): p. A222.

144.   Brissot, C., et al., *Dendritic growth mechanisms in lithium/polymer cells.* Journal of power sources, 1999. **81**: p. 925-929.

145.   Merrill, L.C., et al., *Polymer–Ceramic Composite Electrolytes for Lithium Batteries: A Comparison between the Single-Ion-Conducting Polymer Matrix and Its Counterpart.* ACS Applied Energy Materials, 2020. **3**(9): p. 8871-8881.

146.   Jiang, T., et al., *Solvent-free synthesis of thin, flexible, nonflammable garnet-based composite solid electrolyte for all-solid-state lithium batteries.* Advanced Energy Materials, 2020. **10**(12): p. 1903376.

147.   Bae, J., et al., *Designing 3D nanostructured garnet frameworks for enhancing ionic conductivity and flexibility in composite polymer electrolytes for lithium batteries.* Energy Storage Materials, 2018. **15**: p. 46-52.

148.   Hayashi, A., et al., *Preparation of Li2S–P2S5 amorphous solid electrolytes by mechanical milling.* Journal of the American Ceramic Society, 2001. **84**(2): p. 477-79.

149. Mizuno, F., et al., *New, highly ion-conductive crystals precipitated from Li2S–P2S5 glasses.* Advanced Materials, 2005. **17**(7): p. 918-921.

150. Sakuda, A., A. Hayashi, and M. Tatsumisago, *Sulfide solid electrolyte with favorable mechanical property for all-solid-state lithium battery.* Scientific reports, 2013. **3**(1): p. 1-5.

151. Zhu, Y., X. He, and Y. Mo, *Origin of outstanding stability in the lithium solid electrolyte materials: insights from thermodynamic analyses based on first-principles calculations.* ACS applied materials & interfaces, 2015. **7**(42): p. 23685-23693.

152. Kamaya, N., et al., *A lithium superionic conductor.* Nature materials, 2011. **10**(9): p. 682-686.

153. Deng, Z., et al., *Elastic properties of alkali superionic conductor electrolytes from first principles calculations.* Journal of The Electrochemical Society, 2015. **163**(2): p. A67.

154. Inaguma, Y., et al., *High ionic conductivity in lithium lanthanum titanate.* Solid State Communications, 1993. **86**(10): p. 689-693.

155. Cho, Y.-H., et al., *Mechanical properties of the solid Li-ion conducting electrolyte: Li0. 33La0. 57TiO3.* Journal of Materials Science, 2012. **47**(16): p. 5970-5977.

156. Murugan, R., V. Thangadurai, and W. Weppner, *Fast lithium ion conduction in garnet-type Li7La3Zr2O12.* Angewandte Chemie International Edition, 2007. **46**(41): p. 7778-7781.

157. Thangadurai, V., S. Narayanan, and D. Pinzaru, *Garnet-type solid-state fast Li ion conductors for Li batteries: critical review.* Chemical Society Reviews, 2014. **43**(13): p. 4714-4727.

158.   Yu, S., et al., *Elastic properties of the solid electrolyte Li7La3Zr2O12 (LLZO).* Chemistry of Materials, 2016. **28**(1): p. 197-206.

159.   Alpen, U.v., A. Rabenau, and G. Talat, *Ionic conductivity in Li3N single crystals.* Applied Physics Letters, 1977. **30**(12): p. 621-623.

160.   Rabenau, A., *Lithium nitride and related materials case study of the use of modern solid state research techniques.* Solid State Ionics, 1982. **6**(4): p. 277-293.

161.   Bates, J., et al., *Electrical properties of amorphous lithium electrolyte thin films.* Solid state ionics, 1992. **53**: p. 647-654.

162.   Herbert, E.G., et al., *Mechanical characterization of LiPON films using nanoindentation.* Thin Solid Films, 2011. **520**(1): p. 413-418.

163.   Croce, F., et al., *Nanocomposite polymer electrolytes for lithium batteries.* Nature, 1998. **394**(6692): p. 456-458.

164.   Edman, L., A. Ferry, and M.M. Doeff, *Slow recrystallization in the polymer electrolyte system poly (ethylene oxide) n–LiN (CF3SO2) 2.* Journal of Materials Research, 2000. **15**(9): p. 1950-1954.

165.   Nishimoto, A., et al., *High ionic conductivity of new polymer electrolytes based on high molecular weight polyether comb polymers.* Electrochimica acta, 1998. **43**(10-11): p. 1177-1184.

166.   Hu, Y.-S., *Batteries: getting solid.* Nature Energy, 2016. **1**(4): p. 1-2.

167.   Janek, J. and W.G. Zeier, *A solid future for battery development.* Nature Energy, 2016. **1**(9): p. 1-4.

168. Gao, Z., et al., *Promises, challenges, and recent progress of inorganic solid-state electrolytes for all-solid-state lithium batteries.* Advanced materials, 2018. **30**(17): p. 1705702.

169. Ma, C., et al., *Atomic-scale origin of the large grain-boundary resistance in perovskite Li-ion-conducting solid electrolytes.* Energy & Environmental Science, 2014. **7**(5): p. 1638-1642.

170. Dondelinger, M., et al., *Electrochemical stability of lithium halide electrolyte with antiperovskite crystal structure.* Electrochimica Acta, 2019. **306**: p. 498-505.

171. Hong, H.-P., *Crystal structure and ionic conductivity of Li14Zn (GeO4) 4 and other new Li+ superionic conductors.* Materials Research Bulletin, 1978. **13**(2): p. 117-124.

172. Kanno, R., et al., *Synthesis of a new lithium ionic conductor, thio-LISICON–lithium germanium sulfide system.* Solid state ionics, 2000. **130**(1-2): p. 97-104.

173. Monchak, M., et al., *Lithium diffusion pathway in Li1. 3Al0. 3Ti1. 7 (PO4) 3 (LATP) superionic conductor.* Inorganic chemistry, 2016. **55**(6): p. 2941-2945.

174. Bron, P., et al., *Li10SnP2S12: an affordable lithium superionic conductor.* Journal of the American Chemical Society, 2013. **135**(42): p. 15694-15697.

175. Deiseroth, H.J., et al., *Li6PS5X: a class of crystalline Li-rich solids with an unusually high Li+ mobility.* Angewandte Chemie, 2008. **120**(4): p. 767-770.

176. Li, Y., et al., *Mastering the interface for advanced all-solid-state lithium rechargeable batteries.* Proceedings of the National Academy of Sciences, 2016. **113**(47): p. 13313-13317.

177. Wenzel, S., et al., *Interphase formation on lithium solid electrolytes—An in situ approach to study interfacial reactions by photoelectron spectroscopy.* Solid State Ionics, 2015. **278**: p. 98-105.

178. Zhu, Y., X. He, and Y. Mo, *First principles study on electrochemical and chemical stability of solid electrolyte–electrode interfaces in all-solid-state Li-ion batteries.* Journal of Materials Chemistry A, 2016. **4**(9): p. 3253-3266.

179. Bates, J., et al., *Thin-film rechargeable lithium batteries.* Journal of Power Sources, 1995. **54**(1): p. 58-62.

180. Aono, H., et al., *Ionic conductivity of solid electrolytes based on lithium titanium phosphate.* Journal of the electrochemical society, 1990. **137**(4): p. 1023.

181. Ding, Z., et al., *Interfaces: Key issue to be solved for all solid-state lithium battery technologies.* Journal of The Electrochemical Society, 2020. **167**(7): p. 070541.

182. Liu, Q., et al., *Challenges and perspectives of garnet solid electrolytes for all solid-state lithium batteries.* Journal of Power Sources, 2018. **389**: p. 120-134.

183. Zhang, X., et al., *Synergistic coupling between Li6. 75La3Zr1. 75Ta0. 25O12 and poly (vinylidene fluoride) induces high ionic conductivity, mechanical strength, and thermal stability of solid composite electrolytes.* Journal of the American Chemical Society, 2017. **139**(39): p. 13779-13785.

184. Manthiram, A., X. Yu, and S. Wang, *Lithium battery chemistries enabled by solid-state electrolytes.* Nature Reviews Materials, 2017. **2**(4): p. 1-16.

185. Kotobuki, M., et al., *Compatibility of Li7La3Zr2O12 solid electrolyte to all-solid-state battery using Li metal anode.* Journal of the Electrochemical Society, 2010. **157**(10): p. A1076.

186.   Buschmann, H., et al., *Structure and dynamics of the fast lithium ion conductor "Li 7 La 3 Zr 2 O 12".* Physical Chemistry Chemical Physics, 2011. **13**(43): p. 19378-19392.

187.   Fu, K., et al., *Toward garnet electrolyte–based Li metal batteries: An ultrathin, highly effective, artificial solid-state electrolyte/metallic Li interface.* Science Advances, 2017. **3**(4): p. e1601659.

188.   Cheng, L., et al., *Effect of surface microstructure on electrochemical performance of garnet solid electrolytes.* ACS applied materials & interfaces, 2015. **7**(3): p. 2073-2081.

189.   Xia, W., et al., *Ionic conductivity and air stability of Al-doped Li7La3Zr2O12 sintered in alumina and Pt crucibles.* ACS applied materials & interfaces, 2016. **8**(8): p. 5335-5342.

190.   Sharafi, A., et al., *Surface chemistry mechanism of ultra-low interfacial resistance in the solid-state electrolyte Li7La3Zr2O12.* Chemistry of Materials, 2017. **29**(18): p. 7961-7968.

191.   Sharafi, A., et al., *Impact of air exposure and surface chemistry on Li–Li 7 La 3 Zr 2 O 12 interfacial resistance.* Journal of Materials Chemistry A, 2017. **5**(26): p. 13475-13487.

192.   Wakasugi, J., H. Munakata, and K. Kanamura, *Effect of gold layer on interface resistance between lithium metal anode and Li6. 25Al0. 25La3Zr2O12 solid electrolyte.* Journal of The Electrochemical Society, 2017. **164**(6): p. A1022.

193.   Luo, W., et al., *Transition from superlithiophobicity to superlithiophilicity of garnet solid-state electrolyte.* Journal of the American Chemical Society, 2016. **138**(37): p. 12258-12262.

194.   Luo, W., et al., *Reducing interfacial resistance between garnet-structured solid-state electrolyte and Li-metal anode by a germanium layer.* Advanced Materials, 2017. **29**(22): p. 1606042.

195.   Fu, K., et al., *Transient behavior of the metal interface in lithium metal–garnet batteries.* Angewandte Chemie International Edition, 2017. **56**(47): p. 14942-14947.

196.   Han, X., et al., *Negating interfacial impedance in garnet-based solid-state Li metal batteries.* Nature materials, 2017. **16**(5): p. 572-579.

197.   Wang, C., et al., *Conformal, nanoscale ZnO surface modification of garnet-based solid-state electrolyte for lithium metal anodes.* Nano letters, 2017. **17**(1): p. 565-571.

198.   Shao, Y., et al., *Drawing a soft interface: an effective interfacial modification strategy for garnet-type solid-state Li batteries.* ACS Energy Letters, 2018. **3**(6): p. 1212-1218.

199.   Xu, H., et al., *Li3N-modified garnet electrolyte for all-solid-state lithium metal batteries operated at 40 C.* Nano letters, 2018. **18**(11): p. 7414-7418.

200.   Baniya, A., et al., *Mitigating Interfacial Mismatch between Lithium Metal and Garnet-Type Solid Electrolyte by Depositing Metal Nitride Lithiophilic Interlayer.* ACS Applied Energy Materials, 2022.

201.   Xu, R., et al., *Interface engineering of sulfide electrolytes for all-solid-state lithium batteries.* Nano Energy, 2018. **53**: p. 958-966.

202.   Gurung, A., et al., *A review on strategies addressing interface incompatibilities in inorganic all-solid-state lithium batteries.* Sustainable Energy & Fuels, 2019. **3**(12): p. 3279-3309.

203.   Kato, A., A. Hayashi, and M. Tatsumisago, *Enhancing utilization of lithium metal electrodes in all-solid-state batteries by interface modification with gold thin films.* Journal of Power Sources, 2016. **309**: p. 27-32.

204. Nagao, M., A. Hayashi, and M. Tatsumisago, *Bulk-type lithium metal secondary battery with indium thin layer at interface between Li electrode and Li2S-P2S5 solid electrolyte.* Electrochemistry, 2012. **80**(10): p. 734-736.

205. Sahu, G., et al., *Air-stable, high-conduction solid electrolytes of arsenic-substituted Li 4 SnS 4.* Energy & Environmental Science, 2014. **7**(3): p. 1053-1058.

206. Zhang, Z., et al., *Interface re-engineering of Li10GeP2S12 electrolyte and lithium anode for all-solid-state lithium batteries with ultralong cycle life.* ACS applied materials & interfaces, 2018. **10**(3): p. 2556-2565.

207. Wang, C., et al., *Stabilizing interface between Li10SnP2S12 and Li metal by molecular layer deposition.* Nano Energy, 2018. **53**: p. 168-174.

208. Gao, Y., et al., *Salt-based organic–inorganic nanocomposites: towards a stable lithium Metal/Li10GeP2S12 solid electrolyte interface.* Angewandte Chemie International Edition, 2018. **57**(41): p. 13608-13612.

209. Philip, M.A., et al., *Improving cell resistance and cycle life with solvate-coated thiophosphate solid electrolytes in lithium batteries.* ACS applied materials & interfaces, 2018. **11**(2): p. 2014-2021.

210. Wang, C., et al., *Boosting the performance of lithium batteries with solid-liquid hybrid electrolytes: Interfacial properties and effects of liquid electrolytes.* Nano Energy, 2018. **48**: p. 35-43.

211. Wang, M. and J. Sakamoto, *Correlating the interface resistance and surface adhesion of the Li metal-solid electrolyte interface.* Journal of Power Sources, 2018. **377**: p. 7-11.

212. Lu, Y., et al., *An in situ element permeation constructed high endurance Li–LLZO interface at high current densities.* Journal of Materials Chemistry A, 2018. **6**(39): p. 18853-18858.

213. Zhou, W., et al., *Polymer lithium-garnet interphase for an all-solid-state rechargeable battery.* Nano Energy, 2018. **53**: p. 926-931.

214. Liu, B., et al., *Garnet solid electrolyte protected Li-metal batteries.* ACS applied materials & interfaces, 2017. **9**(22): p. 18809-18815.

215. Available from: https://letstalkscience.ca/educational-resources/stem-in-context/how-does-a-lithium-ion-battery-work ; https://web2.ph.utexas.edu/~coker2/index.files/grating.htm ; https://www.ceb.cam.ac.uk/research/groups/rg-eme/Edu/linear-sweep-and-cyclic-voltametry-the-principles; https://www.pveducation.org/pvcdrom/design-of-silicon-cells/anti-reflection-coating-color

216. Etacheri, V., et al., *Challenges in the development of advanced Li-ion batteries: a review.* Energy & Environmental Science, 2011. **4**(9): p. 3243-3262.

217. Kamali, A.R. and D.J. Fray, *Review on carbon and silicon based materials as anode materials for lithium ion batteries.* J. New Mater. Electrochem. Syst, 2010. **13**(2): p. 147-160.

218. Verma, P., P. Maire, and P. Novák, *A review of the features and analyses of the solid electrolyte interphase in Li-ion batteries.* Electrochimica Acta, 2010. **55**(22): p. 6332-6341.

219. Despić, A. and K.I. Popov, *Transport-controlled deposition and dissolution of metals*, in *Modern Aspects of Electrochemistry No. 7*. 1972, Springer. p. 199-313.

220. Wang, C., et al., *Controlling Li ion flux through materials innovation for dendrite-free lithium metal anodes.* Advanced Functional Materials, 2019. **29**(49): p. 1905940.

221. Santos, E. and W. Schmickler, *The crucial role of local excess charges in dendrite growth on lithium electrodes.* Angewandte Chemie International Edition, 2021. **60**(11): p. 5876-5881.

222. Huang, Z., et al., *Realizing stable lithium deposition by in situ grown Cu 2 S nanowires inside commercial Cu foam for lithium metal anodes.* Journal of Materials Chemistry A, 2019. **7**(2): p. 727-732.

223. Zhang, C., et al., *Vertically aligned lithiophilic CuO nanosheets on a Cu collector to stabilize lithium deposition for lithium metal batteries.* Advanced Energy Materials, 2018. **8**(21): p. 1703404.

224. Rosso, M., et al., *Dendrite short-circuit and fuse effect on Li/polymer/Li cells.* Electrochimica Acta, 2006. **51**(25): p. 5334-5340.

225. Monroe, C. and J. Newman, *The impact of elastic deformation on deposition kinetics at lithium/polymer interfaces.* Journal of The Electrochemical Society, 2005. **152**(2): p. A396.

226. Kim, H., et al., *Metallic anodes for next generation secondary batteries.* Chemical Society Reviews, 2013. **42**(23): p. 9011-9034.

227. Ding, F., et al., *Dendrite-free lithium deposition via self-healing electrostatic shield mechanism.* Journal of the American Chemical Society, 2013. **135**(11): p. 4450-4456.

228. Zhang, Y., et al., *Dendrite-free lithium deposition with self-aligned nanorod structure.* Nano letters, 2014. **14**(12): p. 6889-6896.

229. Dokko, K., et al., *Direct evidence for Li ion hopping conduction in highly concentrated sulfolane-based liquid electrolytes.* The Journal of Physical Chemistry B, 2018. **122**(47): p. 10736-10745.

230. Wagner, R., et al., *Crystal structure of garnet-related Li-ion conductor Li7–3 x Ga x La3Zr2O12: fast Li-ion conduction caused by a different cubic modification?* Chemistry of materials, 2016. **28**(6): p. 1861-1871.

231. Awaka, J., et al., *Crystal structure of fast lithium-ion-conducting cubic Li7La3Zr2O12.* Chemistry letters, 2011. **40**(1): p. 60-62.

232. Meesala, Y., et al., *Recent advancements in Li-ion conductors for all-solid-state Li-ion batteries.* ACS Energy Letters, 2017. **2**(12): p. 2734-2751.

233. Chen, F., et al., *Origin of the phase transition in lithium garnets.* The Journal of Physical Chemistry C, 2018. **122**(4): p. 1963-1972.

234. Bernstein, N., M. Johannes, and K. Hoang, *Origin of the structural phase transition in Li 7 La 3 Zr 2 O 12.* Physical review letters, 2012. **109**(20): p. 205702.

235. Thangadurai, V. and W. Weppner, *Investigations on electrical conductivity and chemical compatibility between fast lithium ion conducting garnet-like Li6BaLa2Ta2O12 and lithium battery cathodes.* Journal of Power Sources, 2005. **142**(1-2): p. 339-344.

236. Allen, J.L., et al., *Effect of substitution (Ta, Al, Ga) on the conductivity of Li7La3Zr2O12.* Journal of Power Sources, 2012. **206**: p. 315-319.

237. Huang, M., A. Dumon, and C.-W. Nan, *Effect of Si, In and Ge doping on high ionic conductivity of Li7La3Zr2O12.* Electrochemistry communications, 2012. **21**: p. 62-64.

238. Wolfenstine, J., et al., *Synthesis and high Li-ion conductivity of Ga-stabilized cubic Li7La3Zr2O12.* Materials Chemistry and Physics, 2012. **134**(2-3): p. 571-575.

239. Ramakumar, S., et al., *Structure and Li+ dynamics of Sb-doped Li 7 La 3 Zr 2 O 12 fast lithium ion conductors.* Physical Chemistry Chemical Physics, 2013. **15**(27): p. 11327-11338.

240. Rangasamy, E., et al., *The effect of 24c-site (A) cation substitution on the tetragonal– cubic phase transition in Li7− xLa3− xAxZr2O12 garnet-based ceramic electrolyte.* Journal of Power Sources, 2013. **230**: p. 261-266.

241. Thompson, T., et al., *Tetragonal vs. cubic phase stability in Al–free Ta doped Li 7 La 3 Zr 2 O 12 (LLZO).* Journal of Materials Chemistry A, 2014. **2**(33): p. 13431-13436.

242. Buannic, L., et al., *Dual substitution strategy to enhance Li+ ionic conductivity in Li7La3Zr2O12 solid electrolyte.* Chemistry of materials, 2017. **29**(4): p. 1769-1778.

243. Song, Y., et al., *Probing into the origin of an electronic conductivity surge in a garnet solid-state electrolyte.* Journal of Materials Chemistry A, 2019. **7**(40): p. 22898-22902.

244. Miara, L.J., et al., *First-principles studies on cation dopants and electrolyte/ cathode interphases for lithium garnets.* Chemistry of Materials, 2015. **27**(11): p. 4040-4047.

245. Ni, L., Z. Wu, and C. Zhang, *Effect of Sintering Process on Ionic Conductivity of Li7- xLa3Zr2-xNbxO12 (x= 0, 0.2, 0.4, 0.6) Solid Electrolytes.* Materials, 2021. **14**(7): p. 1671.

246. Haik, O., et al., *On the surface chemistry of LiMO2 cathode materials (M=[MnNi] and [MnNiCo]): electrochemical, spectroscopic, and calorimetric studies.* Journal of the electrochemical society, 2010. **157**(10): p. A1099.

247. Yada, C., et al., *Dielectric modification of 5V-class cathodes for high-voltage all-solid- state lithium batteries.* Advanced Energy Materials, 2014. **4**(9): p. 1301416.

248. Sakuda, A., A. Hayashi, and M. Tatsumisago, *Interfacial observation between LiCoO2 electrode and Li2S− P2S5 solid electrolytes of all-solid-state lithium secondary batteries using transmission electron microscopy.* Chemistry of Materials, 2010. **22**(3): p. 949-956.

249. Jung, Y.S., et al., *Issues and challenges for bulk-type all-solid-state rechargeable lithium batteries using sulfide solid electrolytes.* Israel Journal of Chemistry, 2015. **55**(5): p. 472-485.

250. Takada, K., *Interfacial nanoarchitectonics for solid-state lithium batteries.* Langmuir, 2013. **29**(24): p. 7538-7541.

251. Takada, K., N. Ohta, and Y. Tateyama, *Recent progress in interfacial nanoarchitectonics in solid-state batteries.* Journal of Inorganic and Organometallic Polymers and Materials, 2015. **25**(2): p. 205-213.

252. Ohta, N., et al., *LiNbO3-coated LiCoO2 as cathode material for all solid-state lithium secondary batteries.* Electrochemistry communications, 2007. **9**(7): p. 1486-1490.

253. Takada, K., et al., *Interfacial phenomena in solid-state lithium battery with sulfide solid electrolyte.* Solid State Ionics, 2012. **225**: p. 594-597.

254. Haruyama, J., et al., *Space–charge layer effect at interface between oxide cathode and sulfide electrolyte in all-solid-state lithium-ion battery.* Chemistry of Materials, 2014. **26**(14): p. 4248-4255.

255. Nagao, M., et al., *Li2S nanocomposites underlying high-capacity and cycling stability in all-solid-state lithium–sulfur batteries.* Journal of Power Sources, 2015. **274**: p. 471-476.

256. Takeuchi, T., et al., *All-solid-state lithium secondary battery with Li2S–C composite positive electrode prepared by spark-plasma-sintering process.* Journal of The Electrochemical Society, 2010. **157**(11): p. A1196.

257. Kishida, K., et al., *Influences of Microstructures of the Cathode/Electrolyte Interface on the Electrochemical Properties of All Solid-State Li-ion Batteries.* MRS Online Proceedings Library (OPL), 2006. **972**.

258. Vadhva, P., et al., *Electrochemical Impedance Spectroscopy for All-Solid-State Batteries: Theory, Methods and Future Outlook.* ChemElectroChem, 2021. **8**(11): p. 1930-1947.

259. Zhang, W., et al., *Interfacial processes and influence of composite cathode microstructure controlling the performance of all-solid-state lithium batteries.* ACS applied materials & interfaces, 2017. **9**(21): p. 17835-17845.

260. Choi, W., et al., *Modeling and applications of electrochemical impedance spectroscopy (EIS) for lithium-ion batteries.* Journal of Electrochemical Science and Technology, 2020. **11**(1): p. 1-13.

261. Strehlow, H., *G. Milazzo and S. Carioli: Tables of Standard Electrode Potentials. John Wiley and Sons Ltd., Chichester, New York, Brisbane, Toronto 1978. XVI+ 419 Seiten. Preis:£ 17, 50.* 1978, Wiley Online Library.

262. Liu, B., J.-G. Zhang, and W. Xu, *Advancing lithium metal batteries.* Joule, 2018. **2**(5): p. 833-845.

263. Suo, L., et al., *A new class of solvent-in-salt electrolyte for high-energy rechargeable metallic lithium batteries.* Nature communications, 2013. **4**(1): p. 1-9.

264. Yamada, Y., et al., *Unusual stability of acetonitrile-based superconcentrated electrolytes for fast-charging lithium-ion batteries.* Journal of the American Chemical Society, 2014. **136**(13): p. 5039-5046.

265.   Togasaki, N., T. Momma, and T. Osaka, *Enhanced cycling performance of a Li metal anode in a dimethylsulfoxide-based electrolyte using highly concentrated lithium salt for a lithium− oxygen battery.* Journal of Power Sources, 2016. **307**: p. 98-104.

266.   Liu, B., et al., *Enhanced cycling stability of rechargeable Li–O2 batteries using high-concentration electrolytes.* Advanced Functional Materials, 2016. **26**(4): p. 605-613.

267.   Raiser, D. and J. Deville, *Study of XPS photoemission of some gadolinium compounds.* Journal of electron spectroscopy and related phenomena, 1991. **57**(1): p. 91-97.

268.   Zhang, H., et al., *New ionic liquids based on a super-delocalized perfluorinated sulfonimide anion: physical and electrochemical properties.* Electrochimica Acta, 2016. **207**: p. 66-75.

269.   Nie, M. and B.L. Lucht, *Role of lithium salt on solid electrolyte interface (SEI) formation and structure in lithium ion batteries.* Journal of the Electrochemical Society, 2014. **161**(6): p. A1001.

270.   Madec, L.n., et al., *Effect of sulfate electrolyte additives on LiNi1/3Mn1/3Co1/3O2/graphite pouch cell lifetime: correlation between XPS surface studies and electrochemical test results.* The Journal of Physical Chemistry C, 2014. **118**(51): p. 29608-29622.

271.   Jie, Y., et al., *Enabling high-voltage lithium metal batteries by manipulating solvation structure in ester electrolyte.* Angewandte Chemie, 2020. **132**(9): p. 3533-3538.

272.   Wang, Q., et al., *Dendrite-free lithium deposition via a superfilling mechanism for high-performance Li-metal batteries.* Advanced Materials, 2019. **31**(41): p. 1903248.

273.   Xue, W., et al., *The effect of sintering process on lithium ionic conductivity of Li 6.4 Al 0.2 La 3 Zr 2 O 12 garnet produced by solid-state synthesis.* RSC Advances, 2018. **8**(24): p. 13083-13088.

274.   Liu, G., et al. *Synthesis of Li7La3Zr2O12 Solid Electrolyte by Solid Phase Sintering Method.* in *IOP Conference Series: Materials Science and Engineering.* 2019. IOP Publishing.

275.   ACOSTA-ENRIQUEZ, E., et al., *NANOSTRUCTURED FIBERS OF A-SI3N4 DEPOSITED BY HYSY-CVD.*

276.   Dhivya, L., et al., *Facile synthesis of high lithium ion conductive cubic phase lithium garnets for electrochemical energy storage devices.* RSC advances, 2015. **5**(116): p. 96042-96051.

277.   Yang, H.-C., et al., *Surface and interface engineering for organic–inorganic composite membranes.* Journal of Materials Chemistry A, 2016. **4**(25): p. 9716-9729.

278.   Cheng, X.B., et al., *Dendrite-free lithium deposition induced by uniformly distributed lithium ions for efficient lithium metal batteries.* Advanced materials, 2016. **28**(15): p. 2888-2895.

279.   Xiang, J., et al., *Improved Rechargeability of Lithium Metal Anode via Controlling Lithium-Ion Flux.* Advanced Energy Materials, 2018. **8**(36): p. 1802352.

280.   Krauskopf, T., et al., *Lithium-metal growth kinetics on LLZO garnet-type solid electrolytes.* Joule, 2019. **3**(8): p. 2030-2049.

281.   Li, X., et al., *Study of lithium silicide nanoparticles as anode materials for advanced lithium ion batteries.* ACS applied materials & interfaces, 2017. **9**(19): p. 16071-16080.

282.   Lang, J. and J. Charlot, *Li3N–Si3N4 system.* Rev. Chim. Miner, 1970. **7**(1): p. 121-131.

283. Yamane, H., S. Kikkawa, and M. Koizumi, *Preparation of lithium silicon nitrides and their lithium ion conductivity.* Solid State Ionics, 1987. **25**(2-3): p. 183-191.

284. Ulvestad, A., J.P. Mæhlen, and M. Kirkengen, *Silicon nitride as anode material for Li-ion batteries: Understanding the SiNx conversion reaction.* Journal of Power Sources, 2018. **399**: p. 414-421.

285. Li, Y., et al., *Crystal, electronic structures and photoluminescence properties of rare-earth doped LiSi2N3.* Journal of Solid State Chemistry, 2009. **182**(2): p. 301-311.

286. Houmes, J.D. and H.-C. zur Loye, *Microwave synthesis of ternary nitride materials.* Journal of Solid State Chemistry, 1997. **130**(2): p. 266-271.

287. Wen, Z., et al., *A new ternary composite lithium silicon nitride as anode material for lithium ion batteries.* Electrochemistry communications, 2006. **8**(8): p. 1349-1352.

288. Hashim, U., S.W. Chong, and W.-W. Liu, *Fabrication of silicon nitride ion sensitive field-effect transistor for pH measurement and DNA immobilization/hybridization.* Journal of Nanomaterials, 2013. **2013**.

289. Zeuner, M., S. Pagano, and W. Schnick, *Nitridosilicates and oxonitridosilicates: from ceramic materials to structural and functional diversity.* Angewandte Chemie International Edition, 2011. **50**(34): p. 7754-7775.

290. Raghavan, R., *Synthesis and electrochemical characterization of Silicon clathrates as anode materials for Lithium ion batteries*. 2013: Arizona State University.

291. Yamashita, T., et al., *Optical band gap of Li8SiN4 with disordered structure as a cathode material of lithium secondary batteries.* physica status solidi (c), 2015. **12**(6): p. 845-848.

292. Li, H., et al., *Fluoroethylene carbonate-Li-ion enabling composite solid-state electrolyte and lithium metal interface self-healing for dendrite-free lithium deposition.* Chemical Engineering Journal, 2021. **408**: p. 127254.

293. Xiong, S., et al., *Design of a Multifunctional Interlayer for NASCION-Based Solid-State Li Metal Batteries.* Advanced Functional Materials, 2020. **30**(22): p. 2001444.

294. Xia, S., et al., *High-Rate and Large-Capacity Lithium Metal Anode Enabled by Volume Conformal and Self-Healable Composite Polymer Electrolyte.* Advanced Science, 2019. **6**(9): p. 1802353.

295. Feng, Y., et al., *Low-volume-change, dendrite-free lithium metal anodes enabled by lithophilic 3D matrix with LiF-enriched surface.* Journal of Materials Chemistry A, 2019. **7**(11): p. 6090-6098.

296. Cheng, Q., et al., *Stabilizing solid electrolyte-anode interface in Li-metal batteries by boron nitride-based nanocomposite coating.* Joule, 2019. **3**(6): p. 1510-1522.

297. Shen, B., et al., *Chemically exfoliated boron nitride nanosheets form robust interfacial layers for stable solid-state Li metal batteries.* Chemical Communications, 2019. **55**(53): p. 7703-7706.

298. Lou, J., et al., *Achieving efficient and stable interface between metallic lithium and garnet-type solid electrolyte through a thin indium tin oxide interlayer.* Journal of Power Sources, 2020. **448**: p. 227440.

299. Zhang, Y., et al., *Behind the Candelabra: A Facile Flame Vapor Deposition Method for Interfacial Engineering of Garnet Electrolyte To Enable Ultralong Cycling Solid-State Li–FeF3 Conversion Batteries.* ACS Applied Materials & Interfaces, 2020. **12**(30): p. 33729-33739.

300. Zhai, P., et al., *Ionic Conductive Thermoplastic Polymer Welding Layer for Low Electrode/Solid Electrolyte Interface Resistance.* ACS Applied Energy Materials, 2020. **3**(7): p. 7011-7019.

Biography

Full Name: Abiral Baniya

Education

Institution	Location	Major/area of study	Degree	Year
Kathmandu Engineering College	Kathmandu, Nepal	Electronics and Communication Engineering	B.E.	2014
South Dakota State University	Brookings, South Dakota	Electrical Engineering	M.S.	2018
Syracuse University	Syracuse, New York	Mechanical & Aerospace Engineering	Ph.D.	2022

Publications

Baniya, Abiral, Ashim Gurung, Jyotshna Pokharel, Ke Chen, Rajesh Pathak, Buddhi Sagar Lamsal, Nabin Ghimire, Raja Sekhar Bobba, Sheikh Ifatur Rahman, Sally Mabrouk, Alevtina L. Smirnova, Kang Xu, and Quinn Qiao. 2022. "Mitigating Interfacial Mismatch between Lithium Metal and Garnet-Type Solid Electrolyte by Depositing Metal Nitride Lithiophilic Interlayer." *ACS Applied Energy Materials*. doi: 10.1021/acsaem.1c03157.

Gurung, Ashim, Jyotshna Pokharel, **Abiral Baniya**, Rajesh Pathak, Ke Chen, Buddhi Sagar Lamsal, Nabin Ghimire, Wen-Hua Zhang, Yue Zhou, and Qiquan Qiao. "A review on strategies addressing interface incompatibilities in inorganic all-solid-state lithium batteries." *Sustainable Energy & Fuels* 3, no. 12 (2019): 3279-3309.

Pathak, Rajesh, Ke Chen, Ashim Gurung, Khan Mamun Reza, Behzad Bahrami, Jyotshna Pokharel, **Abiral Baniya** et al. "Fluorinated hybrid solid-electrolyte-interphase for dendrite-free lithium deposition." *Nature communications* 11, no. 1 (2020): 1-10.

Chen, Ke, Rajesh Pathak, Ashim Gurung, Khan M. Reza, Nabin Ghimire, Jyotshna Pokharel, **Abiral Baniya** et al. "A copper-clad lithiophilic current collector for dendrite-free lithium metal anodes." *Journal of Materials Chemistry A* 8, no. 4 (2020): 1911-1919.

Pathak, Rajesh, **Abiral Baniya**, Raja Sekhar Bobba, and Quinn Qiao. "Hybrid Solid Electrolyte Interphase for Dendrite-Free and Uniform Li Deposition." In *ECS Meeting Abstracts*, no. 6, p. 370. IOP Publishing, 2021.

Pokharel, Jyotshna, Ashim Gurung, **Abiral Baniya**, Wei He, Ke Chen, Rajesh Pathak, Buddhi Sagar Lamsal, Nabin Ghimire, and Yue Zhou. "MOF-derived hierarchical carbon network as an extremely-high-performance supercapacitor electrode." *Electrochimica Acta* 394 (2021): 139058.

Gurung, A., K.M. Reza, S. Mabrouk, B. Bahrami, R. Pathak, B.S. Lamsal, S.I. Rahman, N. Ghimire, R.S. Bobba, K. Chen, **A. Baniya** et al. "Rear-Illuminated Perovskite Photorechargeable Lithium Battery". *Advanced Functional Materials*, (2020). **30**(30): p. 2001865.

Rahman, S.I., B.S. Lamsal, A. Gurung, A.H. Chowdhury, K.M. Reza, N. Ghimire, B. Bahrami, W. Luo, R.S. Bobba, J. Pokharel, and **A.Baniya**, "Grain boundary defect passivation of triple cation mixed halide perovskite with hydrazine-based aromatic iodide for efficiency improvement." *ACS Applied Materials & Interfaces*, (2020). **12**(37): p. 41312-41322.

Ghimire, N., R.S. Bobba, A. Gurung, K.M. Reza, M.A.R. Laskar, B.S. Lamsal, K. Emshadi, R. Pathak, M.A. Afroz, **A. Baniya** and A.H. Chowdhury, "Mitigating Open-Circuit Voltage Loss in Pb–Sn Low-Bandgap Perovskite Solar Cells via Additive Engineering." *ACS Applied Energy Materials*, (2021). **4**(2): p. 1731-1742.

Ghimire, Nabin, Ashim Gurung, Raja Sekhar Bobba, Khan Mamun Reza, Buddhi Sagar Lamsal, Md Ashiqur Rahman Laskar, Jyotshna Pokharel, Wei He, **Abiral Baniya**, and Yue Zhou. "Interface Engineering of Pb-Sn Low-bandgap Perovskite Solar Cells for Improved Efficiency and Stability." *Solar RRL*, (2022).